

AD-A154 587

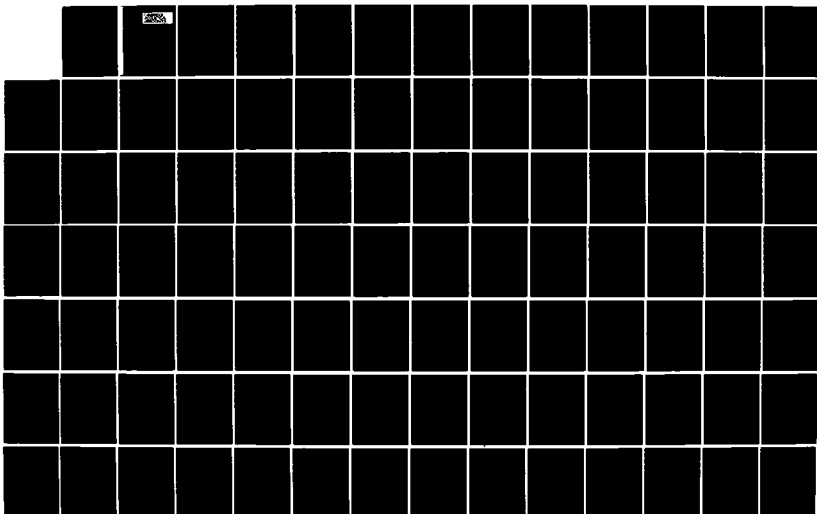
ITERATION SOLUTION FOR A SUBMERGED FORCE-DRIVEN FINITE
CYLINDER(U) CAMBRIDGE ACOUSTICAL ASSOCIATES INC MA
R MARTINEZ APR 85 U-1288-328 N00014-83-C-0194

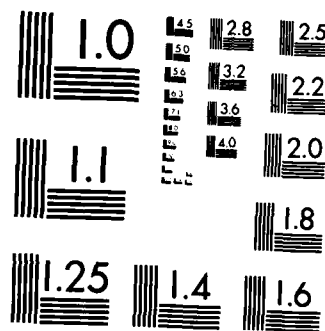
1/2

UNCLASSIFIED

F/G 20/1

NL





MICROCOPY RESOLUTION TEST CHART
NATIONAL BUREAU OF STANDARDS-1963-A

AD-A154 587

4

22

ETH

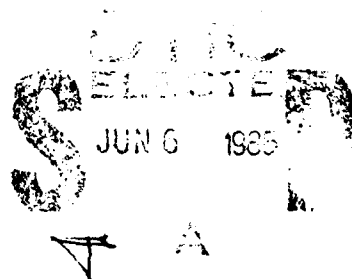
CAMBRIDGE ACOUSTICAL ASSOCIATES

ITERATION SOLUTION FOR A SUBMERGED FORCE-DRIVEN
FINITE CYLINDER

Prepared by:
Rudolph Martinez

April 1985

Report U-1208-328
Prepared for:
Scientific Officer
Group Leader Fluid Mechanics
Mechanics Division, Research Programs
Office of Naval Research
800 North Quincy Street
Arlington, Virginia 22217
Attn: Dr. Allen Kushner
Ref: N00014-83-C-0194



This document has been approved
for public release and sale, its
distribution is unlimited.

54 RINDGE AVENUE EXT., CAMBRIDGE, MASSACHUSETTS 02140

DMC FILE COPY

UNCLASSIFIED

SECURITY CLASSIFICATION OF THIS PAGE (When Data Entered)

REPORT DOCUMENTATION PAGE		READ INSTRUCTIONS BEFORE COMPLETING FORM
1. REPORT NUMBER U-1208-328	2. GOVT ACCESSION NO.	3. RECIPIENT'S CATALOG NUMBER
4. TITLE (and Subtitle) ITERATION SOLUTION FOR A SUBMERGED FORCE- DRIVEN FINITE CYLINDER		5. TYPE OF REPORT & PERIOD COVERED FINAL
7. AUTHOR(s) Rudolph Martinez		6. PERFORMING ORG. REPORT NUMBER
9. PERFORMING ORGANIZATION NAME AND ADDRESS Cambridge Acoustical Associates, Inc. 54 CambridgePark Drive Cambridge, MA 02140		8. CONTRACT OR GRANT NUMBER(s) N00014-83-C-0194
11. CONTROLLING OFFICE NAME AND ADDRESS Office of Naval Research 800 North Quincy Street Arlington, VA 22217		10. PROGRAM ELEMENT, PROJECT, TASK AREA & WORK UNIT NUMBERS
14. MONITORING AGENCY NAME & ADDRESS (if different from Controlling Office) Same as above		12. REPORT DATE April 1985
		13. NUMBER OF PAGES 104
		15. SECURITY CLASS. (of this report) Unclassified
		15a. DECLASSIFICATION/DOWNGRADING SCHEDULE
16. DISTRIBUTION STATEMENT (of this Report) Document distribution shall be only as prescribed by the Scientific Officer, Dr. H. Kushner, ONR, 800 North Quincy St., Arlington, VA 22217. <div style="border: 1px solid black; padding: 5px; display: inline-block;">This document has been approved for public release and sale; its distribution is unlimited.</div>		
17. DISTRIBUTION STATEMENT (of the abstract entered in Block 20) (if not in this report)		
18. SUPPLEMENTARY NOTES		
19. KEY WORDS (Continue on reverse side if necessary and identify by block number) Fluid Structure Interaction, Iteration, Finite-length Cylindrical Shells, Force-Driven		
20. ABSTRACT (Continue on reverse side if necessary and identify by block number) A theoretical model has been developed to predict acoustic radiation from a submerged, finite-cylindrical shell internally stiffened by ring frames and with flat, movable end caps. Iterative techniques are developed to solve the associated fluid-structure coupled systems over a moderate range of frequencies which encompasses several fluid-loaded resonances. We demonstrate that such techniques generate essentially the exact solution in a reasonably small number of iterations. Comparison of computational		

UNCLASSIFIED

SECURITY CLASSIFICATION OF THIS PAGE(When Data Entered)

Abstract (continued)

costs to those for the exact result shows iteration to be economically advantageous for all frequencies considered.

page 4.5 of 1

2

09

Accession For	
NTIS GRA&I	<input checked="" type="checkbox"/>
DTIC TAB	<input type="checkbox"/>
Unannounced	<input type="checkbox"/>
Justification	
<i>WTS 2. pto</i>	
By	
Distribution/	
Availability Codes	
Avail and/or	
Dist	
<i>A1</i>	



UNCLASSIFIED

SECURITY CLASSIFICATION OF THIS PAGE(When Data Entered)

ITERATION SOLUTION FOR A SUBMERGED
FORCE-DRIVEN FINITE CYLINDER

Prepared by:
Rudolph Martinez

April 1985

Report U-1208-328
Prepared for:
Scientific Officer
Group Leader Fluid Mechanics
Mechanics Division, Research Programs
Office of Naval Research
800 North Quincy Street
Arlington, Virginia 22217
Attn: Dr. Allen Kushner
Ref: N00014-83-C-0194

Cambridge Acoustical Associates, Inc.
54 CambridgePark Drive
Cambridge, Massachusetts 02140

TABLE OF CONTENTS

	<u>Page</u>
I. INTRODUCTION: THE MODEL IN CONTEXT	1
A. Statement of the Problem	1
B. Background	2
1. Treatment of External Fluid Space	2
2. Interaction Models for Finite Cylinders using "Exact" Two- and Three-Dimensional Fluid Formulations	2
3. Fluid-Structure Interaction using Iteration Methods	6
II. FLUID AND STRUCTURAL SYSTEMS FOR A FINITE, FRAME-STIFFENED CYLINDRICAL SHELL WITH END CAPS	
A. The Fluid System	9
1. Radiation Loading System	9
2. Calculation of Acoustic Field	17
B. The Structural System	22
1. Unframed, Capped Cylindrical Shell with Fluid Loading	23
2. Cap Motion Equation	24
3. The Frame-Stiffened Cylindrical Shell	30
4. Frame Equations	33
III. ITERATION TECHNIQUES FOR COUPLED STRUCTURAL-FLUID SYSTEMS FOR A FINITE CYLINDER	
A. Introduction	35
B. General System Equations	36
C. Iteration Algorithms for $n=0$	38
1. Method 1	38
2. Method 2	39
D. Iteration Algorithms for $n \geq 1$	43
1. Method 1	44
2. Method 2	45
E. Economic Advantage of Iterative Methods	46
IV. APPLICATION OF THEORY	
A. Introduction	48
B. System Size vs. Frequency	49
C. Choice of Number of Circumferential Modes	50
D. Effect of Stiffening Frames on Acoustic Radiation	50

	<u>Page</u>
E. Exact Solutions: Numerical Results	51
1. Summary	51
2. Frequency Sweeps; Drive on Shell, Drive on Frame ...	51
3. Directivity Patterns for Drive on Shell	52
4. Directivity Patterns for Drive on Frame	53
F. Iterated Solutions: Drive on Shell	55
1. Summary	55
2. Frequency Sweeps	56
3. Directivity Patterns	56
G. Comparison to Experiment	57
H. Computational Times for Exact vs. Iterated Solutions ...	58
V. SUMMARY AND CONCLUSIONS	60
APPENDIX II. A	61
APPENDIX II. B	63
FIGURES AND TABLES	66
REFERENCES	95

ABSTRACT

A theoretical model has been developed to predict acoustic radiation from a submerged, finite-cylindrical shell internally stiffened by ring frames and with flat, movable end caps. Iterative techniques are developed to solve the associated fluid-structure coupled systems over a moderate range of frequencies which encompasses several fluid-loaded resonances. We demonstrate that such techniques generate essentially the exact solution in a reasonably small number of iterations. Comparison of computational costs to those for the exact result shows iteration to be economically advantageous for all frequencies considered.

Acknowledgements: The author wishes to thank his colleagues,
J. M. Garrelick and J.E. Cole, for invaluable
discussions during the course of the investigation.

I. INTRODUCTION: THE MODEL IN CONTEXT

A. Statement of the Problem

The prediction of acoustic radiation from a general submerged body requires, as an intermediate step, that two coupled systems of equations be solved simultaneously for the surface response and radiation loading. One of the systems describes the in-vacuo dynamics of the structure and so appears driven by unknown fluid pressures as well as by known applied forces; the second describes the body-surface structure-less dynamics of the fluid and in exact formulations is usually provided by the Helmholtz integral, which also later yields far-field pressures once its integrand has been fully determined. While the generation of the latter fluid system may sometimes be expected to dominate computational costs, a non-negligible part of the total expense must always be earmarked to the coupled systems' solution process itself. The fluid system is again mostly to blame since its effective contribution to the total impedance is a fully populated matrix in contrast to that of the in-vacuo structure, which is typically heavily banded and therefore relatively easy to invert.

A major objective here is the development and implementation of cost-effective iterative methods to solve fluid-structure systems which arise in the analysis of a finite, frame-stiffened cylindrical shell with movable end caps. The project is in part a follow-up to that of Ref. 1, where we established that similar iterative techniques worked for the force-driven spherical shell. The spherical structure, however, is a separable geometry which besides is modally compatible with its external medium. The iterations performed were thus applied to scalar quantities and, though generally successful, left unanswered the fundamental question regarding feasibility of application to general nonseparable cases with fully populated matrices. It will be recalled that when applicable, iteration methods for the solution of a single linear system traditionally involve an order of magnitude fewer operations than do exact methods.

A second objective is to apply the model to an actual structure and to compare exact far-field predictions to existing measurements.

Summarizing the work, Chapter II contains the development of modal structural and fluid systems for a submerged finite cylinder, and Chapter III that of the several iteration algorithms intended to solve them. In Chapter IV the theory is applied to an actual situation of interest and exact and iterated solutions are discussed and compared to measurement.

B. Background

The following is a brief review of recent developments in the area of vibration of cylindrical structures, framed or unframed, submerged in a heavy fluid which at times may substantially change the character of the in-vacuo response. The use of iteration in past studies is also discussed briefly.

B.1 Treatment of the External Fluid Space

B.1.a "Exact" Models

As earlier stated, rigorous treatments of the external fluid have tended to rely on the Helmholtz integral, the alternative being a finite-element or finite-difference partitioning of a chosen fluid volume enclosing the body and the enforcement of a radiation condition on the outmost elements. The Helmholtz integral has the advantage that it yields an integral equation which requires pressure and displacements values only on the body surface -- the values which completely determine an interaction problem.

A major disadvantage however, is that by itself the Helmholtz integral cannot be solved at the eigenfrequencies of its kernel, so that fluid impedances are not always immediately available² and therefore neither are values of the fluid pressure which would accompany a specified boundary motion. This disadvantage is only apparent, however, since the fluid eigenproblem is removed upon coupling to an interior problem posed for the body cavity which complements the entire medium, and techniques such as those discussed in Refs. 3,4 may be employed for a general impedance calculation; the

methods of Refs. 5 and 6 achieve the same end by coupling the Helmholtz integral to the related equation resulting from differentiation. Moreover, in an interaction problem this apparent disadvantage is entirely fictitious since, as pointed out by Huang⁷, fluid impedances need then never be calculated as a bridging step. In effect, the fluid is then automatically coupled to an "interior" structural system and the Helmholtz eigenproblem does not come up.

Still, a number of useful and interesting studies have been exclusively devoted to the calculation of fluid impedances for the cylindrical geometry, and thus to the mapping out of the radiation loading over such structures. Chertock⁸ for example, has developed a general computational scheme for obtaining solutions of the Helmholtz integral equation corresponding to given or assumed velocity distributions. The method is iterative and he observes that, while it converges easily for low frequencies, higher frequencies demand certain modifications, e.g., averaging of two previous iterates for input in the current step. Slow or nonconvergence of iterative techniques applied just to the fluid system has been connected in Ref. 1 to the Helmholtz eigenfrequencies by recalling the convergence constraints on the standard Neumann series for a Fredholm equation⁹.

Sandman has investigated the finite but baffled cylinder¹⁰, and the finite unbaffled cylinder with zero prescribed motion at the two flat ends.¹¹ His objective was to determine modal radiation loading magnitudes corresponding to prescribed modal motions, with results which could be laid out over those for the classical infinite cylinder solution to determine the effect of the finite ends.¹² Similarly, Kozyrev and Shenderov^{13,14} have calculated fluid impedances for a finite cylinder with rigid and soft caps using a finite-difference approach; they applied Schenk's CHIEF³ method at the Helmholtz eigenfrequencies. However, Patel's¹⁵ like use of CHIEF as part of his analysis of scattering from elastic structures is unnecessary by the above argument since he ignores the fact that the in-vacuo structural formulation represents interior-problem enough for the external fluid.

The modal fluid model developed here is essentially an extension of those by Sandman to include the effect of nonzero cap motion. Thus, inversion of the fluid system derived in Chapter II would yield modal impedances immediately suitable for comparison to those of Ref. 10. Although such results were generated as part of the benchmark shake-down of the present fluid model, for the sake of conciseness we do not report them here.

B.1.b Asymptotic Models

Earlier we stated that the total cost for solving the two coupled systems for a given arbitrary frequency is sometimes dominated by the generation of the fluid system. Add to this the need to generate a new fluid system for each new frequency, and the incentive for a rational substitute for the Helmholtz equation formulation becomes clear. Geers,¹⁶ Doubly-Asymptotic Approximation (DAA) requires in effect that the fluid system be generated for only one frequency: the zero frequency which yields the apparent mass matrix for the given geometry. The method has been refined to give the exact fluid impedance not only at the low and high frequency limits, but also at an additional midrange value of choice.¹⁷ DAA has been applied in a number of studies^{18,1,19} which gauge its performance by comparing to exact, analytically available results. In a more general application, Rantlet and DiMaggio²⁰ have used DAA to model radiation loading for transient response to shock of a finite cylindrical shell for which the alternative would be the more expensive Helmholtz integral formulation.

In Ref. 1 DAA was used as part of an iterative technique to compute the exact structural response corresponding to an exact, Helmholtz-integral fluid model. DAA's purpose was to stabilize iterations whose convergence was otherwise either slow or impossible given the schemes devised. Convergence for the techniques here met with no such difficulties and a similar recourse to DAA was therefore not necessary.

B.2 Interaction Models for Finite Cylinders using "Exact" Two- and Three-Dimensional Fluid Formulations

Chen and Schweikert²¹ have applied a general finite-element methodology to a cylindrical shell and have modeled the three-dimensional fluid interface as a superposition of sources of strengths unknown a priori. An internal stiffening structure was also considered. In accordance with the earlier discussion here, they met with no matrix inversion problems. Baron, et. al.²² used a finite-difference description of a solid elastic cylinder by dividing it into bands and assuming a modal expansion in the circumferential direction. The two cap surfaces were similarly divided into concentric bands. The three-dimensional fluid was modeled using the Helmholtz integral. The final coupled system was obtained by equating the surface-normal stress and displacement fields to the external fluid pressure and particle displacement, respectively. A later model which includes the possibility of an internal void is in fact a fluid-loaded thick-shell theory for the finite cylinder.²³ Later yet, an orthotropic shell model was developed to simulate stiffening-frame effects, and elastic end caps were incorporated.²⁴

Crighton's²⁵ analysis of acoustic scattering by a finite cylindrical bar not only models the fluid as two-dimensional, but has also adopted a strip-theory, or locally-reacting, radiation approximation to eliminate the cumbersome fluid loading integral. Such simplifications allowed him to arrive at a simple and useful theoretical result for the ratio of resonant to nonresonant far-field levels.

rroughs²⁶, and Cole²⁷ have also used two-dimensional fluid models in their analyses of force-driven framed cylindrical shells. Both studies were in good agreement with experimental data. Cole models each stiffening frame as a ring of finite thickness and width, and calculates in-and out-of-plane displacements due to shell-reaction loads by means of Harari's²⁸ equations.

The familiar far-field approximation for the radical in the exponent is then applied,

$$\sqrt{1+r^2+2r\cos\alpha+(z-\bar{z})^2} \approx R \left\{ 1 + \frac{r\cos\alpha - z\bar{z}}{R^2} \right\} \quad (\text{II.A-23})$$

which may be further simplified to just R for the radical in the denominator of Eq. II.A-22, which becomes

$$\begin{aligned} \frac{e^{ikaR}}{R} f_{nm}^{(1)}(r, z) &= \frac{e^{ikaR}}{R} \cdot (-1)^{n+1} \int_{-L/2a}^{L/2a} d\bar{z} \sin \frac{m\pi a}{L} (\bar{z} + L/2a) e^{-ika(z/R)\bar{z}} \\ &\quad \cdot \int_0^\pi d\alpha \cos\alpha e^{ika(r/R)\cos\alpha} \end{aligned} \quad (\text{II.A-24})$$

The \bar{z} integral is easily evaluated. For the α integral one recognizes that

$$J_n(\xi) = \frac{i^{-n}}{\pi} \int_0^\pi d\alpha \cos\alpha e^{i\xi\cos\alpha}$$

so that finally

$$\begin{aligned} f_{nm}^{(1)}(\psi) &= - \frac{(-i)^{n+1}}{2} J_n(k\sin\psi) \cdot \\ &\quad \left\{ e^{im\pi/2} \frac{\sin\{[m\pi a/L - k\cos\psi]L/2a\}}{\{m\pi a/L - k\cos\psi\}} - e^{-im\pi/2} \frac{\sin\{[m\pi a/L + k\cos\psi]L/2a\}}{\{m\pi a/L + k\cos\psi\}} \right\} \end{aligned} \quad (\text{II.A-25})$$

Applying a similar reasoning, one finds that

$$\begin{aligned} f_{nm}^{(2)}(\psi) &= \frac{(-i)^n}{4} k\sin\psi \left\{ J_{n+1}(k\sin\psi) + J_{|n-1|}(k\sin\psi) \right\} \cdot \\ &\quad \left\{ e^{im\pi/2} \frac{\sin\{[m\pi a/L - k\cos\psi]L/2a\}}{\{m\pi a/L - k\cos\psi\}} - e^{-im\pi/2} \frac{\sin\{[m\pi a/L + k\cos\psi]L/2a\}}{\{m\pi a/L + k\cos\psi\}} \right\} \end{aligned} \quad (\text{II.A-26})$$

$$\begin{aligned}
&= \frac{e^{ikaR}}{R} \sum_{n=0}^{\infty} \cos n\psi \left\{ \begin{aligned}
&ika \rho c \sum_{m=1}^{\infty} f_{nm}^{(1)} v_{nm} \\
&+ \sum_{m=1}^{\infty} f_{nm}^{(2)} p_{nm} \\
&+ ika \rho c f_n^{(3)} v_n^C \\
&+ f_n^{(4)} p_n^C \\
&+ ika \rho c f_n^{(5)} v_n^C \\
&+ f_n^{(6)} p_n^C
\end{aligned} \right. \quad (II.A-21)
\end{aligned}$$

where we have analytically extracted out the free-field asymptotic factor e^{ikaR}/R (R nondimensional) of the three dimensional pressure field. The factor multiplying e^{ikaR}/R on the right-hand-side of Eq. II.A-21 is the directivity function for the vibrating shell with end caps as a complex radiator (the angles ϕ, ψ are defined in Fig. II.1). Thus, the quantities $f_{nm}^{(1)}, \dots, f_n^{(6)}$ are functions of $(r/R, z/R)$ ($\sin \psi, \cos \psi$) available analytically by approximating the integrals in Eq. II.A-7 resulting from substitution of Eqs. II.A-9a through II.A-9f. Each of their contribution to the total field has a simple physical interpretation. For example, $f_{nm}^{(1)}, f_{nm}^{(2)}$ represent modal monopole and dipole contributions over the shell surface since respectively they appear multiplying v_{nm} and p_{nm} . Similarly, $f_n^{(3)}$ represents the directivity contribution of a left cap monopole, and $f_n^{(4)}$ that of a right cap dipole, etc. The expressions given below clearly show all these features. To calculate $f_{nm}^{(1)}(\psi)$, one starts with its exact, near-field, form:

$$\frac{e^{ikaR}}{R} f_{nm}^{(1)}(r, z) = -\frac{1}{4\pi} \int_{-L/2a}^{L/2a} d\bar{z} \sin \frac{m\pi a}{L} (\bar{z} + L/2a) \quad (II.A-22)$$

$$\cdot 2(-1)^n \int_0^\pi \frac{d\alpha \cos n\alpha e^{ika\sqrt{1+r^2+2r\cos\alpha+(z-\bar{z})^2}}}{\sqrt{1+r^2+2r\cos\alpha+(z-\bar{z})^2}}$$

and

$$\begin{aligned}
 T_3 = & -\frac{L/a}{2\pi} \sin \frac{\tilde{m}\pi az}{L} \left\{ \frac{\cos[(m-\tilde{m})\pi(1-az/L)] - \cos(m-\tilde{m})\pi/2}{m-\tilde{m}} \right. \\
 & \left. + \frac{\cos[(m+\tilde{m})\pi(1-az/L)] - \cos(m+\tilde{m})\pi/2}{m+\tilde{m}} \right\} \\
 & + \frac{L/a}{2\pi} \cos \frac{\tilde{m}\pi az}{L} \left\{ \frac{\sin[(m-\tilde{m})\pi(1-az/L)] - \sin(m-\tilde{m})\pi/2}{m-\tilde{m}} \right. \\
 & \left. - \left(\frac{\sin[(m+\tilde{m})\pi(1-az/L)] - \sin(m+\tilde{m})\pi/2}{m+\tilde{m}} \right) \right\} \text{ for } m \neq \tilde{m}
 \end{aligned}
 \tag{II.A-18b}$$

where again, here

$$aI_{1n}(z) = \frac{2(-1)^n}{\sqrt{2+z^2}} \int_0^\pi \frac{d\alpha \cos n\alpha \exp\{ika\sqrt{2+z^2}\sqrt{1+\xi\cos\alpha}\}}{\sqrt{1+\xi\cos\alpha}}
 \tag{II.A-19a}$$

$$\begin{aligned}
 a^2 I_{2n}(z) = & \frac{2(-1)^n}{\{2+z^2\}^{3/2}} \int_0^\pi \frac{d\alpha \cos n\alpha}{\{1+\xi\cos\alpha\}^{3/2}} \cdot (1+\cos\alpha) [1-ika\sqrt{2+z^2}\sqrt{1+\xi\cos\alpha}] \\
 & \cdot \exp\{ika\sqrt{2+z^2}\sqrt{1+\xi\cos\alpha}\}
 \end{aligned}
 \tag{II.A-19b}$$

with

$$\xi = 2/(2+z^2)$$

2. Calculation of the Acoustic Field

Eq. II.A-7 is now used to calculate the acoustic far-field pressure p_{ff} defined as (with $R=\sqrt{r^2+z^2}$)

$$p_{ff} = \lim_{\substack{r \rightarrow \infty \\ z \rightarrow \infty}} \frac{1}{\sqrt{2+z^2}} \sum_{n=0}^{\infty} \cos n\phi p_n(r,z) = \lim_{R \rightarrow \infty} \sum_{n=0}^{\infty} \cos n\phi p_n(r,z)
 \tag{II.A-20}$$

$$\begin{aligned}
T_2 = & \frac{L/a}{4\pi m} \cos \frac{m\pi az}{L} \left\{ \cos(m\pi/2) \left[m\pi \left(1 - \frac{2az}{L}\right) + \sin \frac{2m\pi az}{L} \right] \right. \\
& \left. + \sin(m\pi/2) \left[\cos \frac{2m\pi az}{L} - (-1)^m \right] \right\} \\
& - \frac{L/a}{4\pi m} \sin \frac{m\pi az}{L} \left\{ \cos(m\pi/2) \left[\cos \frac{2m\pi az}{L} - (-1)^m \right] \right. \\
& \left. + \sin(m\pi/2) \left[m\pi \left(1 - \frac{2az}{L}\right) - \sin \frac{2m\pi az}{L} \right] \right\} \text{ for } m = \tilde{m}
\end{aligned}$$

(II.A-17a)

$$\begin{aligned}
\text{and } T_2 = & \frac{L/a}{2\pi} \cos \frac{\tilde{m}\pi az}{L} \left\{ \cos\left(\frac{m\pi}{2}\right) \left[\frac{\sin(m-\tilde{m})\pi/2 - \sin(m-\tilde{m})\pi za/L}{m-\tilde{m}} \right. \right. \\
& \left. \left. - \frac{\sin(m+\tilde{m})\pi/2 - \sin(m+\tilde{m})\pi za/L}{m+\tilde{m}} \right] \right. \\
& \left. + \sin\left(\frac{m\pi}{2}\right) \left[\frac{\cos(m-\tilde{m})\pi/2 - \cos(m-\tilde{m})\pi za/L}{m-\tilde{m}} \right. \right. \\
& \left. \left. - \frac{\cos(m+\tilde{m})\pi/2 - \cos(m+\tilde{m})\pi za/L}{m+\tilde{m}} \right] \right\} \\
& + \frac{L/a}{2\pi} \sin \frac{\tilde{m}\pi az}{L} \left\{ \cos(m\pi/2) \left[\frac{\cos(m-\tilde{m})\pi/2 - \cos(m-\tilde{m})\pi za/L}{m-\tilde{m}} \right. \right. \\
& \left. \left. + \frac{\cos(m+\tilde{m})\pi/2 - \cos(m+\tilde{m})\pi za/L}{m+\tilde{m}} \right] \right. \\
& \left. - \sin(m\pi/2) \left[\frac{\sin(m-\tilde{m})\pi/2 - \sin(m-\tilde{m})\pi za/L}{m-\tilde{m}} \right. \right. \\
& \left. \left. + \frac{\sin(m+\tilde{m})\pi/2 - \sin(m+\tilde{m})\pi za/L}{m+\tilde{m}} \right] \right\} \text{ for } m \neq \tilde{m}
\end{aligned}$$

(II.A-17b)

$$\begin{aligned}
T_3 = & - \frac{L/a}{4\pi m} \sin \frac{m\pi az}{L} \left\{ \cos \frac{2m\pi az}{L} - (-1)^m \right\} \\
& + \frac{L/a}{4\pi m} \cos \frac{m\pi az}{L} \left\{ \left(1 - \frac{2az}{L}\right) m\pi + \sin \frac{2m\pi az}{L} \right\} \text{ for } m = \tilde{m}
\end{aligned}$$

(II.A-18a)

the degree of computation is further reduced. Finally, all entries for which $m+\tilde{m}$ is not an even integer may be shown to be identically zero. It turns out therefore, that instead of M^2 triple integrals for the $M \times M$ submatrix, we actually have only $M/2 \cdot (M/2+1)$ double integrals for M even, or $(M+1)^2/4$ double integrals for M odd. Thus, for example, if $M=30$ the number of double integrals needed for the $M \times M$ submatrix becomes $15(15+1)=240$ (not 900). If $M=31$, then $(31+1)^2/4 = 256$ double integrals are required. For large M therefore, roughly $M^2/4$ double integrals are needed to generate most of the fluid elements by the present modal method. Since finite differences would require M^2 (or perhaps $M^2/2$ due to reciprocity), the present method represents a net savings for this part of the calculation. However, the matrix entries for the bottom two rows and rightmost two columns of [C] and [D], require the evaluation of roughly $3M$ triple integrals for $n=0$ or $2M$ for $n \geq 1$ by the modal method and the same number of double integrals by finite differences, so that, calling N the number of mesh points in the outmost of our triple integrals, it follows that both techniques are roughly equivalent in cost when $3MN = 3/4M^2$.

The double-integral versions of $C_{nm\tilde{m}}^{(1)}$, $D_{nm\tilde{m}}^{(1)}$ turn out to be:

$$C_{nm\tilde{m}}^{(1)} = \frac{1}{2\pi} [1 - (-1)^{m+\tilde{m}}] \int_0^{L/2a} dz \{ (T_1 + T_3) [a^2 I_{2n}(z)] + T_2 [a^2 I_{2n}(z+L/2a)] \} \quad (\text{II.A-15a})$$

$$D_{nm\tilde{m}}^{(1)} = -\frac{ika}{2\pi} [1 - (-1)^{m+\tilde{m}}] \int_0^{L/2a} dz \{ (T_1 + T_3) [a I_{1n}(z)] + T_2 [a I_{1n}(z+L/2a)] \} \quad (\text{II.A-15b})$$

where the quantities T_1 , T_2 , T_3 are functions of m, \tilde{m} and z :

$$T_1 = \frac{L/a}{4\pi m} [1 - (-1)^m] \sin \frac{m\pi az}{L} + \frac{L/a}{4} \cos \frac{m\pi az}{L} \text{ for } m = \tilde{m} \quad (\text{II.A-16a})$$

and

$$T_1 = \frac{L/a}{2\pi} \sin \frac{\tilde{m}\pi az}{L} \left\{ \frac{(-1)^{(m-\tilde{m})} - \cos(m-\tilde{m})\pi/2}{m-\tilde{m}} + \frac{(-1)^{(m+\tilde{m})} - \cos(m+\tilde{m})\pi/2}{m+\tilde{m}} \right\} \\ - \frac{L/a}{2\pi} \cos \frac{\tilde{m}\pi az}{L} \left\{ \frac{\sin(m-\tilde{m})\pi/2}{m-\tilde{m}} - \frac{\sin(m+\tilde{m})\pi/2}{m+\tilde{m}} \right\} \text{ for } m \neq \tilde{m}; \quad (\text{II.A-16b})$$

For $n \geq 1$ the present model has $v_n^{C_L} = v_n^{C_R} = 0$; so that the right side of Eq. II.A-13 becomes then

$$\begin{bmatrix}
 D_{n11}^{(1)} & D_{n12}^{(1)} & \dots & D_{n1M}^{(1)} \\
 D_{n21}^{(1)} & \dots & & D_{n2M}^{(1)} \\
 \vdots & & & \vdots \\
 D_{nM1}^{(1)} & \dots & & D_{nMM}^{(1)} \\
 \hline
 D_{nm=1}^{(2)} & D_{nm=2}^{(2)} & \dots & D_{nm=M}^{(2)} \\
 \hline
 D_{nm=1}^{(2)} & -D_{nm=2}^{(2)} & \dots & (-1)^{M+1} D_{nm=M}^{(2)}
 \end{bmatrix}
 \begin{Bmatrix}
 v_{nm=1} \\
 v_{nm=2} \\
 \vdots \\
 v_{nm=M}
 \end{Bmatrix}
 \quad (II.A-14)$$

where the last two columns have been deleted from the $[D]$ matrix multiplying $\{v\}$, which has been shortened accordingly. If $\{v\}^{\text{short}}$ above were known so that the above product could be performed, thus yielding a $M+2$ -element vector, the system governing the $\{p\}$ vector would still have rank $M+2$; its solution would give the shell modal fluid loading $p_{nm=1}; \dots, p_{nm=M}$ plus the fluid cap pressures $p_n^{C_L}, p_n^{C_R}$. From the acoustic viewpoint, these cap pressures, whether or not there is cap motion, represent the modal strength of radiating cap dipoles.

All constants in both $[C]$ and $[D]$ matrices require the evaluation of a triple integral. Thus, the present modal formulation initially does not appear economically advantageous compared to a similar finite-element or finite difference calculation, e.g., that in Ref. 22 where only double integrals are required. However, we now show that the bulk of the matrix elements, namely those composing the upper left $M \times M$ submatrix in both $[C]$ and $[D]$ matrices which represent the coupling of m, \tilde{m} modes on the cylindrical part of the surface, may be recast in terms of double integrals. Moreover, these submatrices are symmetric, e.g. in Eq. II.A-11 $C_{nm\tilde{m}}^{(1)} = C_{\tilde{m}nm}^{(1)}$, so that

Finally, if the modal sum $\sum_{m=1}^{\infty}$ is everywhere truncated to $\sum_{m=1}^M$, M being an integer of sufficient size, and advantage is taken of certain symmetry relations between some of the constants (e.g., it turns out that $D_{nm}^{(3)} = (-1)^{m+1} D_{nm}^{(2)}$; $C_{nm}^{(3)} = (-1)^{m+1} C_{nm}^{(2)}$), the resulting set of fluid equations may then be cast in the following matrix form:

$$\begin{bmatrix}
 L/2a + C_{n11}^{(1)} & C_{n12}^{(1)} \dots & C_{n1M}^{(1)} & C_{nm=1}^{(2)} & C_{nm=1}^{(2)} & P_{nm=1} \\
 C_{n21}^{(1)} & L/2a + C_{n22}^{(1)} \dots & C_{n2M}^{(1)} & C_{nm=2}^{(2)} & -C_{nm=2}^{(2)} & P_{nm=2} \\
 \vdots & \vdots & \vdots & \vdots & \vdots & \vdots \\
 C_{nM1}^{(1)} & \dots & L/2a + C_{nMM}^{(1)} & C_{nm=M}^{(2)} & (-1)^{M+1} C_{nm=M}^{(2)} & P_{nm=M} \\
 \hline
 \tilde{C}_{nm=1}^{(2)} & \tilde{C}_{nm=2}^{(2)} \dots & \tilde{C}_{nm=M}^{(2)} & 1/2 & \tilde{C}_n^{(3)} & C_L \\
 \hline
 \tilde{C}_{nm=1}^{(2)} & -\tilde{C}_{nm=2}^{(2)} \dots & (-1)^{M+1} \tilde{C}_{nm=M}^{(2)} & -\tilde{C}_n^{(3)} & 1/2 & C_R
 \end{bmatrix}
 =
 \begin{bmatrix}
 P_{nm=1} \\
 P_{nm=2} \\
 \vdots \\
 P_{nm=M} \\
 \hline
 C_L \\
 P_n \\
 \hline
 C_R \\
 P_n
 \end{bmatrix}$$

$$\rho c
 \begin{bmatrix}
 D_{n11}^{(1)} & D_{n12}^{(1)} \dots & D_{n1M}^{(1)} & D_{nm=1}^{(2)} & D_{nm=1}^{(2)} & V_{nm=1} \\
 D_{n21}^{(1)} & D_{n22}^{(1)} \dots & D_{n2M}^{(1)} & D_{nm=2}^{(2)} & -D_{nm=2}^{(2)} & V_{nm=2} \\
 \vdots & \vdots & \vdots & \vdots & \vdots & \vdots \\
 D_{nM1}^{(1)} & \dots & D_{nMM}^{(1)} & D_{nm=M}^{(2)} & (-1)^{M+1} D_{nm=M}^{(2)} & V_{nm=M} \\
 \hline
 D_{nm=1}^{(2)} & D_{nm=2}^{(2)} \dots & D_{nm=M}^{(2)} & \tilde{D}_n^{(3)} & \tilde{D}_n^{(4)} & C_L \\
 \hline
 D_{nm=1}^{(2)} & -D_{nm=2}^{(2)} \dots & (-1)^{M+1} D_{nm=M}^{(2)} & \tilde{D}_n^{(4)} & \tilde{D}_n^{(3)} & C_R
 \end{bmatrix}
 \begin{bmatrix}
 V_{nm=1} \\
 V_{nm=2} \\
 \vdots \\
 V_{nm=M} \\
 \hline
 C_L \\
 V_{n=0} \\
 \hline
 C_R \\
 V_{n=0}
 \end{bmatrix}$$

(II.A-13)

$$D_{nm\tilde{m}}^{(1)} = -\frac{ika}{2\pi} \int_{-L/2a}^{L/2a} dz \sin \frac{m\pi a}{L} (z+L/2a) \int_{-L/2a}^{L/2a} d\tilde{z} \sin \frac{\tilde{m}\pi a}{L} (\tilde{z}+L/2a) [aI_{1n}(\xi_1; r=1)]$$

$$C_{nm\tilde{m}}^{(1)} = \frac{1}{2\pi} \int_{-L/2a}^{L/2a} dz \sin \frac{m\pi a}{L} (z+L/2a) \int_{-L/2a}^{L/2a} d\tilde{z} \sin \frac{\tilde{m}\pi a}{L} (\tilde{z}+L/2a) [a^2 I_{2n}(\xi_1; r=1)]$$

$$D_{nm}^{(2)} = -\frac{ika}{2\pi} \int_{-L/2a}^{L/2a} dz \sin \frac{m\pi a}{L} (z+L/2a) \int_0^1 d\tilde{r} \tilde{r} [aI_{3n}(\xi_2; r=1)]$$

$$C_{nm}^{(2)} = \frac{1}{2\pi} \int_{-L/2a}^{L/2a} dz \sin \frac{m\pi a}{L} (z+L/2a) \cdot (z+L/2a) \int_0^1 d\tilde{r} \tilde{r} [a^3 I_{4n}(\xi_2; r=1)]$$

$$D_{nm}^{(3)} = -\frac{ika}{2\pi} \int_{-L/2a}^{L/2a} dz \sin \frac{m\pi a}{L} (z+L/2a) \int_0^1 d\tilde{r} \tilde{r} [aI_{5n}(\xi_3; r=1)]$$

$$C_{nm}^{(3)} = -\frac{1}{2\pi} \int_{-L/2a}^{L/2a} dz \sin \frac{m\pi a}{L} (z+L/2a) \cdot (z-L/2a) \int_0^1 d\tilde{r} \tilde{r} [a^3 I_{6n}(\xi_3; r=1)] \quad (\text{II.A-12})$$

The constants $C_{nm\tilde{m}}^{(1)}$ and $D_{nm\tilde{m}}^{(1)}$ have been initially defined in terms of Cauchy-Principal Value integrals which omit the point $\tilde{z}=z$ for which $\xi_1=1$ and for which aI_{1n} and $a^2 I_{2n}$ are therefore infinite. (Actually, it may be shown that the resulting singularity is of the log type, and thus integrable so that the Cauchy-Principal Value designation may be lifted. Such a result is consistent with the discussion in Ref. 34.)

This procedure may be repeated for field points on the left and right caps. For the point on the left cap, for example, the left-hand side of Eq. II.A-7 becomes $p_n^{C_L}$ and the second integral on the right-hand side must now be written as

$$\int_0^1$$

i.e., we return to Eq. II.A-7 and let $z=-L/2a$; multiply then by $\tilde{r}d\tilde{r}$ and integrate both sides of Eq. II.A-7 from 0 to 1. Constants similar to those in Eqs. II.A-11 and II.A-12 may be defined; these are given in Appendix II.A.(1). A similar calculation is performed for the right cap.

$$p_n(\bar{r}, -L/2a) = p_n(-L/2a) = p_n^{C_L}, \text{ a constant function of end-cap radial coordinate } \bar{r} \quad (\text{II.A-9c})$$

$$p_n(\bar{r}, L/2a) = p_n(L/2a) = p_n^{C_R}, \text{ a constant function of end-cap radial coordinate } \bar{r} \quad (\text{II.A-9d})$$

$$V_n(\bar{r}, -L/2a) = \begin{cases} V_n^{C_L}, & \text{a constant function of end cap radial coordinate for } n=0 \\ 0 & \text{for } n \geq 1 \end{cases} \quad (\text{II.A-9e})$$

$$V_n(\bar{r}, L/2a) = \begin{cases} V_n^{C_R}, & \text{a constant function of end cap radial coordinate for } n=0 \\ 0 & \text{for } n \geq 1 \end{cases} \quad (\text{II.A-9f})$$

Similar expansions may be used for the field pressure $p_n(r, z)$ on the left-hand side of Eq. II.A-7 as the point approaches the cylinder surface; e.g., for a field point (r, z) now on the cylindrical shell surface $(1, z)$ we have

$$\begin{aligned} \sum_{\tilde{m}=1}^{\infty} p_{n\tilde{m}} \sin \frac{\tilde{m}\pi a}{L} (z+L/2a) &= \sum_{\tilde{m}=1}^{\infty} \left\{ ika\rho c V_{n\tilde{m}} \left(-\frac{1}{2\pi} \int_{-L/2a}^{L/2a} d\bar{z} \sin \frac{\tilde{m}\pi a}{L} (\bar{z}+L/2a) \right. \right. \\ &\quad \left. \left. [aI_{1n}(\xi_1; r=1)] \right) + p_{n\tilde{m}} \left(-\frac{1}{2\pi} \int_{-L/2a}^{L/2a} d\bar{z} \sin \frac{\tilde{m}\pi a}{L} (\bar{z}+L/2a) [a^2 I_{2n}(\xi_1; r=1)] \right) \right\} \\ &+ \dots \end{aligned} \quad (\text{II.A-10})$$

where now $\xi_1 = 2/[2+(z-\bar{z})^2]$, and ξ_2, ξ_3 are similarly evaluated for $r=1$.

Multiplying the above by $\sin m\pi a/L(z+L/2a)$ and integrating from $-L/2a$ to $+L/2a$ with respect to z yields

$$\begin{aligned} L/2a p_{nm} &= \rho c \sum_{\tilde{m}=1}^{\infty} D_{nm\tilde{m}}^{(1)} V_{n\tilde{m}} - \sum_{\tilde{m}=1}^{\infty} C_{nm\tilde{m}}^{(1)} p_{n\tilde{m}} + \rho c D_{nm}^{(2)} V_n^{C_L} \\ &- C_{nm}^{(2)} p_n^{C_L} + \rho c D_{nm}^{(3)} V_n^{C_R} - C_{nm}^{(3)} p_n^{C_R} \end{aligned} \quad (\text{II.A-11})$$

where

$$\begin{aligned}
p_n(r, z) = & -\frac{\epsilon}{4\pi} \int_{-L/2a}^{L/2a} dz \{ ika\rho c V_n(1, \bar{z}) [aI_{1n}(r, 1, z, \bar{z})] \\
& + p_n(1, \bar{z}) [a^2 I_{2n}(r, 1, z, \bar{z})] \} \\
& - \frac{\epsilon}{4\pi} \int_0^1 d\bar{r} \bar{r} \{ ika\rho c V_n(\bar{r}, -L/2a) [aI_{3n}(r, \bar{r}, z, -L/2a)] \\
& + (z+L/2a) p_n(\bar{r}, -L/2a) [a^3 I_{4n}(r, \bar{r}, z, -L/2a)] \\
& - \frac{\epsilon}{4\pi} \int_0^1 d\bar{r} \bar{r} \{ ika\rho c V_n(r, L/2a) [aI_{5n}(r, \bar{r}, z, L/2a)] \\
& - (z-L/2a) p_n(\bar{r}, L/2a) [a^3 I_{6n}(r, \bar{r}, z, L/2a)] \}
\end{aligned} \tag{II.A-7}$$

where, for example,

$$aI_{1n}(r, 1, z, \bar{z}) = \frac{2(-1)^n}{\sqrt{1+r^2+(z-\bar{z})^2}} \int_0^\pi \frac{d\alpha \cos n\alpha e^{ika\sqrt{1+r^2+(z-\bar{z})^2} \sqrt{1+\xi_1} \cos \alpha}}{\sqrt{1+\xi_1} \cos \alpha} \tag{II.A-8}$$

with

$$\xi_1 = \frac{2r}{1+r^2+(z-\bar{z})^2}$$

The rest of the expressions for $a^2 I_{2n}$, ..., $a^3 I_{6n}$ are given in Appendix II.A. In Eqs. II.A-7 and II.A-8, all spatial variables have been normalized by the cylinder radius a . $V_n(1, \bar{z})$ and $p_n(1, \bar{z})$ stand for the normal velocity and pressure on the cylindrical part of the boundary; $V_n(\bar{r}, -L/2a)$ and $p_n(\bar{r}, -L/2a)$ stand for corresponding quantities at the left cap; and $V_n(\bar{r}, L/2a)$ and $p_n(\bar{r}, L/2a)$ stand for those at the right cap. We now assume the following expansions:

$$V_n(1, \bar{z}) = \sum_{m=1}^{\infty} V_{nm} \sin \frac{m\pi a}{L} (\bar{z}+L/2a) \tag{II.A-9a}$$

$$p_n(1, \bar{z}) = \sum_{m=1}^{\infty} p_{nm} \sin \frac{m\pi a}{L} (\bar{z}+L/2a) \tag{II.A-9b}$$

A. The Fluid System

1. Radiation Loading System

In a fluid the Helmholtz integral relates the velocity potential ϕ at a field point to boundary values of potential and velocity, both initially unknown in an interaction problem:

$$\phi = \epsilon \iint_S d\bar{S} \left\{ G \frac{\partial \phi}{\partial \bar{n}} - \frac{\partial G}{\partial \bar{n}} \phi \right\} \quad (\text{II.A-1})$$

where $\epsilon = 1, 2$ for points in the fluid and on the boundary, respectively. G is the free-field Green's function,

$$G = - \frac{e^{ikR}}{4\pi R} \quad (\text{II.A-2})$$

where k is the acoustic wavenumber ω/c , and R , the distance between field point (r, ϕ, z) and boundary point $(\bar{r}, \alpha, \bar{z})$, is given by

$$R = \sqrt{r^2 + \bar{r}^2 - 2r\bar{r}\cos(\alpha - \phi) + (z - \bar{z})^2} \quad (\text{II.A-3})$$

so that

$$\frac{\partial G}{\partial \bar{n}} = \begin{cases} \pm \frac{\partial G}{\partial \bar{z}} & \text{for points on the right cap (+) and left (-).} \\ \frac{\partial G}{\partial \bar{r}} & \text{for points on the curved, longitudinal part of the cylindrical surface.} \end{cases} \quad (\text{II.A-4})$$

The r, ϕ, z coordinate system is shown in Fig. II.1; $(\bar{r}, \alpha, \bar{z})$ correspond to running values of these variables in the integration.

The fluid pressure anywhere may be found from ϕ from the unsteady linearized Bernoulli equation

$$p = -\rho \frac{\partial \phi}{\partial t} = i\omega\rho\phi \quad (\text{II.A-5})$$

If one writes p in terms of circumferential n -modes as

$$p(r, \phi, z) = \sum_{n=0}^{\infty} p_n^{(1)}(r, z) \cos n\phi + \sum_{n=1}^{\infty} p_n^{(2)}(r, z) \sin n\phi \quad (\text{II.A-6})$$

it may be shown that both $p_n^{(1)}$ and $p_n^{(2)}$ satisfy the following form of the Helmholtz integral:

II. FLUID AND STRUCTURAL MODELS FOR A FINITE, FRAME-STIFFENED CYLINDRICAL SHELL WITH END CAPS

As earlier pointed out, the finite cylindrical geometry is nonseparable. Because of this, the modal form chosen to describe pressure and displacement variations along the axial, or curved, part of the surface will inevitably be nonorthogonal to that chosen to describe these same variables over the cap surfaces. The result is an elaborate set of linear equations which for both structure and fluid couples one set of modes to the other.

Here we assume that the simply-supported set of $\sin m\pi z/L$ functions adequately describes fluid and structural quantities over the longitudinal part of the geometry--an assumption of course not met by displacements near the ends of a freely suspended, or neutrally bouyant, cylinder but which nevertheless has proven successful in predicting acoustic radiation from such structures.²⁷

Also, because the analysis is here ultimately applied to a case for which the cylinder radius is much smaller than the shortest acoustic wavelength considered, only the radially uniform mode is used for the caps; i.e., cap displacements and pressures are given by the product of the "unit" mode and the constants which denote their values. Should future need dictate a more complete cap description, an expansion such as that of Ref. 20, Eq. 62 may be used.

In Section II.A.1 the Helmholtz integral is used to develop a radiation loading model for the finite-cylindrical geometry. In Section II.A.2 the fluid system so generated is approximated analytically for an arbitrary far-field point. The radiated pressure thus appears as a function of surface pressure and displacement, both unknown at this stage in the analysis.

Section II.B contains the analysis for the dynamics of a submerged frame-stiffened shell with end caps. The otherwise arbitrary external drive is assumed axisymmetric in the circumferential direction. Together with the fluid model of Section II.A, the structural system developed here defines the fluid-structure interaction problem.

Computational Fluid Dynamics almost by definition deals with very large linear systems, and workers in that field have often resorted to iterative techniques as the only practical means of solution. An example of a predictor-corrector type of CFD application of iteration arises in the time-domain description of the fluid medium bounded by a complex structure in impulsive motion, a calculation which normally requires the development of the solution over a large-volume grid of mesh points at each time step, and the associated enforcement of continuity of particle velocity at each instant over the contact surface. Chang and Wang³¹ have used an iterative scheme in their transient boundary condition calculation. At the end of each time step the estimated fluid pressure was used to calculate structural displacements, which then generally did not agree with those for the fluid particles at the interface. These were then corrected and the fluid medium recalculated to yield the new radiation load vector, etc.

Belytschko³² has discussed the role of iteration in the implicit time integration of system equations for the general transient fluid-structure interaction problem. Whitlow and Harris³³ have done essentially the same for unsteady transonic flow in their discussion of similar numerical techniques commonly used in that field. Transonic flow over an oscillating airfoil is governed by a nonlinear potential equation which gives rise to shocks in the gas medium; since the positions of these vary with time, a fine local mesh is usually required.

As will be discussed in Chapter III, in developing some of the iteration techniques here we have emphasized the convergence role of system subpartitioning rather than the application of methods known to accelerate convergence.

The present structural model is essentially this same model with rational simplifications to reduce the number of degrees of freedom matched between shell and frames (here only radial and circumferential displacements are used whereas Cole also matches axial displacements and out-of-plane rotations). Fundamental differences between the model here and that in Ref. 27 are therefore really confined to just the fluid-loading system, for which the present study may be viewed as providing the three-dimensional extension.

B.3 Fluid-Structure Interaction Studies using Iteration Models

Chertock⁸ has used an iterative technique to effectively invert the fluid system for a general body of revolution, in essence, to find its impedance matrix. As discussed earlier, he generally found that while the method converges easily at low frequencies, it later becomes unstable with increasing frequency. He circumvented this difficulty by altering his basic scheme to use an average value of previous iterates where before, for the lower frequencies, he had used only the most recently available value. Ref. 29, Chapter 11's general discussion on such summability techniques provides the rationale behind their potential stabilizing effect. We too applied this basic idea in our iterative treatment of the fluid-loaded driven sphere.¹

For the low-frequency limit, where the externally unbounded fluid medium has a purely inertial effect on the vibrating surface, Au-Yang³⁰ has used an iteration algorithm to find the fluid-loaded resonances of a cylindrical shell. He starts it out by assuming each resonance's value and then uses the fluid system to calculate the fluid loading at that frequency. Next, this pressure solution is introduced into the otherwise homogeneous structural system, which yields a new root, and so on. He found the technique to converge nicely for most of the frequencies calculated.

As previously discussed, $f_{nm}^{(2)}(\psi)$ stands for the contribution of dipoles on the cylindrical part of the boundary; for every n - m combination we note the factor $\sin\psi$ in the above expression. The rest of the modal directivity contributions $f_n^{(3)}, \dots, f_n^{(6)}$ turn out to be

$$f_n^{(3)}(\psi) = -\frac{(-i)^n}{2} e^{ika(L/2a)\cos\psi} \int_0^1 d\bar{r} \bar{r} J_n(k\sin\psi\bar{r}) \quad (\text{II.A-27})$$

$$f_n^{(4)}(\psi) = -\frac{(-i)^{n+1}}{2} k\cos\psi e^{ika(L/2a)\cos\psi} \int_0^1 d\bar{r} \bar{r} J_n(k\sin\psi\bar{r}) \quad (\text{II.A-28})$$

$$f_n^{(5)}(\psi) = -\frac{(-i)^n}{2} e^{-ika(L/2a)\cos\psi} \int_0^1 d\bar{r} \bar{r} J_n(k\sin\psi\bar{r}) \quad (\text{II.A-29})$$

$$f_n^{(6)}(\psi) = \frac{(-i)^{n+1}}{2} k\cos\psi e^{-ika(L/2a)\cos\psi} \int_0^1 d\bar{r} \bar{r} J_n(k\sin\psi\bar{r}) \quad (\text{II.A-30})$$

Again, $f_n^{(3)}, f_n^{(5)}$ account for monopoles at the left and right caps (acting only for $n=0$ in the present model); and $f_n^{(4)}$ and $f_n^{(6)}$ represent dipoles also at the caps (hence the extra $\cos\psi$ factor for $f_n^{(4)}, f_n^{(6)}$).

The grouping $m\pi a/L \pm ka\cos\psi$ appearing as argument of $\sin\{\}/\{\}$ in Eqs. II.A-25, 26 to a large extent determines the far-field effect of sources distributed along the shell part of the cylinder. Physically, supersonic axial modes may be expected to radiate efficiently and in the ray direction ψ^* given by $\cos\psi^* = 1/M_m$, where M_m denotes axial Mach number for the m mode. Since the modal solution is of the form $\sin m\pi z/L \exp(-i\omega t) - \exp[-i\omega(t - za/c_m)]$, with $c_m = \omega L/m\pi$, it follows that modal Mach numbers M_m are given by $\omega L/m\pi \cdot 1/c = ka/(m\pi a/L)$ so that

$$\frac{m\pi a}{L} \pm k\cos\psi = ka \left\{ \frac{1}{M_m} \pm \cos\psi \right\} \quad (\text{II.A-31})$$

Since the $\sin \{\}/\{\}$ group has its maximum value of unity at the null ψ^* of Eq. II.A-31, the analytical solution embodies the physical requirement of preferred radiation in the theoretical ray direction. Subsonic axial modes (for which Eq. II.A-31 never vanishes) lack a clear preferred radiation direction and in fact would have an identically zero far-field were the cylinder infinite in length. Their acoustic effect for the finite geometry is that of a pair of sources, one for each end of the cylinder, and thus a contribution which may be expected to be generally low in comparison to that of supersonic sources distributed over the entire surface, all reaching the far-field since their Mach lines (acoustic wavefronts) never intersect.

Similar statements may be made about radiation in the circumferential direction and the mathematical behavior of $J_n(k a \sin \psi)$ as a function of order and argument. It may be easily shown that the rotary speed of circumferential modes satisfying $n > ka$ is respectively supersonic and subsonic. Subsonic contributions instead of being attributed to finite-end effects are due now to the sources' felt acceleration as they travel in a circle. Such is the prediction of the general Ffowcs-Williams Hawkins equation³⁶ which, incidentally, also provides the theoretical foundation for Gutin noise -- the sound radiated by steady blade forces in a subsonic propeller. Acoustic radiation from the subsonic $n > ka$ circumferential modes is here really due to the same mechanism of acceleration due to rotary motion.

An important feature of the preceding far-field calculation is that it accounts for possible source noncompactness in both circumferential and axial directions. This is necessary because in Chapter IV the model will be applied to a very high-aspect ratio cylinder for which the condition $kL \gg 1$ is satisfied over much of the frequency range investigated. In fact, although the far-field condition $kR \gg 1$ is always strictly satisfied, the ratio R/L of field point distance to cylinder length turns out to be only about 4 (here for convenience R is dimensional).

However, we argue that by keeping just the $z\bar{z}$ term (and no higher-order contributions) in Eq. II.A-23 the theory adequately accounts for phase differences along the cylinder axis, or equivalently in the time domain, for the \bar{z} -dependence of retarded times $\tau = t - R/c = \tau(\bar{z})$ for sources distributed

along the cylindrical axis. Given that the approximation's neglected term inside the parenthesis of Eq. II.A-23 is known to be $1/2(\bar{z}/R)^2$, one may readily estimate its possible impact on the phase information for parameters of interest here. First, we note that axial noncompactness will have greatest effect for field points along the cylinder axis $\psi=0$ or 180° . For these, $\bar{z}^2/R^2 = \cos^2\psi \cdot \bar{z}^2/R^2 = \bar{z}^2/R^2$, so that the percent error of the neglected term is $1/2(\bar{z}/R)$. Thus, for the Chapter IV values of $\bar{z}_{\max} = L/2 = 9.58$ ft and $aR = 45$ ft, the upper bound of the phase error is about 12%, which should not seriously affect the character of signal cancellation or reinforcement at these two far-field points.

As explained immediately after Eq. II.A-23, the radical which appears in all denominators has been even more simply approximated to yield the three-dimensional spreading factor $1/R$. For the cylinder of interest here the greatest "true" source-field distance is $\sqrt{45^2 + (9.58)^2} = 46$, which implies that in using $R \approx 45$ ft as measured from the cylinder's centroid an error of less than 2.3% (or .2 dB) is incurred in so estimating the level for that "worst" source.

B. The Structural System

In Section A we have derived the fluid system modal equations. Here we develop similar equations for the structural system, i.e., for a framed, simply-supported, finite cylindrical shell with end caps. The shell is submerged and thus loaded by the fluid pressure vector of Section A, which we recall provides for radiation loading at the cap ends. Consistent with the analysis in Section A we assume that cap motion takes place only for $n=0$, so that as earlier stated, computed cap pressures for $n \geq 1$ are due only to diffraction from the cylindrical part of the shell surface and may be expected therefore to yield a far-field on-axis level of modal radiated pressure significantly below that for $n=0$. The system is driven by a force distribution applied either at one of the frames or directly anywhere on the shell skin. The structure may also be driven axially by a load acting at the end cap. Shell frames, caps, and the applied drives are all assumed circumferentially axisymmetric and thus describable by the $\cos n\phi$ series.

Sections B.1,2 develop the model for an unframed shell with end caps. Section B.3 covers the inclusion of stiffening frames.

Methods for solving the structural-fluid coupled systems will be discussed in Chapter III.

1. Unframed, Capped Cylindrical Shell with Fluid Loading

The equations of motion for a finite, simply-supported cylindrical shell appear in a number of standard references, e.g., Ref. 35.

$$L_1 u + L_2 q + L_3 w = - \frac{a^2 (1-\nu)^2}{Eh} \left\{ p_z^C(\phi) \delta(z+L/2a) - p_z^C(\phi) \delta(z-L/2a) \right\} \quad (\text{II.B-1a})$$

$$L_4 u + L_5 q + L_6 w = 0 \quad (\text{II.B-1b})$$

$$L_7 u + L_8 q + L_9 w = - \frac{a^2 (1-\nu^2)}{Eh} \left\{ F_r(z, \phi) - p_r(z, \phi) \right\} \quad (\text{II.B-1c})$$

where u , q , w stand respectively for axial, tangential (or circumferential), and radial displacements; the shell has radius a , Poisson ratio ν , thickness h , and Young's modulus E . Figure II.2 shows the generic geometry. The effect of the caps on the shell has been modeled as a set of (unknown) reaction pressures $p_z^{C,L,R}$ in Eq. II.B-1a; shortly, $p_z^{C,L,R}$ will be expressed in terms of cap displacements through the dynamic equation for cap motion. F_r and p_r are respectively the externally applied drive and radiation loading on the axial surface of the cylinder. The operators L_1, \dots, L_9 given in Appendix II.B correspond to the Donnell-Mushtari thin-shell theory.

For a simply supported cylinder, we let

$$u = \sum_n \sum_m u_{nm} \cos n\phi \cos \frac{m\pi a}{L} (z+L/2a) \quad (\text{II.B-2a})$$

$$q = \sum_n \sum_m q_{nm} \sin n\phi \sin \frac{m\pi a}{L} (z+L/2a) \quad (\text{II.B-2b})$$

$$w = \sum_n \sum_m w_{nm} \cos n\phi \sin \frac{m\pi a}{L} (z+L/2a) \quad (\text{II.B-2c})$$

and also

$$p_{z_{L,R}}^{C_{L,R}}(\phi) \delta(z+L/2a) = \sum_n \sum_m p_{z_{nm}}^{C_{L,R}} \cos n\phi \cos \frac{m\pi a}{L} (z+L/2a) \quad (\text{II.B-3a})$$

$$p_{r,F_r}(\phi, z) = \sum_n \sum_m (p_{r_{nm}}^{F_r}) \cos n\phi \sin \frac{m\pi a}{L} (z+L/2a) \quad (\text{II.B-3b})$$

Substituting Eqs. II.B-2,3 into II.B-1 one obtains

$$\begin{bmatrix} A_1 & A_2 & A_3 \\ A_4 & A_5 & A_6 \\ A_7 & A_8 & A_9 \end{bmatrix} \begin{Bmatrix} u_{nm} \\ q_{nm} \\ w_{nm} \end{Bmatrix} = - \frac{a^2 (1-\nu^2)}{Eh} \begin{Bmatrix} p_{z_{nm}}^{C_L} - p_{z_{nm}}^{C_L} \\ 0 \\ F_{r_{nm}} - p_{r_{nm}} \end{Bmatrix} \quad (\text{II.B-4})$$

where the quantities A_1 through A_9 are given in Appendix II.B(1).

2. Equation for Cap Motion

Each of the two end caps is assumed to have mass M_c and to move rigidly in the axial direction under cap fluid loading, drive and shell reaction forces. The fluid loading on the caps is assumed evenly distributed and thus constant over the radius as measured from the caps' center, whereas shell reaction forces are taken as acting only at the shell-cap circumferential interface. For example, for the left cap at $z=-L/2a$.

$$-i\omega M_c V^{C_L} = a^2 \int_0^1 dr r \left\{ p_{z_{n=0}}^{C_L} \delta(r-1) + \frac{F_{z_{n=0}}^{C_L} \delta(r-r_o)}{r_o} + p_{z_{n=0}}^{C_{L,f}} \right\} \quad (\text{II.B-5})$$

where we have accounted for the possibility of an externally applied drive at radial position r_o ; $p_{z_{n=0}}^{C_{L,f}}$ denotes fluid loading, and $p_{z_{n=0}}^{C_L}$ the reaction

with the shell structure; $M_c = \rho_s \tilde{t} \pi a^2$, \tilde{t} = cap thickness, and ρ_s = density of metal. Eq. II.B-5 thus becomes

$$\rho_c \tilde{Z}^{cap} v_{n=0}^C = p_{z_{n=0}} + F_{z_n}^C + \frac{1}{2} p_{z_n}^{C_{L,f}} \quad (\text{II.B-6})$$

where for convenience of later analysis we expressed \tilde{Z}^{cap} , the cap reactive impedance normalized by c , as

$$\tilde{Z}^{cap} = -ika \left(\frac{\rho_c}{\rho} \right) (\tilde{t}/a) \pi \quad (\text{II.B-7})$$

where ρ_c is cap material density. A similar expression may be derived for $v_{n=0}^{C_R}$, the axial velocity for the right cap. Again, the present model allows for a finite left side in Eq. II.B-6 only for $n=0$. As discussed in Section II.A, more complex cap modes could be modeled to match higher n shell modes but for simplicity and tractability this is not pursued here. Letting now $z = \pm L/2a$ in Eq. II.B-2a we observe that

$$v_{n=0}^C = - \sum_{m=0} U_{(n=0)m} \quad (\text{II.B-8a})$$

$$v_{n=0}^{C_R} = \sum_{m=0} U_{(n=0),m} (-1)^m \quad (\text{II.B-8b})$$

where $U_{nm} = -i\omega u_{nm}$ which from the system in Eq. II.B-4 has solution

$$U_{nm} = i\omega \frac{a^2(1-v^2)}{Eh} \left\{ B_1 (p_{z_{nm}}^C - p_{z_{nm}}^L) + B_3 (F_{r_{nm}} - p_{r_{nm}}) \right\} \quad (\text{II.B-9})$$

Constants B_1, B_3 are given in Appendix II.B(2).

Since

$$\delta(z-L/2a) = \sum_{m=0} \frac{2\varepsilon_m (-1)^m}{L/a} \cos \frac{m\pi a}{L} (z+L/2a) \quad (\text{II.B-10a})$$

$$\delta(z+L/2a) = \sum_{m=0}^{\infty} \frac{2\epsilon_m}{L/a} \cos \frac{m\pi a}{L} (z+L/2a) \quad (\text{II.B-10b})$$

where

$$\epsilon_m = \begin{cases} 1/2 & \text{for } m = 0 \\ 1 & \text{for } m \geq 1 \end{cases}$$

Thus, it follows that

$$p_{z_{nm}}^L = \frac{2\epsilon_m}{L/a} p_{z_n}^L \quad (\text{II.B-11a})$$

$$p_{z_{nm}}^R = \frac{2\epsilon_m (-1)^m}{L/a} p_{z_n}^R \quad (\text{II.B-11b})$$

where $p_{z_n}^{L,R}$ are the same shell-cap reaction forces appearing in the equation for the cap dynamics, e.g., Eq. II.B-6. These may be eliminated by substituting Eqs. II.B-11 into II.B-9. Using Eq. II.B-6 for $V_{n=0}^L$ and the corresponding right-cap equation yields:

$$\begin{aligned} & \left[1 + \frac{i\omega a^2 (1-\nu^2)}{Eh} \cdot \frac{2\rho c \tilde{Z}^{\text{cap}}}{L/a} \left(\sum_{m=0}^{\infty} B_1 \epsilon_m \right) \right] V_{n=0}^L = \\ & \frac{i\omega a^2 (1-\nu^2)}{Eh} \left\{ \frac{2\rho c \tilde{Z}^{\text{cap}}}{L/a} \left(\sum_{m=0}^{\infty} B_1 (-1)^m \epsilon_m \right) V_{n=0}^R \right. \\ & + \frac{2}{L/a} \left(\sum_{m=0}^{\infty} B_1 \epsilon_m \right) F_{z_{(n=0)}}^L - \frac{2}{L/a} \left(\sum_{m=0}^{\infty} B_1 (-1)^m \epsilon_m \right) F_{z_{(n=0)}}^R \\ & + \frac{1}{L/a} \left(\sum_{m=0}^{\infty} B_1 \epsilon_m \right) p_n^L - \frac{1}{L/a} \left(\sum_{m=0}^{\infty} B_1 (-1)^m \epsilon_m \right) p_n^R \\ & \left. - \sum_{m=1}^{\infty} B_3 F_{r_{nm}} + \sum_{m=1}^{\infty} B_3 p_{r_{nm}} \right\} \quad (\text{II.B-12a}) \end{aligned}$$

$$\begin{aligned}
\left[1 + \frac{i\omega a^2 (1-v^2)}{Eh} + \frac{2\rho c \tilde{Z}^{\text{cap}}}{L/a} \left(\sum_{m=0} B_1 \epsilon_m \right) \right] v_{n=0}^{C_R} = \\
\frac{i\omega a^2 (1-v^2)}{Eh} \left\{ \frac{2\rho c \tilde{Z}^{\text{cap}}}{L/a} \left(\sum_{m=0} B_1 \epsilon_m \right) v_{n=0}^{C_L} - \frac{2}{L/a} \left(\sum_{m=0} B_1 (-1)^m \epsilon_m \right) F_{z(n=0)}^{C_L} \right. \\
+ \frac{2}{L/a} \left(\sum_{m=0} B_1 \epsilon_m \right) F_{z(n=0)}^{C_R} - \frac{1}{L/a} \left(\sum_{m=0} B_1 (-1)^m \epsilon_m \right) p_n^{C_L} \\
\left. + \frac{1}{L/a} \left(\sum_{m=0} B_1 (-1)^m \epsilon_m \right) p_n^{C_R} + \sum_{m=1} (-1)^m B_3 F_{r_{nm}} - \sum_{m=1} (-1)^m B_3 p_{r_{nm}} \right\}
\end{aligned}
\tag{II.B-12b}$$

where we have simplified the notation by calling $p_{z_n}^{C_R, f}$, $p_{z_n}^{C_L, f}$ simply $p_n^{C_R}$, $p_n^{C_L}$ -- the fluid pressures on the right and left caps as denoted in Section II.A; and similarly replaced $p_{r_{nm}}$ by p_{nm} , the modal pressures for the shell part.

From the system in Eq. II.B-4 one may also solve for velocities $v_{nm} = -i\omega w_{nm}$ on the cylindrical part of the surface. Substituting all we know so far into that solution yields that

$$\begin{aligned}
v_{(n=0)m} = \frac{i\omega a^2 (1-v^2)}{Eh} \left\{ \frac{2\epsilon_m}{L/a} B_7 \left[\rho c \tilde{Z}^{\text{cap}} \left(v_{n=0}^{C_L} - (-1)^m v_{n=0}^{C_R} \right) \right. \right. \\
\left. \left. - \left(F_{z(n=0)}^{C_L} - (-1)^m F_{z(n=0)}^{C_R} \right) - \frac{1}{2} \left(p_n^{C_L} - (-1)^m p_n^{C_R} \right) \right] + B_9 (F_{r_{nm}} - p_{nm}) \right\}
\end{aligned}
\tag{II.B-13}$$

In the above $\epsilon_m = 1$ always since $m \geq 1$. For $n \geq 1$ the cap velocities $v_n^{C_L, R}$ are identically zero and the cap fluid loading does not affect the motion of the cylindrical surface. Thus for $n \geq 1$, Eq. II.B-13 simplifies to

$$V_{n \geq 1, m} = \frac{i\omega a^2 (1-v^2)}{Eh} B_9 (F_{r_{nm}} - p_{nm}) \quad (\text{II.B-14})$$

We now collect the results in Eqs. II.B-12a, b and B-13 for $n=0$, and II.B-14 for $n \geq 1$ into structural systems for $n=0, \geq 1$ respectively. We recognize that $i\omega a^2 (1-v^2)/Eh = i\omega (a/h) (\rho_s c_p (1-i\eta))$ (see Appendix II.B(1)), and define the following three constants

$$K_1 = 2i\Omega (a/h) (\rho/\rho_s) (c/c_p) (a/L) \tilde{Z}^{\text{cap}}$$

$$K_2 = \sum_{m=0} B_1 \epsilon_m$$

$$K_3 = \sum_{m=0} B_1 (-1)^m \epsilon_m$$

Then for $n=0$ we have that

$$\rho c \begin{bmatrix} 1 & 0 & 0 & . & . & 0 \\ 0 & 1 & 0 & . & . & . \\ 0 & 0 & . & . & 0 & . \\ . & . & . & . & . & 0 \\ . & . & . & 0 & 1 & 0 \\ 0 & . & . & . & 0 & 1 \\ \hline 0 & . & . & . & . & 0 \\ 0 & . & . & . & . & 0 \end{bmatrix} \begin{bmatrix} K_1 B_7^{m=1} \\ K_1 B_7^{m=2} \\ . \\ . \\ . \\ K_1 B_7^{m=M} \\ \hline 1+K_1 K_2 \\ -K_1 K_3 \end{bmatrix} \begin{bmatrix} K_1 B_7^{m=1} \\ -K_1 B_7^{m=1} \\ . \\ . \\ . \\ (-1)^{M+1} K_1 B_7^{m=M} \\ \hline -K_1 K_3 \\ 1+K_1 K_2 \end{bmatrix} \left\{ \begin{array}{l} V_{nm=1} \\ V_{nm=2} \\ . \\ . \\ . \\ V_{nm=M} \\ \hline V_{n=0}^{C_L} \\ \hline V_{n=0}^R \end{array} \right\} =$$

$$\frac{\Omega\left(\frac{a}{h}\right)\left(\frac{\rho}{\rho_s}\right)\left(\frac{c}{c_p}\right)}{\sqrt{1 - i\eta}} \begin{bmatrix} B_9^{m=1} & 0 & \dots & 0 & -B_7^{m=1}/(L/a) & -B_7^{m=1}/(L/a) \\ 0 & B_9^{m=2} & & \cdot & -B_7^{m=2}/(L/a) & +B_7^{m=2}/(L/a) \\ \cdot & & \cdot & \cdot & \cdot & \cdot \\ \cdot & & & 0 & \cdot & \cdot \\ 0 & \dots & & 0 & B_9^{m=M} & -B_7^{m=M}/(L/a) & (-1)^M B_7^{m=M}/(L/a) \end{bmatrix} \begin{Bmatrix} p_{nm=1} \\ p_{nm=2} \\ \cdot \\ \cdot \\ p_{nm=M} \end{Bmatrix} +$$

$$\begin{bmatrix} -B_3^{m=1} & -B_3^{m=2} & \dots & -B_3^{m=M} & K_2/(L/a) & -K_3/(L/a) \\ -B_3^{m=1} & +B_3^{m=2} & \dots & (-1)^M B_3^{m=M} & -K_3/(L/a) & K_2/(L/a) \end{bmatrix} \begin{Bmatrix} C_L \\ p_n \\ C_R \\ p_n \end{Bmatrix}$$

$$\frac{\Omega\left(\frac{a}{h}\right)\left(\frac{\rho}{\rho_s}\right)\left(\frac{c}{c_p}\right)}{\sqrt{1 - i\eta}} \begin{bmatrix} B_9^{m=1} & 0 & \dots & 0 & -2B_7^{m=1}/(L/a) & -2B_n^{m=1} \\ 0 & B_9^{m=2} & & \cdot & -2B_7^{m=2}/(L/a) & +2B_7^{m=2}/(L/a) \\ \cdot & & \cdot & 0 & \cdot & \cdot \\ \cdot & & & 0 & \cdot & \cdot \\ 0 & \dots & & 0 & B_9^{m=M} & -2B_7^{m=M} & (-1)^M 2B_7^{m=M}/(L/a) \end{bmatrix} \begin{Bmatrix} F_{rnm=1} \\ F_{rnm=2} \\ \cdot \\ \cdot \\ F_{rnm=M} \end{Bmatrix}$$

$$\begin{bmatrix} -B_3^{m=1} & -B_3^{m=2} & \dots & -B_3^{m=M} & 2K_2/(L/a) & 2K_3/(L/a) \\ -B_3^{m=1} & +B_3^{m=2} & \dots & (-1)^M B_3^{m=M} & -2K_3/(L/a) & 2K_2/(L/a) \end{bmatrix} \begin{Bmatrix} C_L \\ F_{z_{n=0}} \\ C_R \\ F_{z_{n=0}} \end{Bmatrix}$$

(II.B-15)

For $n \geq 1$ the structural system is purely diagonal

$$\rho c \begin{bmatrix} 1 & & & 0 \\ & 1 & & \\ & & \ddots & \\ 0 & & & 1 \end{bmatrix} \begin{Bmatrix} v_{nm=1} \\ v_{nm=2} \\ \vdots \\ v_{nm=M} \end{Bmatrix} =$$

$$\frac{-i\Omega(a/h)(\rho/\rho_s)(c/c_p)}{\sqrt{1-i\eta}} \begin{bmatrix} B_9^{m=1} & 0 & \dots & 0 \\ 0 & B_9^{m=2} & & \\ \vdots & & \ddots & \\ 0 & \dots & 0 & B_9^{m=M} \end{bmatrix} \begin{Bmatrix} p_{nm=1} \\ p_{nm=2} \\ \vdots \\ p_{nm=M} \end{Bmatrix}$$

$$+ \frac{i\Omega(a/h)(\rho/\rho_s)(c/c_p)}{\sqrt{1-i\eta}} \begin{bmatrix} B_9^{m=1} & 0 & \dots & 0 \\ 0 & B_9^{m=2} & & \\ \vdots & & \ddots & \\ 0 & \dots & 0 & B_9^{m=M} \end{bmatrix} \begin{Bmatrix} F_{r_{nm=1}} \\ F_{r_{nm=2}} \\ \vdots \\ F_{r_{nm=M}} \end{Bmatrix} \quad (\text{II.B-16})$$

3. The Frame-Stiffened Cylindrical Shell

The effect of N_f internal stiffening ring-shaped frames is modeled here as a set of N_f initially unknown, radially directed (normal to the shell surface) modal reaction forces. The true drive may be taken as acting on the shell through a particular ring frame, or as acting directly on the shell skin. The procedure for the solution of the frame reactions requires that displacements at every axial frame location be computed due to each virtual load in the presence of fluid loading. An opposite system of virtual reaction forces acts on the ring frames, for which a second set of equations relating frame displacements to reactions may be written with knowledge of each frame's structural impedance. Finally, equating shell and frame displacements at their interface yields a linear system of equations for the unknown reactions.

In the present model we enforce continuity of radial and tangential displacements between shell and frames (w and q in Eq. II.B-1); so that for the shell not only must we calculate the radial influence of the superposed

system of virtual radial loads, but also the radial influence of virtual tangential forces (equal by reciprocity to also needed tangential displacements due to radial forces), and tangential displacements for virtual tangential forces. However, for typical submarine shell parameters the latter may be assumed to be negligible relative to the others. Therefore, if N_f is used to denote the number of stiffening frames, the order of the system to obtain the reaction vector is $2N_f$; and each of the $2N_f \times 2N_f$ system entries is a combined fluid-loaded admittance coefficient for the shell and frames. The known right-hand side is a function of the actual applied drive. After the radial components of the frame reactions have been so determined, they are used together with the external drive (if applied directly to shell skin) in Eqs. II.B-1c as the total system of $F_r(\phi, z)$ external forces driving the shell.

We calculate the modal radial velocity and surface pressure vectors for the cylindrical part of the boundary by solving the coupled systems in Eqs. II.A-13, 14 and II.B-15, 16 for a virtual n-modal load F_n^j acting in frame location j. Thus,

$$[v_{nm=1}^j, v_{nm=2}^j, \dots, v_{nm=M}^j]^T \quad (\text{II.B-17a})$$

$$[p_{nm=1}^j, p_{nm=2}^j, \dots, p_{nm=M}^j]^T \quad (\text{II.B-17b})$$

is known due to

$$\delta(z-z_j) \sum_n \left(\frac{F_{r_n}^j/a}{\rho c} \right) \cos n\phi$$

where the r subscript on $F_{r_n}^j$ denotes the radial direction.

The corresponding tangential modal velocity vector $[v_{nm=1}^j, v_{nm=2}^j, \dots, v_{nm=M}^j]^T$ may be calculated from the relationship $(v_{nm} = -i\omega q_{nm})$

$$\begin{pmatrix} A_8 & -\frac{A_7}{A_4} & A_5 \end{pmatrix} v_{nm} = \begin{pmatrix} \frac{A_7}{A_4} & A_6 & -A_9 \end{pmatrix} v_{nm} + \frac{i\Omega(a/h)}{\rho_s c_p \sqrt{1-i\eta}} \{F_{r_n}^j/a - p_{nm}^j\} \quad (\text{II.B-18})$$

so that radial and tangential velocities may be computed at axial frame locations z_i , $i=1, \dots, N_f$, through

$$v_n(z_i), v_n(z_i) = \sum_m (v_{nm}, v_{nm}) \sin \frac{m\pi a}{L} (z_i + L/2a) \quad (\text{II.B-19})$$

Thus, defining the admittance coefficients c_{nij} , \bar{c}_{nij} by

$$c_{nij} = \frac{v_n^j(z_i)}{\left(\frac{F_{r_n}^j/a}{\rho c} \right)} \quad (\text{II.B-20a})$$

$$\bar{c}_{nij} = \frac{v_n(z_i)}{\left(\frac{F_{r_n}^j/a}{\rho c} \right)} \quad (\text{II.B-20b})$$

$$\tilde{c}_{nij} = \frac{v_n(z_i)}{\left(\frac{F_{t_n}^j/a}{\rho c} \right)} \approx 0 \quad (\text{II.B-20c})$$

where the t subscript on $F_{t_n}^j$ denotes tangential, we may therefore write that the total velocity at a shell surface point z_i is given by

$$v_n(z_i) = \sum_{j=1}^{N_f} \left(\frac{F_{r_n}^j/a}{\rho c} \right) c_{nij} + \sum_{j=1}^{N_f} \left(\frac{F_{t_n}^j/a}{\rho c} \right) \bar{c}_{nij} \quad (\text{II.B-21a})$$

$$v_n(z_i) \approx \sum_{j=1}^{N_f} \left(\frac{F_{r_n}^j/a}{\rho c} \right) \bar{c}_{nij} \quad (\text{II.B-21b})$$

In the above it is assumed that the applied external drive acts indirectly on the shell through a frame so that all shell forces are virtual. For the case when a radial drive distribution acts directly on the shell the right sides of Eqs. II.B-21a,b would contain respectively the additional terms

$$\frac{F_{on}}{\rho c} c_{ni}^o, \quad \frac{F_{on}}{\rho c} \bar{c}_{ni}^o$$

where c_{ni}^o denotes the loading distribution's radial influence at position i , and \bar{c}_{ni}^o the tangential influence.

4. Frame Equations

The statement of Newton's second law for the j^{th} frame takes the form

$$\frac{\tilde{F}_n^j}{\rho c} = Z_{11}^j v_n(z_j) + Z_{13}^j v_n(z_j) \quad (\text{II.B-22a})$$

$$\frac{\tilde{F}_t^j}{\rho c} = Z_{31}^j v_n(z_j) + Z_{33}^j v_n(z_j) \quad (\text{II.B-22b})$$

where the frame impedances Z_{11}, \dots, Z_{33} have been derived by Harari²⁸, and are listed here in Appendix II.B(2). The net force \tilde{F}_{r_n} is given by

$$\tilde{F}_{r_n} = \begin{cases} F_{r_{no}} - F_{r_n} & \text{for drive on frame} \\ -F_{r_n} & \text{for drive not on frame} \end{cases}$$

A similar expression applies for \tilde{F}_t . Equations II.B-22a,b may be inverted in order to obtain explicit forms for v_n, v_n , which then may be set equal to shell displacements to yield the final system for the unknown reactions in terms of a combined admittance matrix $[A]^{\text{comb}}$:

As earlier stated, iteration schemes such as those proposed here require also a number of operations proportional to N^2 , the precise number BN^2 depending on the convergence rate, i.e., on the number of matrix-vector products required to achieve the desired level of accuracy (each matrix-vector product is an N^2 operation). On the other hand, exact standard solvers such as Gaussian elimination require CN^3 operations, with $C=O(1)$.

The following ratio of Total Computational Efforts (TCE) therefore describes the savings potential of iterative methods over exact:

$$\frac{(\text{TCE})_{\text{Iteration}}}{(\text{TCE})_{\text{Exact}}} = \frac{AN^2 + BN^2}{AN^2 + CN^3} \quad (\text{III.E-1a})$$

$$\sim \left(\frac{A+B}{C}\right) \cdot \frac{1}{N} \quad \text{as } N \rightarrow \infty \quad (\text{III.E-1b})$$

where, again, the first term in both numerator and denominator is a measure of system generation effort, and the second terms denote actual system-solving times. Thus, substantial savings could result wherever the needed number of iteration steps is much less than the system order N .

where

$$[\tilde{A}] = [C_2^S] - [I^S - B_2^S][1/C_1^S] \quad (\text{III.D-8})$$

From here on the iteration technique follows the pattern of technique 2 previously discussed for $n=0$: For the $k=0$ starting step we set $x_2(M+1) = x_2(M+2) = 0$ and obtain $\{x_1^S\}^{k=0}$ from Eq. III.D-7 by solving the latter in K_2 (inner) Jacobi steps with the $[B_{\tilde{A}}]$ -matrix corresponding to $[\tilde{A}]$ above. The cap mode Eq. III.D-5c is then solved either exactly or approximately, depending for a more general case on the order of the partitioned-off $[\tilde{C}]$ subsystem. For the present case, $[\tilde{C}]$ is 2×2 and an exact solution is used in Chapter IV applications. With these values of $\{x_2(M+1), x_2(M+1)\}^T$ $k=0$ on the RHS of Eq. III.D-7, a new $\{x_1^S\}^{k=1}$ vector is obtained in K_2 iteration steps and so on. As in Method 2 for $n=0$, the whole procedure here is repeated K_1 outer steps. Also, as the alternate algorithm for $n=0$, this one for $n \geq 1$ appears to be nonstationary but again with a necessary convergence criterion: $S(B_{\tilde{A}}) < 1$. This second algorithm for $n \geq 1$ was applied successfully whenever Method 1 was found to diverge.

E. Economic Advantage of the Iterative Methods

The total cost of solving fluid-structure interaction problems has two clearly separate contributions: (1) the generation of the systems, i.e., filling up every matrix entry; and (2) the solution process applied to these systems. In a finite-difference or finite-element formulation N control points are chosen to represent the surface of the structure and the generated fluid and structural systems therefore contain $N \times N$ elements. The work needed to fill up each entry depends on the character of the differential equation describing the structure and on the numerical integration techniques chosen to perform local evaluations of the Helmholtz integral; hopefully, both operations can be accomplished with many fewer than N multiplications and additions for typically large systems. Thus, the total cost of system generation may be denoted by AN^2 , where A is a constant.

2. Method 2

Referring back to Eq. II.B-16, we recall that matrix $[C_1^S]$, the structural modal admittance matrix for modes on the shell surface alone excluding cap modes, is diagonal and thus readily invertible if necessary. This is due to the separability of this part of the geometry. The second iterative algorithm for $n \geq 1$ presented next exploits this feature of the model formulation without invalidating our basic policy of noninversion, since the latter is cost-effective mostly, and thus strictly observed, for the fluid system. More importantly, since structural systems resulting from the in-vacuo finite-element analysis of a general structure normally are in terms of an impedance rather than an admittance matrix, no inversion is necessary. Also, because such matrices are typically heavily banded, the product $[I-B_2][1/C_1^S]$ that arises in the following analysis would involve many fewer operations than the N^3 otherwise required if the impedance matrix $[1/C_1^S]$ were fully populated.

Following an approach similar to that for $n=0$'s second technique, we write that now for $n \geq 1$

$$\{x_1^S\} = [C_1^S]\{x_2^S\} + \{b^S\} \quad (\text{III.D-5a})$$

$$\begin{aligned} [I^S - B_2^S]\{x_2^S\} + \{(I-B_2)_{i,M+1}\}x_{2(M+1)} + \{(I-B_2)_{i,M+2}\}x_{2(M+2)} \\ = [C_2^S]\{x_1^S\} \end{aligned} \quad (\text{III.D-5b})$$

$$[\tilde{C}] \begin{Bmatrix} x_{2(M+1)} \\ x_{2(M+2)} \end{Bmatrix} = \begin{Bmatrix} \sum_{i=1}^M (\hat{C}_2)_{M+1,i} x_1(i) - (I-B_2)_{M+1,i} x_2(i) \\ \sum_{i=1}^M (\hat{C}_2)_{M+2,i} x_1(i) - (I-B_2)_{M+2,i} x_2(i) \end{Bmatrix} \quad (\text{III.D-5c})$$

Eq. III.D-5a now is inverted to solve for $\{x_2^S\}$:

$$\{x_2^S\} = [1/C_1^S]\{x_1^S\} - [1/C_1^S]\{b^S\} \quad (\text{III.D-6})$$

which upon substitution into III.D-5b yields

$$\begin{aligned} [\tilde{A}]\{x_1^S\} = - [I^S - B_2^S][1/C_1^S]\{b^S\} + \{(I-B_2)_{i,M+1}\}x_{2(M+1)} \\ + \{(I-B_2)_{i,M+2}\}x_{2(M+2)} \end{aligned} \quad (\text{III.D-7})$$

where $[B_2]$ is still given by Eq. III.B-4c. The nonsquare matrix $[\hat{C}_2]$ is given by $[D_Y]^{-1}[\hat{\delta}]$; $[C_1^S]$ is simply $[\beta_1^S]$ of Eq. III.B-2a, a diagonal matrix containing shell-surface modal structural admittances as defined by Eq. II.B-16.

1. Method 1

Analogous to Eqs. III.C-1a and III.C-1b for $n=0$, for $n \geq 1$ we have

$$x_1^{s k} = C_1^S x_2^{s k-1} + b^s \quad (\text{III.D-2a})$$

$$x_2^k = B_2 x_2^{k-1} + \hat{C}_2 x_1^{s k-1} \quad (\text{III.D-2b})$$

for which a convergence criterion is established by writing Eqs. III.D-2a and III.D-2b in equivalent combined form:

$$\begin{matrix} M \\ M+2 \end{matrix} \left\{ \begin{array}{c|c|c} \overbrace{\begin{matrix} I^S & -C_1^S & \begin{matrix} 0 & 0 \\ \downarrow & \downarrow \\ 0 & 0 \end{matrix} \end{matrix}}^{\begin{matrix} M \\ M \end{matrix}} \\ \hline \begin{matrix} -\hat{C}_2 & I-B_2 \end{matrix} \end{array} \right\} \begin{Bmatrix} x_1^s \\ x_2 \end{Bmatrix} = \begin{Bmatrix} b \\ 0 \\ \downarrow \\ 0 \end{Bmatrix} \quad (\text{III.D-3})$$

With $\{\tilde{x}\} = [x_1^s, x_2]^T$, iterations Eqs. III.D-2a and III.D-2b may be shown to be equivalent to the Jacobi method,

$$\tilde{x}^k = \tilde{B} \tilde{x}^{k-1} + \tilde{b} \quad (\text{III.D-4a})$$

where

$$[\tilde{B}] = \left[\begin{array}{c|c|c} 0 & C_1^S & \begin{matrix} 0 & 0 \\ \downarrow & \downarrow \\ 0 & 0 \end{matrix} \\ \hline \hat{C}_2 & B_2 & \end{array} \right] \quad (\text{III.D-4b})$$

and $\tilde{x} = [x_1^s, x_2]^T$. Convergence is obtained when all eigenvalues of $[\tilde{B}]$ have magnitude less than 1, i.e., $S(\tilde{B}) < 1$.

$$\begin{bmatrix} I^S & -C_1^S \\ -C_2^S & I^S - B_2^S \end{bmatrix} \begin{Bmatrix} x_1^S \\ x_2^S \end{Bmatrix}^{k=1} = \begin{Bmatrix} g_1 \\ g_2 \end{Bmatrix}^{k=1} \quad (\text{III.C-13})$$

Eq. III.C-13 may now be solved iteratively as was Eq. III.C-11, i.e., in K_2 iteration steps. The procedure is stopped when $k=K_1$ steps.

We note that while $[\tilde{B}^S]$ is the same matrix as for the $k=0$ iteration, the effective drive vector $\{b^S\}^{k=1}$ is now clearly different. The method therefore is non-stationary. As indicated in Ref. 29, however, the fact that $[\tilde{B}^S]$ is constant vs. k keeps the convergence analysis for this subsystem simple, and a necessary condition to converge now is that $S(\tilde{B}^S) < 1$, which is a different criterion from that obtained previously for method 1 given the basic differences in system matrix partitioning and the fact that the total scheme may now actually be semi-exact. We note that this second iteration scheme uses two nested algorithms: The outer is performed K_1 times and corresponds to the k counter; the inner one is executed K_2 times for each value of k .

D. Iteration Algorithms for $n \geq 1$

Two iteration procedures also are developed for the systems of Eqs. III.B-2a and III.B-2b. The first of these, however, is fundamentally no different from the method 1 for $n=0$, and the only purpose here is to show briefly how the analysis for convergence still follows the earlier format though the pressure and velocity vectors now differ in order, and also one of the coupling matrices, the $[\delta^S]$ matrix of Eq. III.B-26, is nonsquare. The second algorithm for $n \geq 1$ similarly involves some of the same elements as method 2 for $n=0$, but also applies a novel manipulation not previously employed for one of the system submatrices. In actual applications, this second algorithm was observed to converge when the first one did not.

Following earlier nomenclature, we now write Eqs. III.B-2a and III.B-2b in equivalent form suitable for iteration:

$$\{x_1^S\} = [C_1^S]\{x_2^S\} + \{b^S\} \quad (\text{III.D-1a})$$

$$\{x_2^S\} = [B_2]\{x_2^S\} + [\hat{C}_2]\{x_1^S\} \quad (\text{III.D-1b})$$

To start, $[\tilde{x}_1, \tilde{x}_2]^T$ is set to zero so that the $k=0$ iterate of $[g_1, g_2]^T$, denoted $[g_1^0, g_2^0]^T$, becomes $[g_1^0, g_2^0]^T = [b^S, 0]^T$ in Eq. III.C-8a, which then reads

$$\begin{bmatrix} I^S & -C_1^S \\ -C_2^S & I^S - B_2^S \end{bmatrix} \begin{Bmatrix} x_1^S \\ x_2^S \end{Bmatrix}^{k=0} = \begin{Bmatrix} g_1 \\ g_2 \end{Bmatrix}^{k=0} = \begin{Bmatrix} b^S \\ 0 \end{Bmatrix} \quad (\text{III.C-10})$$

Eq. III.C-10 may then be solved by Jacobi's method (or by other, more sophisticated techniques) in a set of K_2 J-iteration steps. We write,

$$\begin{Bmatrix} x_1^S \\ x_2^S \end{Bmatrix}_j^{k=0} = [\tilde{B}^S] \begin{Bmatrix} x_1^S \\ x_2^S \end{Bmatrix}_{j-1}^{k=0} + \{\tilde{b}^S\}^{k=0} \quad (\text{III.C-11})$$

where

$$[\tilde{B}^S] = [\tilde{D}^S]^{-1} \left\{ [\tilde{D}^S] - \begin{bmatrix} I^S & -C_1^S \\ -C_2^S & I^S - B_2^S \end{bmatrix} \right\} \quad (\text{III.C-12a})$$

$$\{\tilde{b}^S\} = [\tilde{D}^S]^{-1} \begin{Bmatrix} b^S \\ 0 \end{Bmatrix} \quad (\text{III.C-12b})$$

and where $[\tilde{D}^S]$ is a diagonal matrix containing Eq. III.C-10's diagonal elements. Again, the iteration in Eq. III.C-11 is carried out K_2 steps, after which the results so obtained for $[x_1^S, x_2^S]^{Tk=0}$ are used to compute $[\tilde{g}_1, \tilde{g}_2]^{Tk=0}$ from Eqs. III.C-9e and III.C-9f for use in Eqs. III.C-8b. The latter may now be solved iteratively in the same fashion as was $[x_1^S, x_2^S]^{Tk=0}$, or, if this subsystem is conveniently chosen to be small enough as in the present case, where it contains only the two cap unknowns, an exact solution for $[\tilde{x}_1, \tilde{x}_2]^{Tk=0}$ may be just as economical. These values of $[\tilde{x}_1, \tilde{x}_2]^{Tk=0}$ are then used to calculate, using Eqs. III.C-9c and III.C-9d, new values of g_1, g_2 , denoted $g_1^{k=1}, g_2^{k=1}$ for another k -iteration with Eqs. III.C-8a, which then reads:

$$\begin{bmatrix} I^S & -C_1^S \\ -C_2^S & I^S - B_2^S \end{bmatrix} \begin{Bmatrix} x_1^S \\ x_2^S \end{Bmatrix} = \begin{Bmatrix} g_1 \\ g_2 \end{Bmatrix} \quad (\text{III.C-8a})$$

$$\begin{bmatrix} \tilde{a} & -\tilde{C}_1 \\ -\tilde{C}_2 & \tilde{I} - \tilde{B}_2 \end{bmatrix} \begin{Bmatrix} \tilde{x}_1 \\ \tilde{x}_2 \end{Bmatrix} = \begin{Bmatrix} \tilde{g}_1 \\ \tilde{g}_2 \end{Bmatrix} \quad (\text{III.C-8b})$$

where

$$\{\tilde{x}_1\} = \begin{Bmatrix} x_1^{(M+1)} \\ x_1^{(M+2)} \end{Bmatrix} \quad (\text{III.C-9a})$$

$$\{\tilde{x}_2\} = \begin{Bmatrix} x_2^{(M+1)} \\ x_2^{(M+2)} \end{Bmatrix} \quad (\text{III.C-9b})$$

$$\{g_1\} = -\{\alpha_{i,M+1}\}x_1^{(M+1)} - \{\alpha_{i,M+2}\}x_1^{(M+2)} + \{(C_1)_{i,M+1}\}x_2^{(M+1)} + \{(C_1)_{i,M+2}\}x_2^{(M+2)} + \{b^S\} \quad (\text{III.C-9c})$$

$$\{g_2\} = -\{(I-B_2)_{i,M+1}\}x_2^{(M+1)} - \{(I-B_2)_{i,M+2}\}x_2^{(M+2)} + \{(C_2)_{i,M+1}\}x_1^{(M+1)} + \{(C_2)_{i,M+2}\}x_1^{(M+2)} \quad (\text{III.C-9d})$$

$$\{\tilde{g}_1\} = \begin{Bmatrix} \sum_{i=1}^M (C_1)_{M+1,i} x_2^S(i) \\ \sum_{i=1}^M (C_1)_{M+2,i} x_2^S(i) \end{Bmatrix} \quad (\text{III.C-9e})$$

$$\{\tilde{g}_2\} = -\begin{Bmatrix} \sum_{i=1}^M (I-B_2)_{M+1,i} x_2^S(i) \\ \sum_{i=1}^M (I-B_2)_{M+2,i} x_2^S(i) \end{Bmatrix} + \begin{Bmatrix} \sum_{i=1}^M (C_2)_{M+1,i} x_1^S(i) \\ \sum_{i=1}^M (C_2)_{M+2,i} x_1^S(i) \end{Bmatrix} \quad (\text{III.C-9f})$$

$$[\tilde{\alpha}] \begin{Bmatrix} x_1^{(M+1)} \\ x_1^{(M+2)} \end{Bmatrix} = [\tilde{C}_1] \begin{Bmatrix} x_2^{(M+1)} \\ x_2^{(M+2)} \end{Bmatrix} + \begin{Bmatrix} \sum_{i=1}^M (C_1)_{M+1,i} x_2^S(i) \\ \sum_{i=1}^M (C_1)_{M+2,i} x_2^S(i) \end{Bmatrix} \quad (\text{III.C-7b})$$

$$\begin{aligned} [I^S - B_2^S] \{x_2^S\} + \{(I - B_2)_{i,M+1}\} x_2^{(M+1)} + \{(I - B_2)_{i,M+2}\} x_2^{(M+2)} \\ = [C_2^S] \{x_1^S\} + \{(C_2)_{i,M+1}\} x_1^{(M+1)} + \{(C_2)_{i,M+2}\} x_1^{(M+2)} \end{aligned} \quad (\text{III.C-7c})$$

$$[\widetilde{I - B_2}] \begin{Bmatrix} x_2^{(M+1)} \\ x_2^{(M+2)} \end{Bmatrix} = - \begin{Bmatrix} \sum_{i=1}^M (I - B_2)_{M+1,i} x_2^S(i) \\ \sum_{i=1}^M (I - B_2)_{M+2,i} x_2^S(i) \end{Bmatrix} \quad (\text{III.C-7d})$$

$$+ [\tilde{C}_2] \begin{Bmatrix} x_1^{(M+1)} \\ x_1^{(M+2)} \end{Bmatrix} + \begin{Bmatrix} \sum_{i=1}^M (C_2)_{M+1,i} x_1^S(i) \\ \sum_{i=1}^M (C_2)_{M+2,i} x_1^S(i) \end{Bmatrix}$$

where $\{\alpha_{i,M+1}\}$, $\{\alpha_{i,M+2}\}$ are M-element vectors made up of the first M entries of the $[\alpha]$ matrix's $(M+1)^{\text{th}}$ column (Eq. III.B-1a). Similar definitions apply to $\{(C_1)_{i,M+1}\}$, $\{(I - B_2)_{i,M+2}\}$, etc. Eqs. III.C-7a and III.C-7c have order M. Also, it will be recalled that the upper left $M \times M$ submatrix $[I^S - B_1^S]$ of $[\alpha]$ is the identity matrix since $[B_1^S] \equiv 0$. Systems III.C-7b and III.C-7d have, for the present problem, an order of 2. A summation such as $\sum_{i=1}^M (I - B_2)_{M+1,i} x_2^S(i)$ denotes the inner product of the $(M+1)^{\text{th}}$ row of matrix $[I - B_2]$ with vector $\{x_2^S\}$. The 2×2 matrices $\tilde{\alpha}$, $\widetilde{I - B_2}$, \tilde{C}_1 , \tilde{C}_2 contain the bottom rightmost four elements $(M+1, M+1)$, $(M+1, M+2)$, $(M+2, M+1)$, $(M+2, M+2)$ of matrices α , $I - B_2$, C_1 , C_2 . It is important to point out that such partitioning of the two original systems should be mathematically completely arbitrary. For the physical problem at hand, however, such splitting sets aside the M-subvector of shell-surface effects from the two-element cap subvector by placing these quantities on opposite sides of the equations. If more cap modes had been used in the model, the two smaller subsystems would have been augmented accordingly. Eqs. III.C-7a through III.C-7c may also be written in combined form:

one realizes that expansions III.C-2 through III.C-4 are also obtained, to the identical order of error indicated, by simple Jacobi iteration of the combined system:

$$\begin{Bmatrix} x_1 \\ \vdots \\ x_2 \end{Bmatrix}^k = \begin{bmatrix} B_1 & C_1 \\ \vdots & \vdots \\ C_2 & B_2 \end{bmatrix} \begin{Bmatrix} x_1 \\ \vdots \\ x_2 \end{Bmatrix}^{k-1} + \begin{Bmatrix} b \\ \vdots \\ o \end{Bmatrix} \quad (\text{III.C-5})$$

or

$$\tilde{x} = \tilde{B}\tilde{x}^{k-1} + \tilde{b} \quad (\text{III.C-6})$$

where \tilde{x} is now a $2(M+1)$ -element vector, etc. Thus identifying the equivalence of algorithm III.C-1 to that corresponding to Eq. III.C-5 establishes its convergence criterion, which is now clearly that $S(\tilde{B}) < 1$. In summary, fixed-point iteration of joint structure-fluid systems converges if the matrix \tilde{B} , composed of the "self" matrices B_1, B_2 along its diagonal blocks, and of the "coupling" matrices C_1, C_2 as off-diagonals, has a spectrum all less than one in magnitude. Consistency proof of algorithm III.C-1 (i.e., that if for some $k=k^*$, $x_1^{k^*}, x_2^{k^*} = (x_1, x_2)^{\text{exact}}$, then $x_{1,2}^{k>k^*} = x_{1,2}^{\text{exact}}$ also) follows trivially from the standard single-system proof. Similarly, although at first algorithm III.C-1 does not appear to be stationary, i.e., that for both x_1 and x_2 the effective "self" matrix B_{eff} and associated known RHS b_{eff} appear to be functions of the iteration counter k rather than being k -independent quantities, the equivalent system of Eqs. III.C-5 and III.C-6 in fact shows that the algorithm is stationary and that for the combined system $\tilde{B}_{\text{eff}}, \tilde{b}_{\text{eff}}$ are just the constants $\tilde{B}, [b, o]^T$, where T denotes transpose. As previously stated, once the iteration scheme has been recast in terms of Eq. III.C-5, the latter may be changed to other techniques with accelerated convergence, e.g., SOR.

2. Method 2

Eqs. III.B-3a and III.B-3b may also be written as

$$\begin{aligned} [I^S - B_1^S] \{x_1^S\} + \{\alpha_{i,M+1}\} x_{1(M+1)} + \{\alpha_{i,M+2}\} x_{1(M+2)} \\ = [C_1^S] \{x_2^S\} + \{(C_1)_{i,M+1}\} x_{2(M+1)} + \{(C_1)_{i,M+2}\} x_{2(M+2)} + \{b^S\} \end{aligned} \quad (\text{III.C-7a})$$

C. Iteration Algorithms for $n=0$ 1. Method 1

To simplify the nomenclature, we drop, in some of what follows next, the curly and square brackets from quantities defined in Eqs. III.B-3, III.B-4 and III.B-5. The first algorithm we wish to explore for Eqs. III.B-3a and III.B-3b, is

$$x_1^k = B_1 x_1^{k-1} + C_1 x_2^{k-1} + b \quad (\text{III.C-1a})$$

$$x_2^k = B_2 x_2^{k-1} + C_2 x_1^{k-1} \quad (\text{III.C-1b})$$

To begin, one sets $x_2^0 = 0$ and $x_1^0 = b$. The solution $x_1^0 = b$ does not really correspond to the in-vacuo response of the structure because b is not $\alpha^{-1}f$, but instead only $D_\alpha^{-1}f$. The first few iterations go as follows:

$$k = 1 : x_1^1 = (I+B_1)b \quad (\text{III.C-2a})$$

$$x_2^1 = C_2 b \quad (\text{III.C-2b})$$

$$k = 2 : x_1^2 = (I+B_1+B_1^2)b + C_1 C_2 b \quad (\text{III.C-3a})$$

$$x_2^2 = (C_2 + C_2 B_1 + B_2 C_2)b \quad (\text{III.C-3b})$$

$$k = 3 : x_1^3 = (I+B_1+B_1^2+B_1^3)b + (C_1 C_2 + B_1 C_1 C_2 + C_1 B_2 C_2 + C_1 C_2 B_1)b \quad (\text{III.C-4a})$$

$$x_2^3 = (C_2 + C_2 B_1 + B_2 C_2 + B_2^2 C_2 + B_2 C_2 B_1 + C_2 B_1^2 + C_2 C_1 C_2)b \quad (\text{III.C-4b})$$

At first the analysis for convergence of x_1 and x_2 given the expansions Eqs. III.C-2 through III.C-4 appears complicated due to their coupling. For example, although the $\sum_{n=0}^{\infty} B_1^n b$ part of the solution for x_1 is reminiscent of iteration by Jacobi's method, there is also the $C_1 C_2 b + \dots$ part which necessarily changes the criterion of convergence from $S(B_1) < 1$ to something else (we follow the standard nomenclature of Ref. 29, where $S(B_1)$ stands for the spectrum of matrix B_1 ; thus $S(B_1) < 1$ states that all eigenvalues of B_1 must be less than 1 in magnitude). This situation is greatly simplified, however, when

purposes of iteration, Eqs. III.B-1a and III.B-1b for $n=0$ are now written as follows:

$$\{x_1\} = [B_1]\{x_1\} + [C_1]\{x_2\} + \{b\} \quad (\text{III.B-3a})$$

$$\{x_2\} = [B_2]\{x_2\} + [C_2]\{x_1\} \quad (\text{III.B-3b})$$

where

$$[B_1] = [D_\alpha]^{-1}[D_\alpha - \alpha] \quad (\text{III.B-4a})$$

$$[C_1] = [D_\alpha]^{-1}[\beta_1] \quad (\text{III.B-4b})$$

$$\{b\} = [D_\alpha]^{-1}[\beta_2]\{f\} \quad (\text{III.B-4c})$$

$$[B_2] = [D_\gamma]^{-1}[D_\gamma - \gamma] \quad (\text{III.B-4d})$$

$$[C_2] = [D_\gamma]^{-1}[\delta] \quad (\text{III.B-4e})$$

where D_α stands for the diagonal matrix composed of the diagonal elements of $[\alpha]$, and $[D_\gamma]$ for that corresponding to $[\gamma]$.

For $n \geq 1$, one may similarly write

$$\{x_1\} = [C_1^S]\{x_2\} + \{b^S\} \quad (\text{III.B-5a})$$

$$\{x_2\} = [B_2]\{x_2\} + [\hat{C}_2]\{x_1^S\} \quad (\text{III.B-5b})$$

where $\{b^S\} = \{f^S\}$, and $[B_2]$ is still given by Eq. III.B-4d. The $(M+2) \times M$ matrix $[\hat{C}_2]$ is given by the product $[D_\gamma]^{-1}[\delta^S]$.

For both the $n=0$ and $n \geq 1$ formulations we now develop two separate iteration algorithms and discuss their convergence. For example, for the $n=0$ problem we show that the two algorithms place upon the joint system different analytically derived convergence criteria, so that if one algorithm fails the other may possibly converge. The $n \geq 1$ problem is treated similarly. We will show in Chapter IV that over the frequency range explored at least one of the iteration techniques always converged to the exact solution.

which contains a free convergence-optimization parameter not analytically available in the J-method. However, no attempt is made here to adapt such SOR-type techniques to the basic algorithms, and we merely note that the savings realized as reported in Chapter IV, while significant, could thereby be made even greater.

B. System Equations

Equations II.A-13 and II.A-14 relate surface modes of fluid pressure to surface modes of fluid particle velocity for the nonseparable finite-cylinder geometry. Eqs. II.B-15 and II.B-16 relate, for the structure, vibrational response to an applied drive in the presence of the surrounding fluid, which contributes an unknown load distributed over the axial surface of the shell and end caps. Equating the surface response vector to the surface fluid particle velocity yields the final coupled systems from which $\{v\}$ and $\{p\}$ may be solved for a given drive load configuration $\{f\}$. Eqs. II.A-13 and II.B-15 apply for circumferential n -mode $n=0$, and Eqs. II.A-14 and II.B-16 apply for $n \geq 1$. Thus in summary, we have that for $n=0$,

$$[\alpha]\{v\} = [\beta_1]\{p\} + [\beta_2]\{f\} \quad (\text{III.B-1a})$$

$$[\gamma]\{p\} = [\delta]\{v\} \quad (\text{III.B-1b})$$

where every matrix contains $(M+2) \times (M+2)$ elements (each row and column contains M shell surface models plus one cap mode for each end of the cylinder, and each vector contains $M+2$ elements. For $n \geq 1$, we have

$$\{v^s\} = [\beta_1^s]\{p^s\} + [\beta_2^s]\{f^s\} \quad (\text{III.B-2a})$$

$$[\gamma]\{p\} = [\delta^s]\{v^s\} \quad (\text{III.B-2b})$$

where $[\gamma]$ and $\{p\}$ still have $(M+2) \times (M+2)$, and $M+2$ elements, respectively, but where now $\{v^s\}$ denotes the shortened M -element modal velocity vector which contains only shell-surface modes; we recall that this is the result of assuming that for $n \geq 1$ the caps are rigid. Similarly, the s -superscript on β_1 , β_2 , and f indicate a rank of M rather than $M+2$. Matrix $[\delta^s]$ contains $M+2$ rows, one for each of the $M+2$ pressure modes, for which a "diffracted" cap mode exists; and it contains M columns, one for the effect of each of the M shell-surface velocity modes on each pressure mode, including cap pressures. For

III. ITERATION TECHNIQUES FOR COUPLED STRUCTURAL-FLUID SYSTEMS FOR A FINITE CYLINDER

A. Introduction

The main purpose of the present study is to show whether fully populated structural-fluid systems as would arise from a finite-element or modal analysis of a nonseparable geometry may be solved iteratively and thus more economically than by the standard exact method, which effectively requires the inversion of at least one large matrix. For N -order coupled systems the exact solution requires a number of operations proportional to N^3 , while the corresponding number for iterative techniques is only N^2 . In our earlier investigation for the spherical shell¹ we demonstrated that well-established iterative techniques, e.g., Richardson's method and the so-called method of summability (Ref. 29, p. 345), could be applied to solve those versions of the Helmholtz and dynamic response equations. However, due to the separability of the spherical geometry, all matrices were effectively diagonal and the viability of this promising approach went untested for the more fundamentally complex general case.

In this chapter we develop iterative schemes to solve the finite cylinder problem as a representative of a wider class containing off-diagonal elements. For each procedure we discuss qualitatively conditions for successful iteration and attempt to explain why a specific technique may work when another fails. Actual numerical results and comparison to exact solutions are deferred to Chapter IV, where we also tabulate computational times vs. number and type of iterations. We find that the stability of computations often hinges on judicious system subpartitioning, a concept which has been commonly applied, though in somewhat different context, to the otherwise difficult treatment of certain ill-conditioned matrices.^{37,38,39}

One general comment applies to the convergence rate of essentially all the algorithms developed. Initially we show that the resulting expansion for parts of the iteration algorithms may be interpreted, after proper partitioning of matrices and vectors, as an application of fixed-point, or Jacobi, iteration (Ref. 29, p. 71). In some cases, the convergence rate of such J-method solutions could be improved substantially by a recasting to yield equivalent expansions corresponding to the Successive-Over-Relaxation (SOR) method (Ref. 29, p. 73),

$$\begin{aligned}
[A]^{\text{comb}} & [F_{r_n}^1, F_{r_n}^2, \dots, F_{r_n}^{N_f}; F_{t_n}^1, F_{t_n}^2, \dots, F_{t_n}^{N_f}]^T \\
& = F_{r_{no}} \begin{cases} [0, 0, \dots, \tilde{A}_i^*, 0, \dots, 0; 0, \dots, \tilde{B}_i^*, 0, \dots, 0]^T \\ [-c_1^0, -c_2^0, \dots, -c_{N_f}^0; -c_1^0, -c_2^0, \dots, -c_{N_f}^0]^T \end{cases}
\end{aligned} \tag{II.B-23}$$

where

$$\tilde{A}_i = \frac{z_{33}^i}{z_{11}^i z_{33}^i - z_{13}^i z_{31}^i} \tag{II.B-24}$$

$$\tilde{B}_i = \frac{-z_{31}^i}{z_{11}^i z_{33}^i - z_{13}^i z_{31}^i} \tag{II.B-25}$$

The right sides of Eq. II.B-23 are, (1) radial drive applied to the i^{th} frame, (2) radial drive acting directly on the shell. In the former case the model assumes that the applied drive distribution is concentrated at an axial location, while in the latter the radial drive has an arbitrary axial distribution. For both cases the circumferential drive distribution is arbitrary.

Again, upon solution of Eq. II.B-23, the combined radial loading system on the shell (reactions plus drive) becomes the effective shell drive which together with fluid loading appears forcing the structural systems of Eqs. II.B-15 and 16).

IV. APPLICATION OF THEORY

A. Introduction

The modal solution technique developed in Chapter II is now applied to the idealization of an actual structure for which extensive far-field measurements exist. Comparisons are made between theory and experiment. The iterative techniques of Chapter III are also applied and their results are compared to the exact solution.

The cylindrical structure shown in Figures IV.1a,b is one of five equal segments spliced to make up the total physical model in Ref. 40, which is a recent compilation of related experimental acoustic and response data collected by the Penn State group of Burroughs, Hayek, Hallander, and Bostian, in coordination with the ONR. Figure IV. 2 shows the simplified structure used for our calculations. Only the large joint-band frames have been kept as structural discontinuities, while all non-axisymmetric details, including axial stringers, have been eliminated. The simplified structure models what Ref. 40 calls the single, or inner, shell configuration. The predictions reported here are for a radial point drive applied either directly to the shell skin at the cylinder's midsection point, or at one of the two frames nearest the center. Structural parameters corresponding to Figure IV.2 are listed in Table IV.1.

For reasons outlined below having to do with system size and a limited computational budget, calculations were not carried out by the present method beyond 500 Hz. In order to continue the comparison of measurement to prediction to 2500 Hz, the fluid model was replaced by that for an infinite cylinder.

For clarity of presentation, the discussion and physical interpretation of predictions are given first at some length using the results obtained from solving the coupled systems exactly. We demonstrate subsequently that in fact all such exact results are also obtainable by iteration; thus, they may be viewed as converged solutions. The calculations describing just the iteration process are then displayed, both in frequency-sweep form and for directivity patterns. In order to present as many results as possible with

a minimum of repetition, some of the directivity patterns for the iterated solution correspond to frequencies which are different from those shown under the section for the exact results. We conclude that the iterative solution of fluid-loaded structural systems is both feasible and cost effective, at least in the low-frequency range where fluid loading has a global effect and is therefore less amenable to local modeling.

Since, as pointed out in Chapter III, convergence rates do not depend on the coupled systems' forcing function, iterated solutions will be presented only for the drive-on-skin case. Iterated solutions for the driven frame may be assumed to converge similarly.

B. System Size vs. Frequency

The modal theory of Chapter II requires that the series of simply-supported axial modes be truncated to yield coupled systems of finite rank. Here we determine quantitatively the minimum needed number M of such modes in terms of the frequency-dependent flexural wavenumber k_f for the shell plating. The minimum system size M must capture the shell flexural wavenumber k_f and if possible overshoot it by a certain margin. The inclusion of k_f in the m sum allows a fair representation of the structural far-field effect of each frame on the others, as required by off-diagonal frame admittance coefficients in Eq. II.B-20; while the additional modes are needed to calculate the diagonal, self admittance elements. Thus, we have that

$$M > \frac{L/a}{\pi} \cdot k_f a \quad (\text{IV.B-1})$$

With Eq. IV.B-1 serving as the criterion for system size, the minimum matrix order M vs frequency is given on the second column of Table IV.2. For reasons of economy, only the range $20 \text{ Hz} < f < 500 \text{ Hz}$ was investigated here and the value M was kept fixed at 30 for all calculations.

Values of the normalized acoustic wavenumber ka are given on the third column of Table IV.2. We note that for every frequency the below-coincidence condition $k_f a < ka$ is satisfied, so that every plating wavenumber listed has a subsonic trace speed and thus does not contribute directly to

the far-field. The coincidence frequency for the shell skin is approximately 35.3 kHz and therefore well above the range of interest here. However, for the shell in question the axial modal wavenumber $m\pi/(L/a)$ is given roughly by $m \cdot (.14)$, so that for example 500 Hz contains $m=1,2,3$ modes which are supersonic and therefore radiative; the rest, $4 < m < 30=M$, are subsonic. The relative contribution of subsonic and supersonic modes to the acoustic field has been discussed qualitatively in some detail in Chapter II, Section A.

C. Choice of Number of Circumferential Modes

In the theoretical model, stiffening frames represent axial structural discontinuities; however, since no circumferential discontinuities which would render the structure nonaxisymmetric are considered here either for the framing or for the skin, a structural criterion analogous to that of Eq. IV.1 need not be imposed on the circumferential mode n . The only requirement on the number of n modes is that they include all those which radiate efficiently, i.e., all n satisfying $n < ka$. Here we have used the $n=0,1$ and 2 modes, of which according to Table IV.2 column 3, only the first is supersonic over 20 Hz $< f < 500$ Hz. However, strong $n=0$ response is not anticipated for the low frequencies considered and all three modes may in some cases contribute comparably to the far-field signal. Acoustical radiation from subsonic and supersonic circumferential modes was also discussed qualitatively in Chapter II, Section A.

D. The Effect of Stiffening Frames on Acoustic Radiation

In the low frequency limit frame structural impedances become inertial and thus vanishingly small. Internal frame-skin reactions are similarly zero as the entire structure moves in its fundamental beam mode. As the frequency increases, frame-shell impedance mismatches grow and so must reaction forces. Frame reactions may be expected to be greater for those frames positioned away from the nodes of an excited m shell mode;

e.g., an $m=1$ resonant mode will generally cause greater reactions for the two frames near the shell middle than for those near the two ends. Conversely, the $m=5, 10, 15 \dots$ resonances should have associated smaller reactions since the four frame positions coincide naturally with modal nodes. Given sufficient structural damping, at higher frequencies frame reactions become acoustic points (or rings) of origin wherever the shell-plating structural far field they excite is below coincidence.

E. Exact Solutions: Numerical Results

E.1 Summary

All far-field predictions presented here use the spherical coordinate system of Figure II.1. The field position defined by $\phi=0$, $\psi=90^\circ$ (beam aspect) is in line with the drive direction; $\phi=180^\circ$, $\psi=90^\circ$ points in the direction opposite the drive. Preliminary spot checks on the shape of the acoustic directivity revealed that for most frequencies in the range investigated pressure maxima occurred within elevation angles $\psi=65^\circ$ and 85° , typically in the vicinity of $\psi=80^\circ$. Far-field results are presented at 20° intervals for both circumferential and elevation angles. Since directivity patterns were fairly smooth, the levels shown for $\psi=80^\circ$ are in essence equal to those for $\psi=90^\circ$, which are not shown. The dimensional distance Ra from the cylinder's center to the far-field point is 45 ft; thus, $k \cdot Ra$ varies in value from about 1 at 20 Hz to just over 25 at 500 Hz. The pressure has been normalized by the quantity F/a^2 , where F is the magnitude of the applied drive.

E.2 Exact Solution: Frequency Sweeps

Figure IV.3 shows frequency sweeps at $\psi=80^\circ$, $\phi=0$ and at $\psi=80^\circ$, $\phi=180^\circ$ for the drive on the shell. Figure IV.4 shows similar results for the drive on the frame. The acoustic field for the drive acting directly on the fluid is given in both by the force-dipole curve. The latter far field is antisymmetric with respect to the $\phi=90^\circ$ plane and its levels for $\phi=0$ and 180° are identical. In Figure IV.3 the spectrum for $\phi=0$ generally

stays above the dipole curve, while that for $\phi=180^\circ$ seems to oscillate about it. For lower frequencies the $\phi=0, 180^\circ$ curves merge in agreement with the expectation that the structural response should then be primarily rigid body with an associated dipole-like far field. In the extreme low-frequency range bounded above by the fluid-loaded fundamental, the system's total impedance is stiffness-controlled and some departure from the dipole curve should be expected. This, however, is an artifact of the model since the subject actually was a freely suspended hull.

Figure IV.4 corresponds to the driven-frame case. The relatively small differences between the $\phi=0, 180^\circ$ curves indicate rigid-body motion over most of the spectrum.

E.3 Exact Solution: Directivity Patterns for Drive on Shell

Figures IV.5-8, corresponding to the drive-on-shell case, show predicted directivity patterns for a few of the peaks in Figure IV.3, $\phi=0$ spectrum. Each figure shows three curves corresponding to three different elevation angles; each curve shows far-field pressure vs. circumferential angle ϕ on a plane normal to the cylinder axis. Thus for example, the $\phi=0$ value of the $\psi=80^\circ$ curve on Figure IV.5, roughly -64 dB, corresponds to the local peak at 100 Hz in Figure IV.3. Similarly, the $\phi=180^\circ$ value for $\psi=80^\circ$ corresponds to that for $\phi=180^\circ$ at 100 Hz in Figure IV.3. The low values obtained near $\phi=90^\circ$ (direction perpendicular to the drive at every elevation angle) further confirms the dipole-like behavior of the acoustic field. Since the drive acts at the cylinder's exact center, the directivity patterns of Figures IV. 5-8 are symmetric about the $\psi=90^\circ$ plane; e.g., the pattern for $\psi=100^\circ$ is the same as that for $\psi=80^\circ$, and that for $\psi=140^\circ$ is equal to that for $\psi=40^\circ$.

The gap at 200 Hz between the $\phi=0, 180^\circ$ curves has been attributed to $n=0,2$ contributions comparable in magnitude to that of $n=1$. Figure IV.6 shows the 200 Hz far-field pattern. We note that while the largest pressure

still belongs to the $\psi=80^\circ$ elevation, other elevations may dominate at other ϕ positions.

Figure IV.7 and 8, respectively for 300 and 400 Hz, continue the trend towards increased complexity with increasing frequency, especially for lower elevations.

Figure IV.9 shows the directivity pattern on the plane containing the cylinder axis and the $\phi=0$ point. The circumferential angle is fixed at $\phi=0$ and the elevation angle varies from the position $\psi=0$, which looking to the cylinder sees only the right cap, to $\psi=180^\circ$ which sees only the left cap. Curves are shown for the four peak frequencies displayed in Figures IV.5-8. As previously stated, all curves are symmetric with respect to $\psi=90^\circ$. For each curve, the $\psi=0, 180^\circ$ values denote predicted radiation levels at the two far-field points which coincide with the cylinder axis. These levels increase with frequency (as expected), though apparently not monotonically.

Since the theoretical model allows cap motion only for $n=0$, low levels at $\psi=0, 180^\circ$ for 100 Hz are consistent with the earlier assertion that the structure primarily responds then as a rigid beam; for $n=1$ the caps are assumed rigid, and low but nonzero levels at $\psi=0, 180^\circ$ are due then to diffraction of signals emanating from the shell surface. The higher levels observed for the other curves point indirectly to the greater participation of the breathing mode as frequency increases. Finally, as previously mentioned, the highest absolute levels were predicted near $\psi=80^\circ$ for most frequencies.

E.4 Exact Solution: Directivity Patterns for Drive on Frame

The peaks in the calculated spectrum at $\psi=80^\circ$ shown in Figure IV.4 for the drive-on-frame case correspond approximately to frequencies 100, 200, 350, and 500 Hz. For these, directivity patterns are shown in Figures IV. 10-14. Figures IV. 10-13 show patterns on planes

normal to the cylinder axis; Figure IV. 14 shows patterns on the plane defined by the cylinder axis and the point $\phi=0$. Unlike the drive-on-shell (middle) case, these radiation patterns are not symmetric relative to the $\psi=90^\circ$ plane. Thus, to provide a better overall picture of the acoustic field, the elevations angles displayed have been changed to $\psi=40^\circ$, 80° , and 140° ; 40° and 140° are of course equidistant from the cylinder axis.

For 100 Hz, Figure IV.10 shows characteristic dipole patterns for all three elevations. As before, $\psi=80^\circ$ provides the highest levels. The small differences between the $\psi=40^\circ$ and the 140° curves suggest that for low frequencies the rigid-body structural response is insensitive to the precise axial position of the frame being driven.

In Figure IV.11 for 200 Hz, the departure observed from the dipole pattern is consistent with the gap between the two curves on Figure IV.4 widening at that frequency. The $\psi=80^\circ$ elevation no longer dominates the acoustic field; also, the differences between the 40° and 140° curves appear more pronounced in the lower hemisphere.

In Figure IV.12 for 350 Hz the highest levels return to $\psi=80^\circ$. However, substantial asymmetry is indicated by the curves for the other two elevations.

Figure IV.13 again shows a dipole pattern at all elevations with $\psi=80^\circ$ containing the highest levels.

Figure IV.14 shows the ψ -dependence of the acoustic field for increasing frequency; the 500 Hz curve contains the largest value -- roughly -45 dB at $\psi=100^\circ$; 350 Hz follows with a level of about -51 dB at $\psi=60^\circ$ and so on. The predicted on-axis values are also observed to increase with frequency. Interestingly, these values seem fairly symmetric relative to $\psi=90^\circ$ even if the rest of the field obviously is not; i.e., two far-field observers, one facing the right cap and the other the left, would hear roughly the same -69 dB at 500 Hz, the same -78 dB at 350 Hz, etc.

F. Iterated Solutions: Drive on Shell

F.1 Summary

In Chapter III iteration algorithms were formulated to solve the coupled fluid-structure systems for the frame-stiffened, finite cylindrical shell. It will be recalled that for $n=0$ the resulting pressure and velocity modal vectors are equal in rank, and that for $n \geq 1$ the pressure vector is two entries longer than the velocity vector because cap element motion is then taken to be identically zero. For both $n=0$, $n \geq 1$, the first technique was the standard Jacobi iteration (J) method adapted to coupled systems. As previously discussed, Jacobi iteration uses a single iteration counter and convergence (or divergence) occurs after applying the algorithm a prescribed number of steps. The second form of iteration for both $n=0$ and $n \geq 1$ equation sets is actually a two-counter process which uses an algorithm nested within another. As was pointed out in Chapter III, part of the partitioned subsystems could be solved either exactly or approximately (Eqs. III.C-8b and D-5c). Here we use the exact option so that these two-step algorithms fall in that category of linear-system iterative solution techniques which Ref. 29 terms "semi-exact."

Iterated solutions were attempted here first by the J technique for every n mode of every frequency. Successful convergence was usually observed for the lower frequencies between 20 and 100 Hz. However, as frequency increased, the J method was found to diverge often. For such cases the two-step algorithms were applied with both counter limits set to 3 and convergence to an acceptable solution was always observed. Thus, in the following presentation of iterated results the figure label "iteration counter(s)=3" states that the approximate solution was obtained either in three J steps, or in three steps of the two-step processes; "iteration counter(s)=1" always refers to the solution after a single J step, which, as discussed in Chapter III, is the quasi in-vacuo result obtained by approximating the structural impedance matrix by its diagonal, which is then inverted. The results shown were chosen as representative of the body of data generated.

F.2 Iterated Solution: Frequency Sweeps

Figure IV. 15 shows exact and approximate solutions for the frequency sweep at $\psi=80^\circ$, $\phi=0$ for the drive-on-shell. The exact curve is the same as that on Figure IV.3 with $\phi=0$. Although the first J step yields a poor estimate, an excellent approximation is obtained in three generally nested steps for all frequencies except perhaps 400 and 450 Hz. The directivity patterns will show, however, that such close agreement was not obtained at other orientations in the acoustic field.

Figure IV. 16 shows the frequency sweep at the two far-field positions coinciding with the cylinder axis ($\phi=0, \psi=0$ and $\phi=0, \psi=180^\circ$). Below 200 Hz even the one-step solution appears adequate. The iterated solution using counter(s) set to 3 is again for all practical purposes the exact solution.

F.3 Directivity Patterns: Iterated Solutions

Figure IV. 17 shows exact and approximate directivity patterns on the plane defined by $\psi=80^\circ$ with ϕ varying from 0 to 360° . The exact solution is taken from Figure IV.5 (different scale). We note that the degree of improvement vs number of iterations appears to be global in that convergence is equally good for all values of circumferential angle.

Figure IV. 18 shows pattern and convergence behavior for 300 Hz. The convergence rate for this case appears greater than that for 100 Hz since the zeroth solution is now a worse first estimate.

In Figure IV. 19 for 400 Hz convergence ceases to be globally monotonic. Thus, after three steps the solution for $\phi=180^\circ$ seems to be down about 8 dB and that for $\phi=0$ up 4 dB; this 4 dB overshoot was seen in Figure IV. 15 at 400 Hz. Figure IV. 20 shows the pattern for 500 Hz.

Figures IV. 21-24 show directivity patterns on the plane containing the cylinder and $\phi=0$ axes. For all figures the circumferential angle ϕ has value 0 and the elevation angle ψ varies from 0 to 180° . Convergence was observed to be fairly good over the frequency spectrum investigated by the method.

It should be pointed out that within the frequency range investigated here, i.e., below 500 Hz, several fluid-loaded resonances were measured in Ref. 40, part 2; and that although only far-field predictions have been presented here, the iterative algorithms were observed to converge for all n modes to the correct structural response (and associated near-field surface pressure) within this resonant range.

G. Comparison to Experiment

Figure IV. 25 shows measured beam-aspect ($\psi=90^\circ$, $\phi=0$) levels for the cylindrical structure of which Figure IV.1a, b shows one of five equal segments.⁴⁰ Also shown are predictions by the present model for frequencies up to 500 Hz, and by a simpler infinite-cylinder fluid model for frequencies between 500 and 2500 Hz. The force-dipole solution is also indicated.

As previously pointed out, and as again the figure shows, predictions for the low frequency range hover about the force dipole with more consistent departures taking place as frequency increases. Except for the measured anti-resonance dip at 1 kHz for the drive-on-frame case, predictions and the dipole curve would seem to underestimate the mean of the data by about 25 dB.

However, the results of previous experimental and theoretical studies^{41,42} strongly suggest that beam-aspect acoustic spectra of force-driven cylindrical structures similar to that investigated here are closely approximated by the force dipole at the lower frequencies, and, at higher frequencies below coincidence, by the infinite plate solution known classically to be 6 dB above the force dipole. Junger⁴² for example, has identified three primary frequency ranges for a typical heavy-framed submarine hull. In the lower of these the ship behaves as a rigid beam and the force-dipole solution is roughly valid. For the next higher, compartment-resonance, range he has established structural damping criteria under which bounding frames play a subdominant role in the response function which then corresponds to the infinite-plate solution; although at fluid-loaded resonances peak levels may otherwise far exceed those by analytic

asymptotic formulae, he finds that the latter nevertheless provide good mean-value curves. Finally, above the hull's ring resonance he determines that if the shell plating is treated as an infinite system, its acoustic field closely approximates the frequency-averaged measured data.

Therefore, the discrepancy in overall behavior between present and earlier measurements plus theoretical conclusions remains to be explained.

H. Computational Times for Exact vs Iterated Solutions

We end the discussion here with a brief summary of the time-savings advantage of approximate solutions. In all fairness, however, it should be pointed out that for the present modal formulation total computational costs were dominated by the generation of matrix elements for the fluid system rather than by the solution technique applied to effect its inversion. In effect, the A constant in Eq. III.E-1a had a large value as a result of the integration routines used here. Nevertheless, if for the moment the AN^2 system-generation contribution is ignored in Eq. III.E-1a, one may calculate part of the $N \rightarrow \infty$ asymptotic value of the savings ratio between iterated and exact solution, i.e., the $(B/C) \cdot 1/N$ part of Eq. III.B-1b ($N=M+2$ here). This measure of savings is quantified next.

Table IV.3 shows computational times needed to solve a given, generated coupled system. Percent time savings over the exact solution are tabulated. The first of the approximate solution entries, $K_1=1, K_2=1$, refers to the J method with K_1 and K_2 as defined in Chapter III. The second entry, $K_1=K_2=3$, refers to the nested, two-step iteration process, for which a set of K_1, K_2 combinations were also applied yielding solutions of accuracy ranging from the generally acceptable ($K_1=K_2=3$), to the generally unacceptable ($K_1=K_2=1$).

Had a technique such as DAA been used to model the fluid in the present problem, the ratio of total matrix inversion to matrix generation

costs would have been essentially given by $(B/C)1/N$. The reason for this of course is that DAA requires a single fluid calculation valid for all frequencies and thus eliminates much of the system-generation effort. However, the final solution would then be doubly approximate because the approximate inversion process would then operate on an approximate fluid model.

Finally, as discussed in Chapter III, SOR-type recasting of fluid and structural systems should be expected to improve convergence rates without significant computational penalties. Comparison of exact and iterated solutions should appear then even more in favor of the approximate method.

V. SUMMARY AND CONCLUSIONS

A theoretical model has been developed to predict acoustic radiation from a submerged, finite-cylindrical shell internally stiffened by ring frames and with flat, movable end caps. The model has been applied to a structure for which recent acoustic data has been collected. Predictions differ from existing measurements by roughly 25 dB; however, they appear consistent with the results of a number of previous experimental and theoretical studies.

Iterative schemes have been developed to solve the associated fluid-structure coupled systems over a moderate range of frequencies encompassing several fluid-loaded resonances. We have demonstrated that such techniques may be applied to generate essentially the exact solution in a reasonably small number of iterations. By comparing computational costs to those for the exact result, we found iteration to be economically advantageous for all frequencies considered.

Lastly, we have noted that, for an arbitrary fluid-loaded structure modeled using finite differences or elements, the ratio of total computing cost by iteration to that using exact inversion should decrease with system size. The development and implementation of techniques such as those used here is therefore recommended.

APPENDIX II.A

$$(1) \quad a^2 I_{2n} = \frac{2(-1)^n}{\{1+r^2+(z-\bar{z})^2\}^{3/2}}$$

$$\int_0^\pi \frac{d \cos \alpha (1+r \cos \alpha) [1-ika \sqrt{1+r^2+(z-\bar{z})^2} \sqrt{1+\xi_1 \cos \alpha}] \exp\{ika \sqrt{1+r^2+(z-\bar{z})^2} \sqrt{1+\xi_1 \cos \alpha}\}}{\{1+\xi_1 \cos \alpha\}^{3/2}}$$

where

$$\xi_1 = 2r/[1+r^2+(z-\bar{z})^2]$$

$$a I_{3n} = \frac{2(-1)^n}{\sqrt{r^2+\bar{r}^2+(z+L/2a)^2}} \int_0^\pi \frac{d \cos \alpha \exp\{ika \sqrt{r^2+\bar{r}^2+(z+L/2a)^2} \sqrt{1+\xi_2 \cos \alpha}\}}{\sqrt{1+\xi_2 \cos \alpha}}$$

$$a^3 I_{4n} = \frac{2(-1)^n}{\{r^2+\bar{r}^2+(z+L/2a)^2\}^{3/2}}$$

$$\int_0^\pi \frac{d \cos \alpha [1-ika \sqrt{r^2+\bar{r}^2+(z+L/2a)^2} \sqrt{1+\xi_2 \cos \alpha}] \exp\{ika \sqrt{r^2+\bar{r}^2+(z+L/2a)^2} \sqrt{1+\xi_2 \cos \alpha}\}}{\{1+\xi_2 \cos \alpha\}^{3/2}}$$

where

$$\xi_2 = 2r\bar{r}/[r^2+\bar{r}^2+(z+L/2a)^2]$$

$$a I_{5n} = \frac{2(-1)^n}{\sqrt{r^2+\bar{r}^2+(z-L/2a)^2}} \int_0^\pi \frac{d \cos \alpha \exp\{ika \sqrt{r^2+\bar{r}^2+(z-L/2a)^2} \sqrt{1+\xi_3 \cos \alpha}\}}{\sqrt{1+\xi_3 \cos \alpha}}$$

PLANE NORMAL TO SHELL AXIS DRIVE ON SHELL, F=300 HZ

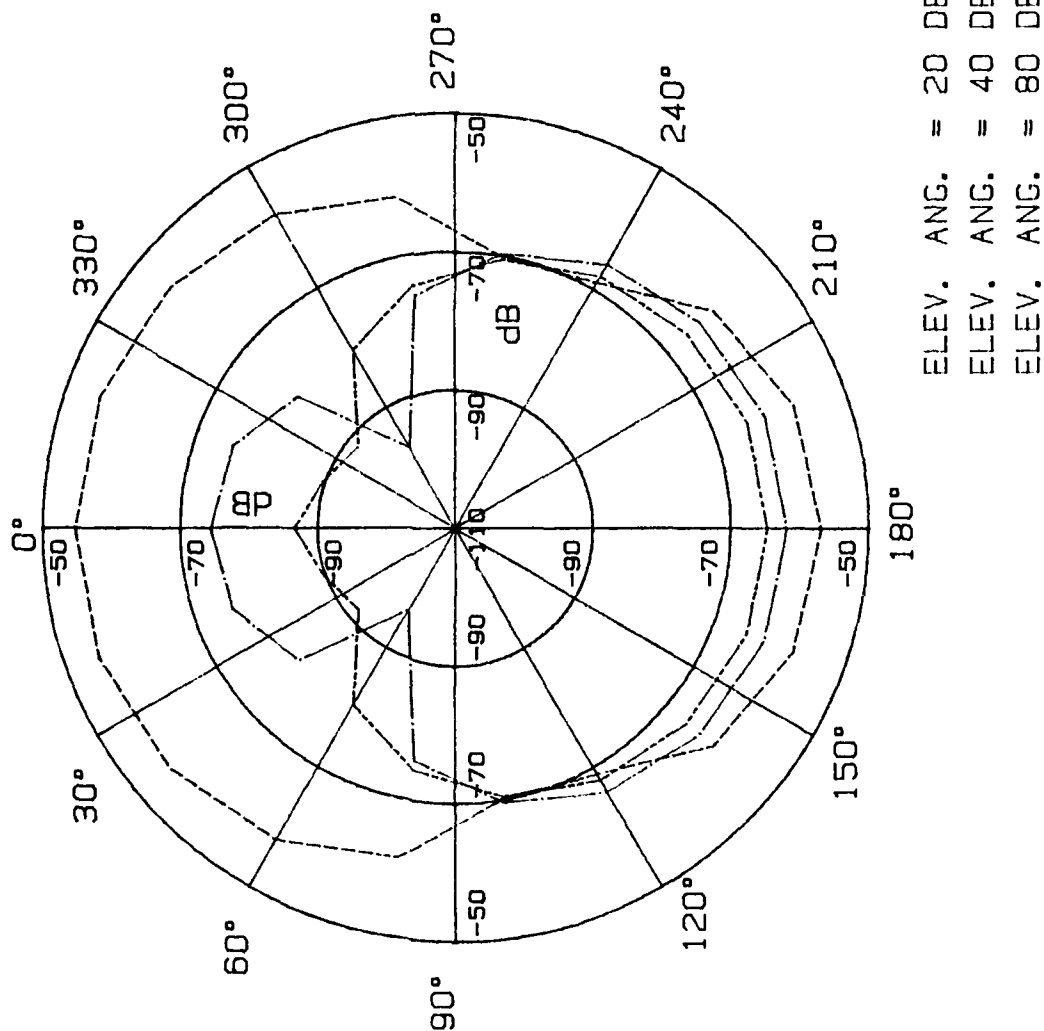


Figure IV.7 Predicted Acoustic Directivity vs ϕ for 300 Hz with Point Drive on Shell Middle;
 $\psi = 20^\circ, 40^\circ, 80^\circ$.

PLANE NORMAL TO SHELL AXIS DRIVE ON SHELL, F=200 Hz

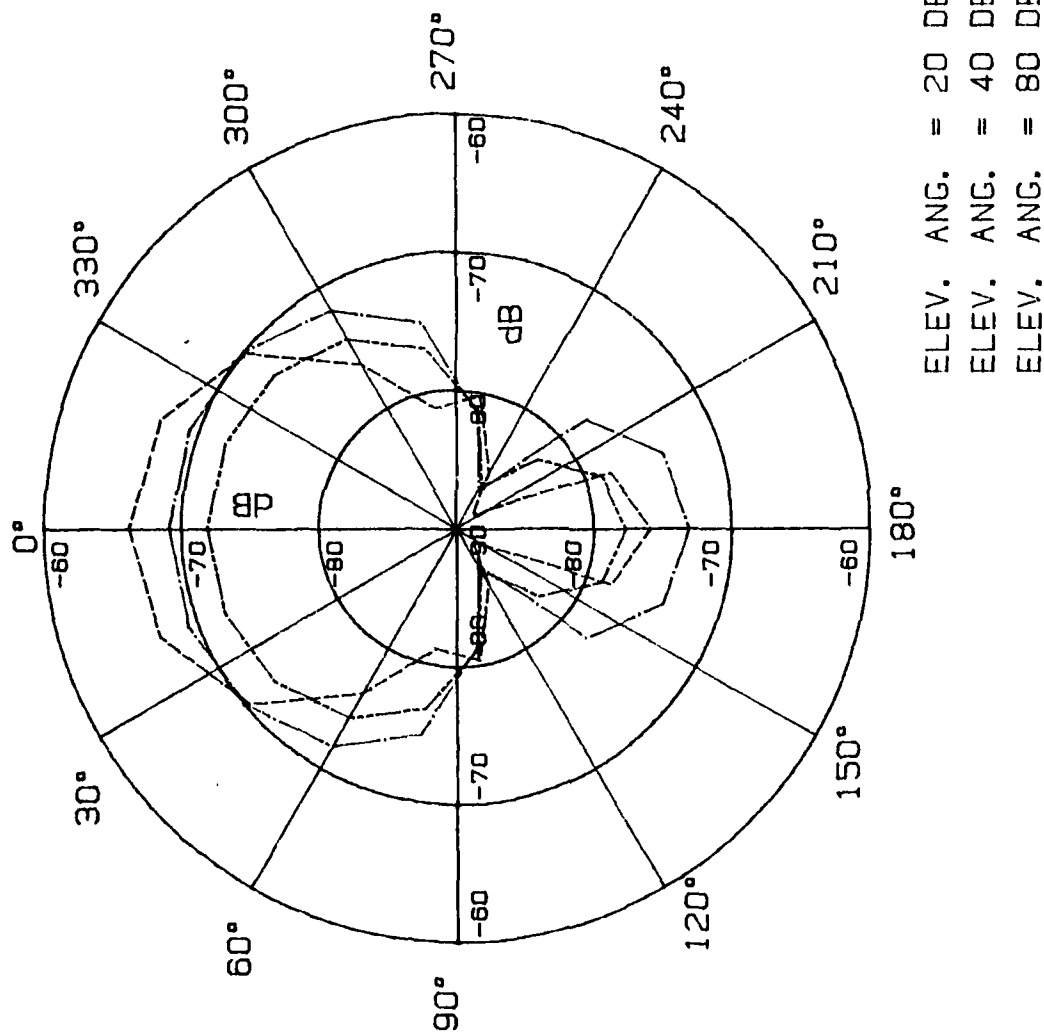


Figure IV.6 Predicted Acoustic Directivity vs ϕ for 200 Hz with Point Drive on Shell Middle;
 $\psi=20^\circ, 40^\circ, 80^\circ$.

PREDICTED ACOUSTIC DIRECTIVITY IN
 PLANE NORMAL TO SHELL AXIS
 DRIVE ON SHELL, $F=100$ Hz

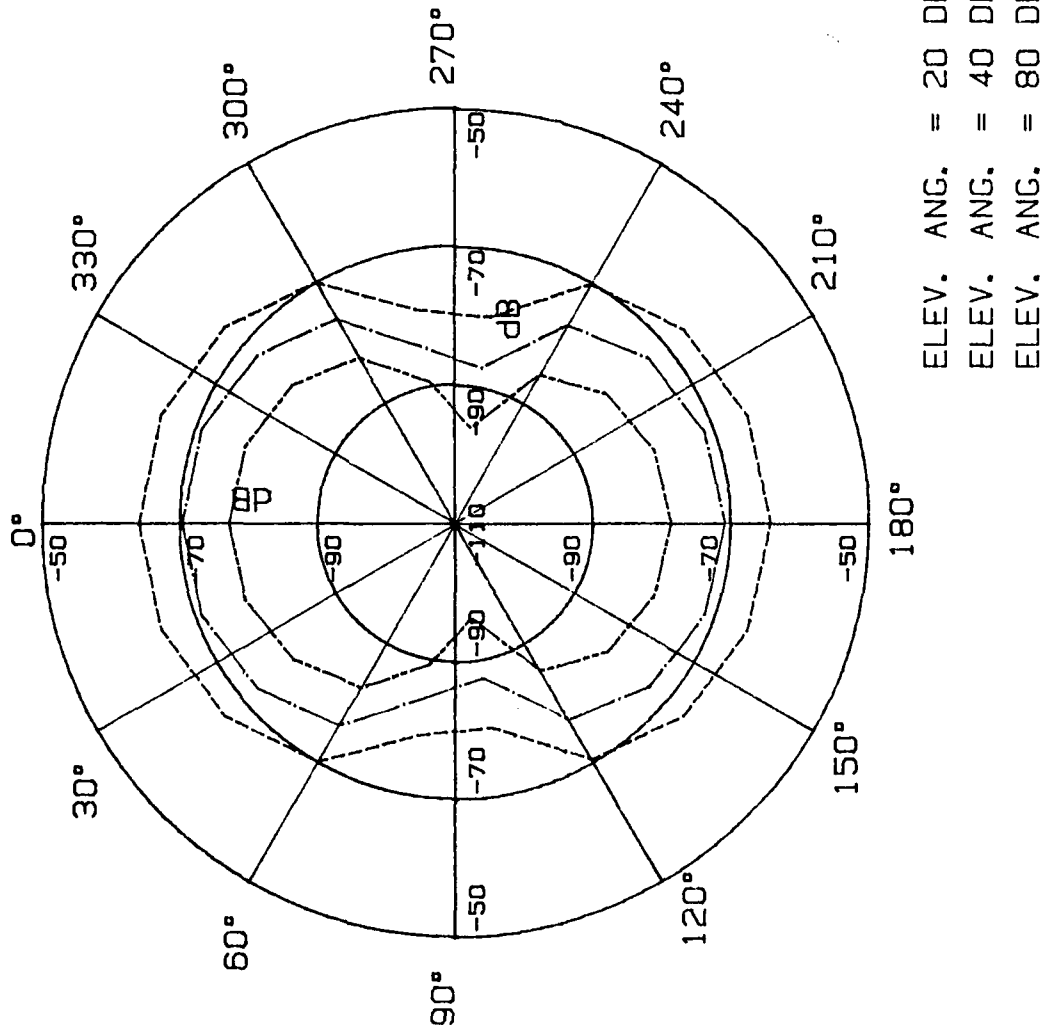


Figure IV.5 Predicted Acoustic Directivity vs ϕ for 100 Hz with Point Drive on Shell Middle;
 $\psi=20^\circ, 40^\circ, 80^\circ$.

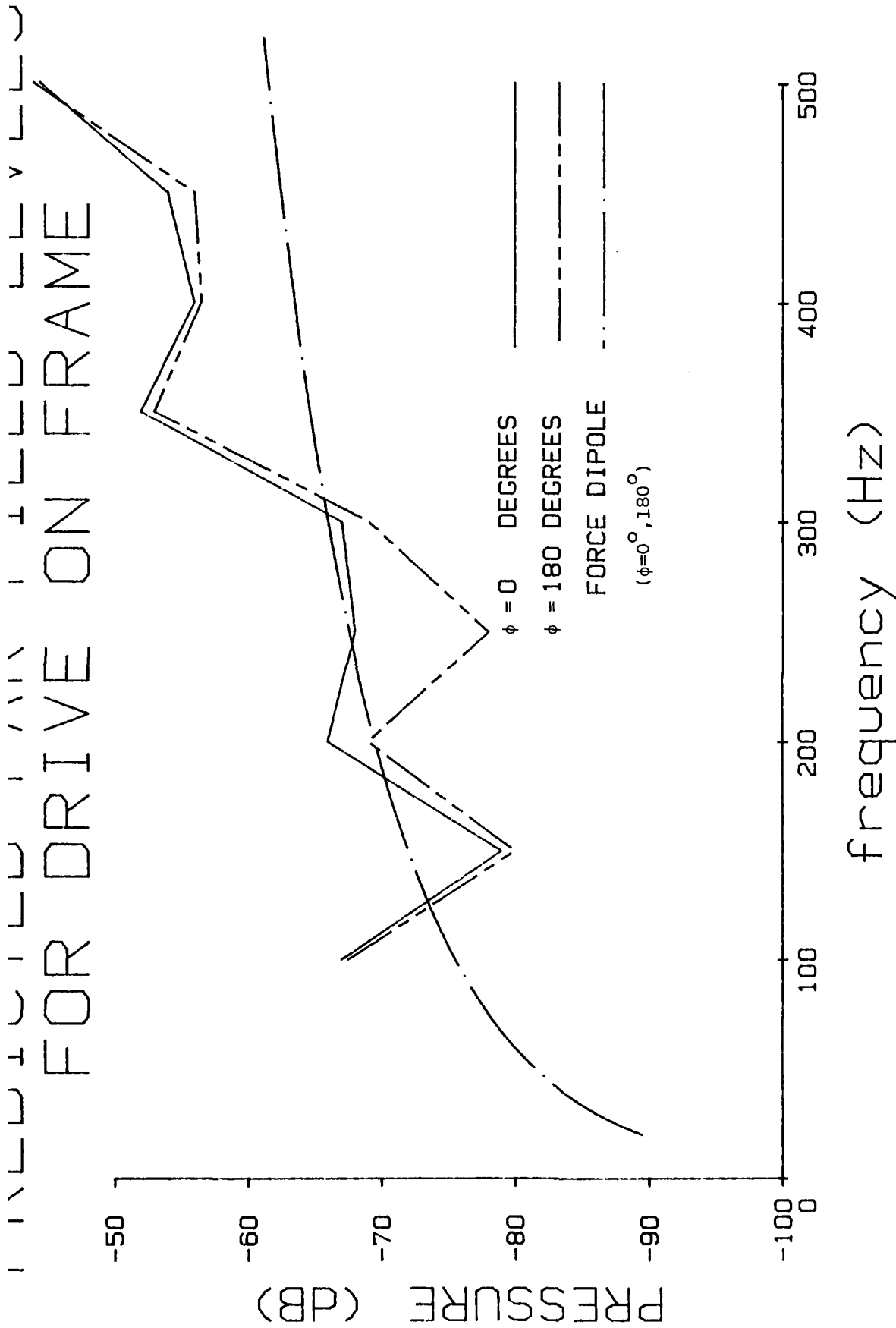


Figure IV.4 Calculated Spectra of Radiated Sound at ($\phi=0, \psi=80^\circ$), ($\phi=180^\circ, \psi=80^\circ$) for Drive on Frame.

PREDICTED FAR-FIELD LEVELS FOR DIRECT SHELL DRIVE

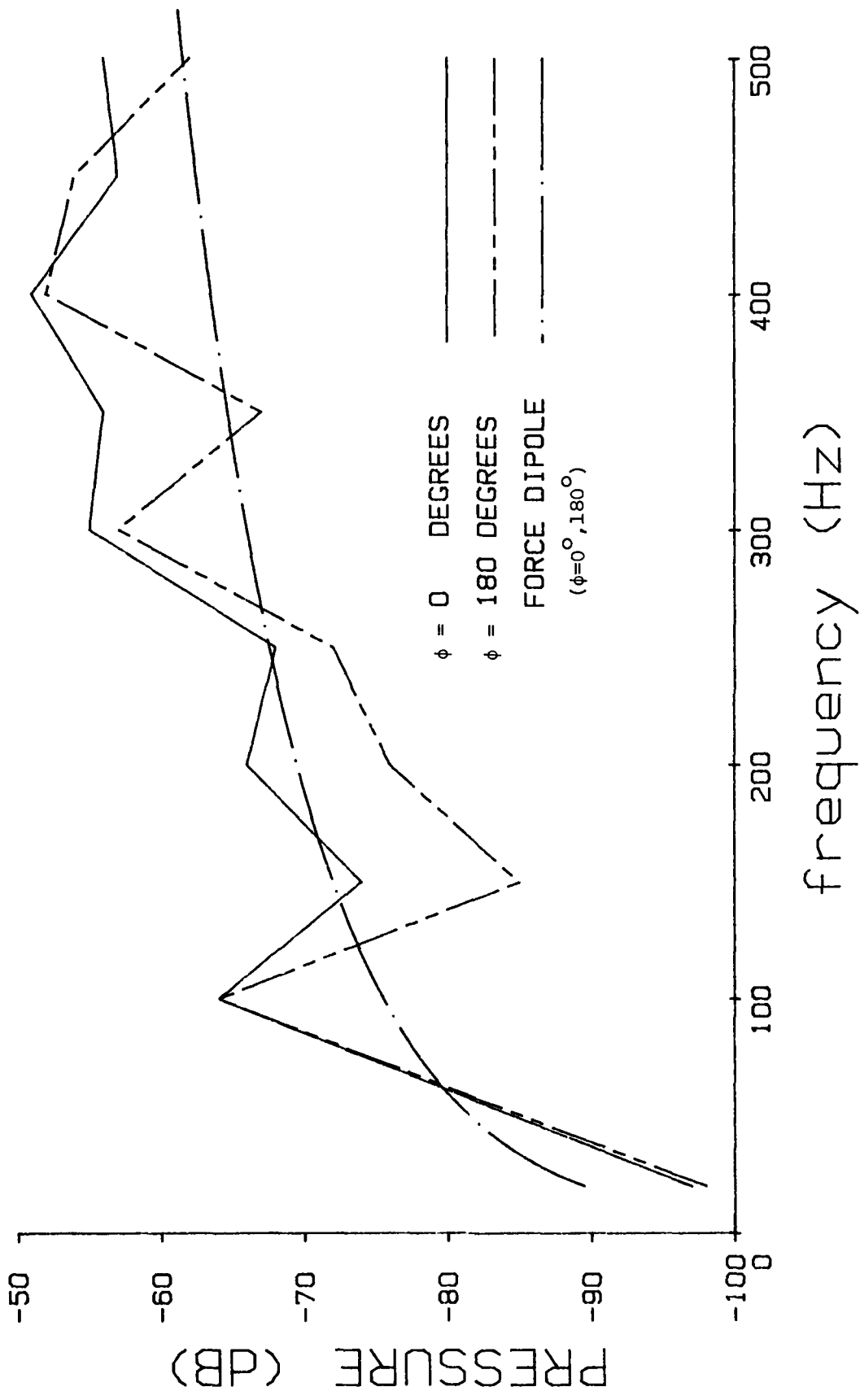


Figure IV.3 Calculated Spectra of Radiated Sound at ($\phi=0, \psi=80^\circ$), ($\phi=180^\circ, \psi=80^\circ$) for Drive on Shell.

TABLE IV.2
STRUCTURAL AND ACOUSTIC WAVENUMBERS, AND REQUIRED SYSTEM SIZE

f (Hz)	$k_f a (\approx .188\sqrt{f})$	$M(>\frac{L/a}{\pi} \cdot k_f a)$	$ka (\approx f/1000)$
20	.84	6	.02
50	1.32	9.3	.05
100	1.88	13.2	.1
200	2.66	18.6	.2
500	4.20	29.4	.5
1000	5.95	41.6	1.
2000	8.41	59.0	2.
5000	13.30	93.0	5.

TABLE IV.1
CYLINDER STRUCTURAL PARAMETERS

Cylinder length	230"
Shell thickness	.3125" (Aluminum)
Shell radius	10.344"
Caps' thickness	1.5" (Steel)
No. of frames	4 (Aluminum)
Inter-frame spacing	46"
Frame height	1.0625"
Frame width	3.25"
Assumed Loss factor for all structures	.05

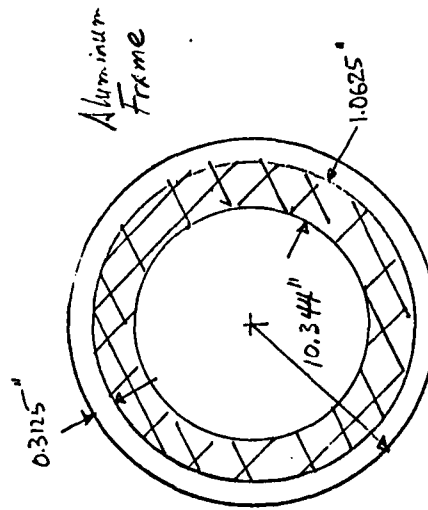
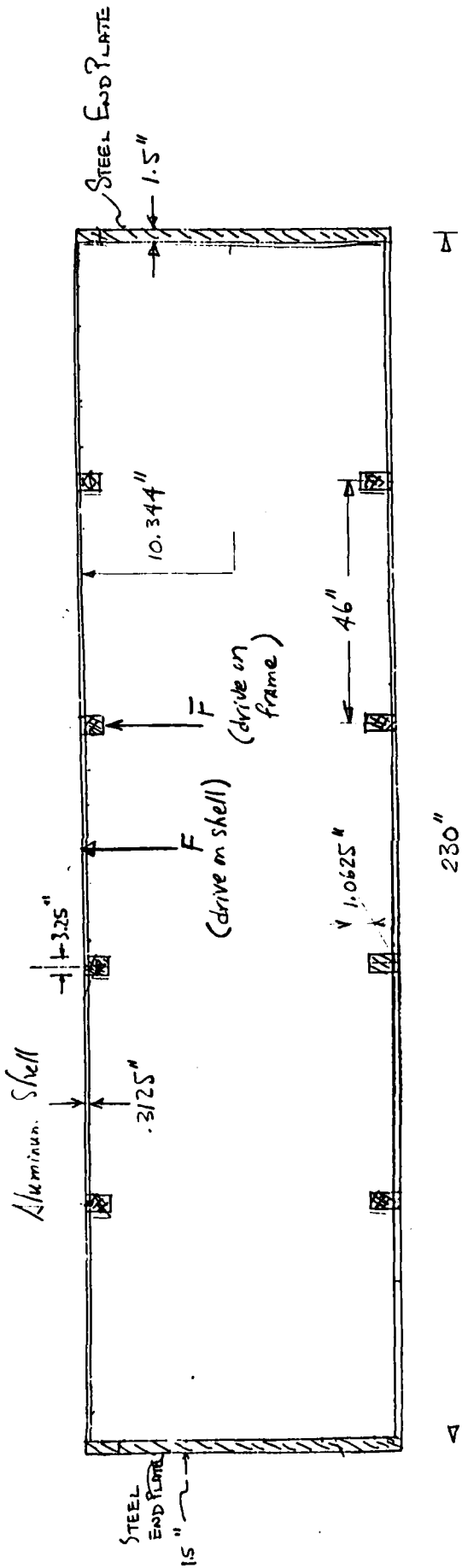
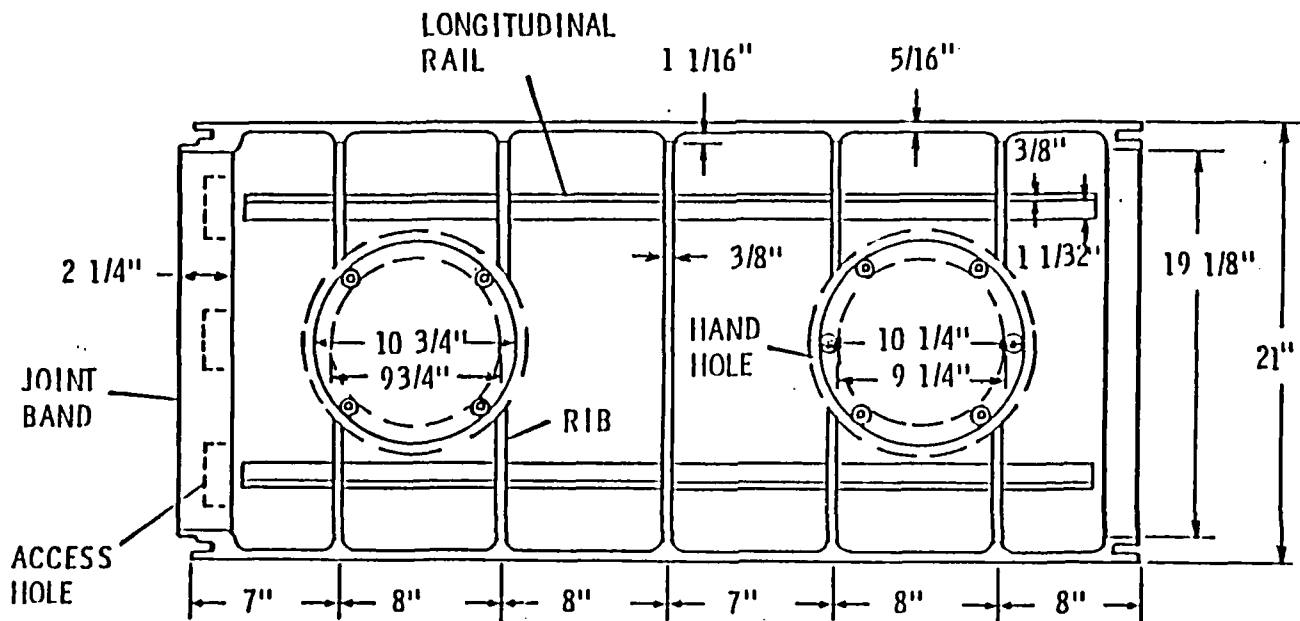


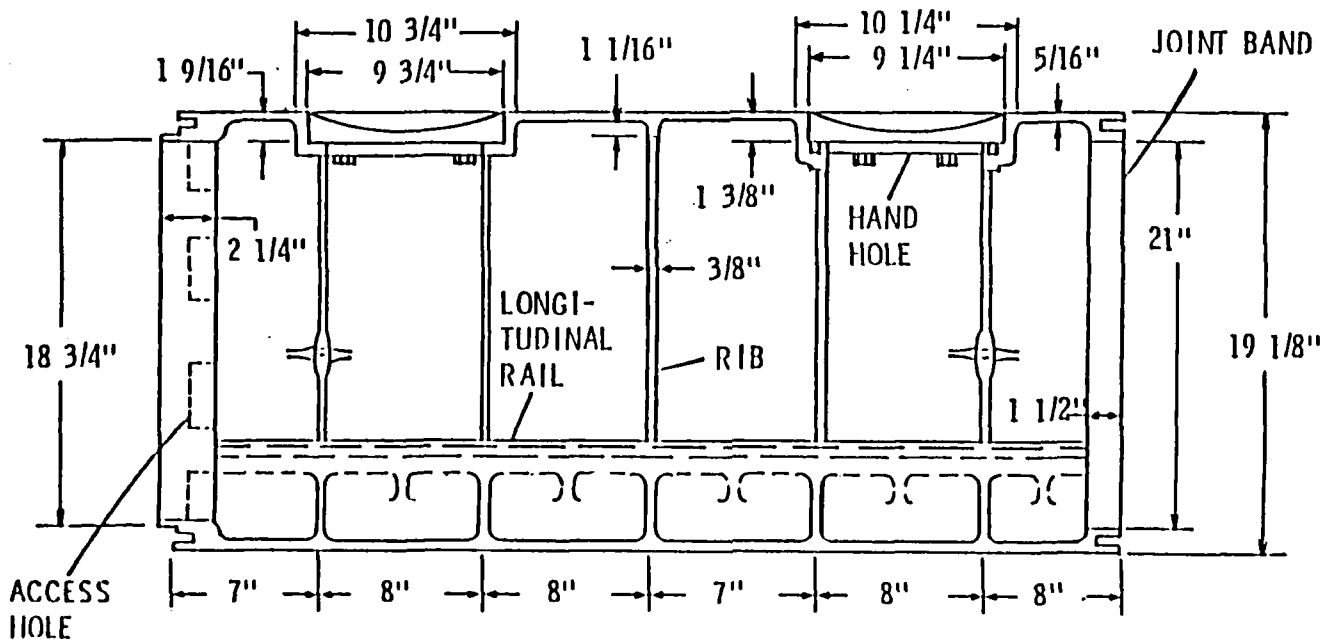
Figure IV.2 Idealized Geometry Used for Theoretical Predictions, Structural Parameters are Indicated for Shell, Caps, and Frames (also Table IV.1) Drives considered here are shown: on shell, on frame.

TOP VIEW



(a)

SIDE VIEW



(b)

Figure IV.1a,b From Ref. 40; Top and Side Views of a Typical ΔL Interframe Cylinder Section of the Experimental Model ($\Delta L=46"$ in Fig. IV.2)

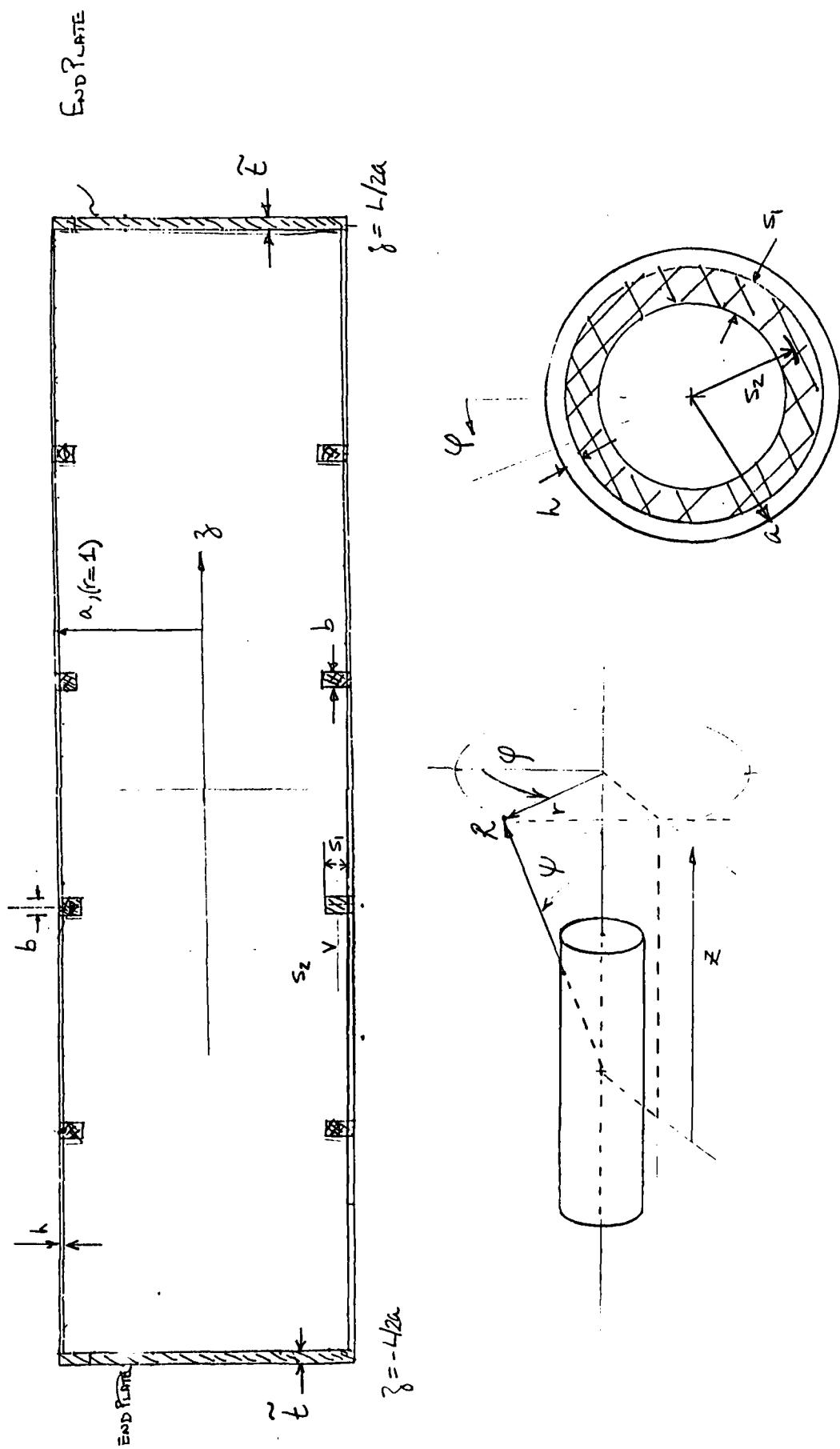


Figure II.1 Finite Cylinder Model Showing (a) Side View with (r, z) Origin and Structural Dimensions for Shell, Caps, and Frames; (b) Coordinate System for Far-field Calculations; (c) Cylinder Cross-section Showing Structural Ring-frame Parameters.

where "det" denotes the determinant of the matrix in Eq. II.B-4.

(2) Modal Impedances for Ring Frames

Modal impedances \tilde{Z}_{n11} , etc., have been given Harari²⁸ in dimensional form and relate net frame forces to frame displacements rather than velocities. The relationship between Harari's "impedance" Z_{n11}^H and our normalized quantity Z_{n11} is

$$Z_{n11} = \frac{i}{ka} \frac{Z_{n11}^H}{\rho c^2}$$

and similarly for the rest. Thus they are given by

$$Z_{n11} = \frac{i(\rho_f/\rho)(c_{pf}/c)\sqrt{1-i\eta_f}}{\Omega_f} b s_1 \left\{ \frac{n^4 s_1^2}{12 s_2^2} - \frac{n^2 s_1}{2 s_2} + \frac{1}{s_2} - s_2 \Omega_f^2 \right. \\ \left. - \frac{n s_1 s_2}{2} \left[- \frac{n^3 s_1}{s_2^2} \left(\frac{1}{2} - \frac{s_1}{12 s_2} \right) + \frac{n}{s_2^2} + \frac{n s_1}{2} \Omega_f^2 \right] \right\}$$

$$Z_{n33} = \frac{i(\rho_f/\rho)(c_{pf}/c)\sqrt{1-i\eta_f}}{\Omega_f} b s_1 s_2 \left\{ n^2 \left(1 + \frac{n^2 s_1^2}{s_2^2} \right) - (s_2 \Omega_f)^2 \right\}$$

$$Z_{n13} = \frac{i(\rho_f/\rho)(c_{pf}/c)\sqrt{1-i\eta_f}}{\Omega_f} b s_1 n \left[1 + \left(\frac{n s_1}{s_2} \right)^2 \right] - \frac{n s_1}{2 s_2} Z_{n33}$$

$$Z_{n31} = \frac{i(\rho_f/\rho)(c_{pf}/c)\sqrt{1-i\eta_f}}{\Omega_f} b s_1 n \left[1 - n^2 s_1 \left(\frac{1}{2} - \frac{s_1}{12 s_2} \right) + \frac{s_1}{2} (s_2 \Omega_f)^2 \right]$$

where b is the frame width as defined in Fig. II.2, which also shows $s_1, s_2; \rho_f$ is the frame material density, c_{pf} its compressional wave speed, and η_f its structural loss factor; also,

$$\Omega_f = (\omega a / c_{pf}) / \sqrt{1-i\eta_f}$$

In the above equations all spatial quantities appear normalized by the shell radius a .

$$A_2 = \left(\frac{1+\nu}{2}\right) n \left(\frac{m\pi a}{L}\right)$$

$$A_3 = \nu \left(\frac{m\pi a}{L}\right)$$

$$A_4 = A_2$$

$$A_5 = \Omega^2 - (1+\beta^2) \{n^2 + \left(\frac{1-\nu}{2}\right) \left(\frac{m\pi a}{L}\right)^2\}$$

$$A_6 = -n[1+\beta^2 \{n^2 + \left(\frac{m\pi a}{L}\right)^2\}]$$

$$A_7 = A_3$$

$$A_8 = A_6$$

$$A_9 = \Omega^2 - 1 - \beta^2 \left[\left(\frac{m\pi a}{L}\right)^2 + n^2 \right]^2$$

where

$$\Omega = (\omega a / c_p) / \sqrt{1 - i\eta} \quad ;$$

c_p = shell compressional wave speed;

η = structural loss factor; and

$$\beta = (h/a) / \sqrt{12} \quad .$$

The constants B_1 , B_3 , B_7 , B_9 are given by

$$B_1 = \frac{A_5 A_9 - A_6 A_8}{\det}$$

$$B_3 = \frac{A_2 A_6 - A_3 A_5}{\det}$$

$$B_7 = \frac{A_4 A_8 - A_5 A_7}{\det}$$

$$B_9 = \frac{A_1 A_5 - A_2 A_4}{\det}$$

APPENDIX II.B

(1) Structural Operators and Constants

The thin-shell theory operators L_1, \dots, L_9 in Eqs. II.B-1a are given by (Refs. 34, and 12).

$$L_1 = \frac{\partial^2}{\partial z^2} + \frac{1-\nu}{2} \frac{\partial^2}{\partial \phi^2} + \Omega^2$$

$$L_2 = \frac{1+\nu}{2} \frac{\partial^2}{\partial z \partial \phi}$$

$$L_3 = \frac{\nu \partial}{\partial z}$$

$$L_4 = L_2$$

$$L_5 = \left(\frac{1-\nu}{2}\right)(1+\beta^2) \frac{\partial^2}{\partial z^2} + (1+\beta^2) \frac{\partial^2}{\partial \phi^2} + \Omega^2$$

$$L_6 = \frac{\partial}{\partial \phi} - \beta^2 \left(\frac{\partial^3}{\partial z^2 \partial \phi} + \frac{\partial^3}{\partial \phi^3} \right)$$

$$L_7 = -L_3$$

$$L_8 = -L_6$$

$$L_9 = -1-\beta^2 \left(\frac{\partial^4}{\partial z^4} + \frac{2\partial^4}{\partial z^2 \partial \phi^2} + \frac{\partial^4}{\partial \phi^4} \right) + \Omega^2$$

The constants A_1, \dots, A_9 in Eq. II.B-4 are,

$$A_1 = \Omega^2 - \left(\frac{m\pi a}{L}\right)^2 - \left(\frac{1-\nu}{2}\right)n^2$$

$$a^3 I_{6n} = \frac{2(-1)^n}{\{r^2 + \bar{r}^2 + (z-L/2a)^2\}^{3/2}}$$

$$\int_0^\pi d\alpha \cos \alpha [1 - ika \sqrt{r^2 + \bar{r}^2 + (z-L/2a)^2} \sqrt{1 + \xi_3 \cos \alpha}] \exp \{ika \sqrt{r^2 + \bar{r}^2 + (z-L/2a)^2} \sqrt{1 + \xi_3 \cos \alpha}\} \\ \frac{1}{\{1 + \xi_3 \cos \alpha\}^{3/2}}$$

$$\xi_3 = 2r\bar{r}/[r^2 + \bar{r}^2 + (z-L/2a)^2]$$

$$(2) \quad C_{nm}^{(2)} = \frac{1}{2\pi} \int_{-L/2a}^{L/2a} dz \sin \frac{m\pi a}{L} (z+L/2a) \cdot (z+L/2a) \int_0^1 d\bar{r} \bar{r} [a^3 I_{4n}(\xi_2; r=1)]$$

$$\tilde{C}_{nm}^{(2)} = \frac{1}{2\pi} \int_0^1 dr r \int_{-L/2a}^{L/2a} d\bar{z} \sin \frac{m\pi a}{L} (\bar{z}+L/2a) [a^2 I_{2n}(\xi_1; r=1)]$$

$$\tilde{C}_n^{(3)} = \frac{L/a}{2\pi} \int_0^1 dr r \int_0^1 d\bar{r} \bar{r} [a^3 I_{6n}(\xi_3; z=-L/2a)]$$

$$\tilde{D}_n^{(3)} = -\frac{ika}{2\pi} \int_0^1 dr r \int_0^1 d\bar{r} \bar{r} [a I_{3n}(\xi_2; z=-L/2a)]$$

$$\tilde{D}_n^{(4)} = -\frac{ika}{2\pi} \int_0^1 dr r \int_0^1 d\bar{r} \bar{r} [a I_{3n}(\xi_2; z=+L/2a)]$$

FAR-FIELD DIRECTIVITY ON
PLANE NORMAL TO SHELL AXIS
DRIVE ON SHELL, $F=400$ HZ

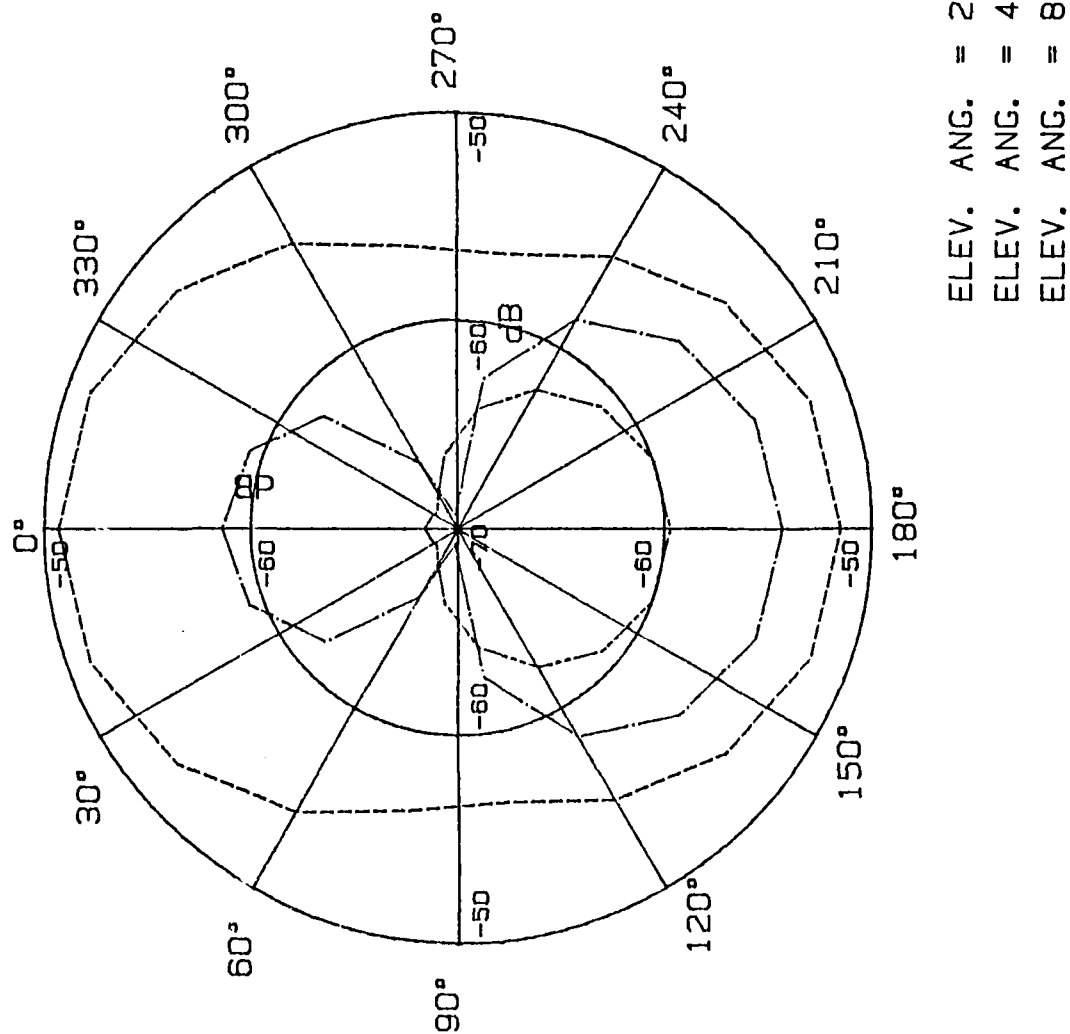


Figure IV.8 Predicted Acoustic Directivity vs ϕ for 400 Hz with Point Drive on Shell Middle; $\psi=20^\circ, 40^\circ, 80^\circ$.

FAR-FIELD DIRECTIVITY ON
 PLANE PASSING THRU SHELL AXIS
 DRIVE ON SHELL, CIRC. ANG. = 0

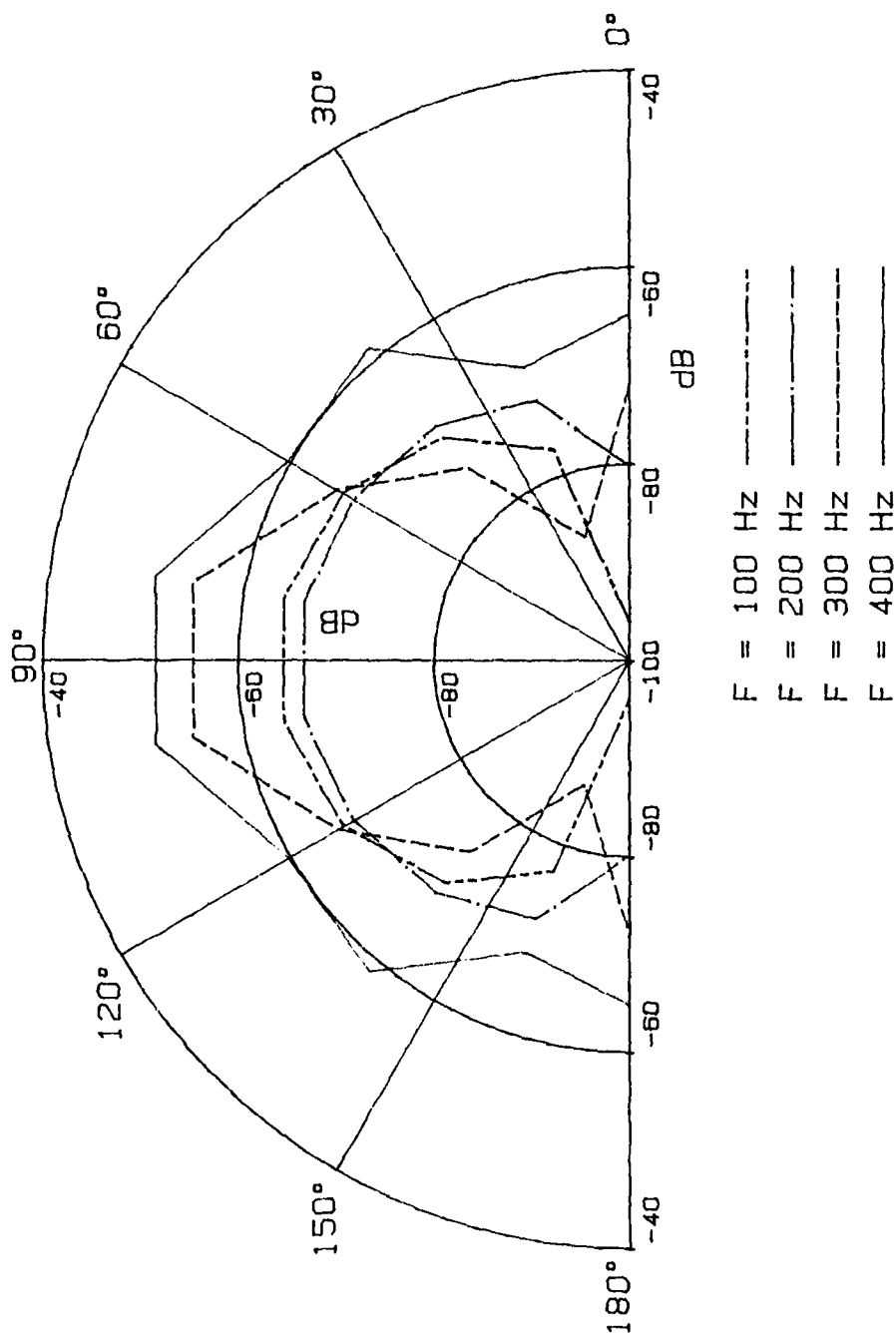
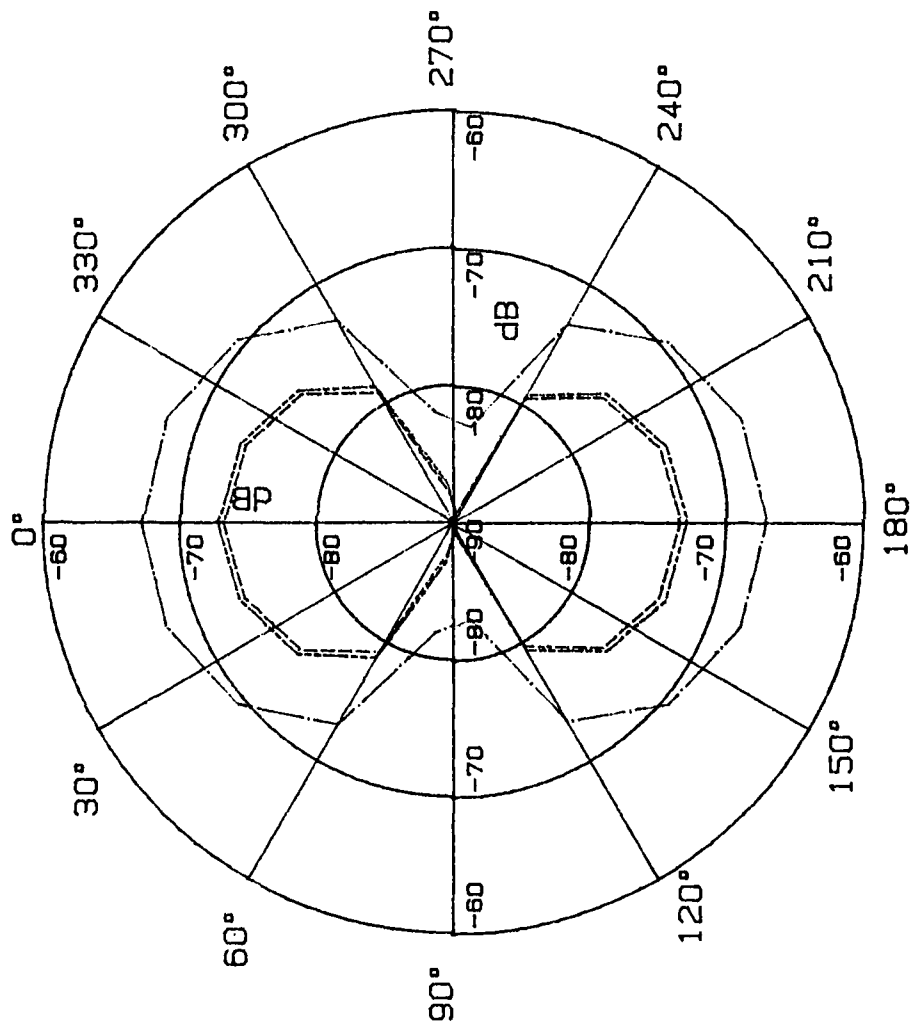


Figure IV. 9 Predicted Acoustic Directivity vs ψ for $\phi=0$; Point Drive on Shell Middle.

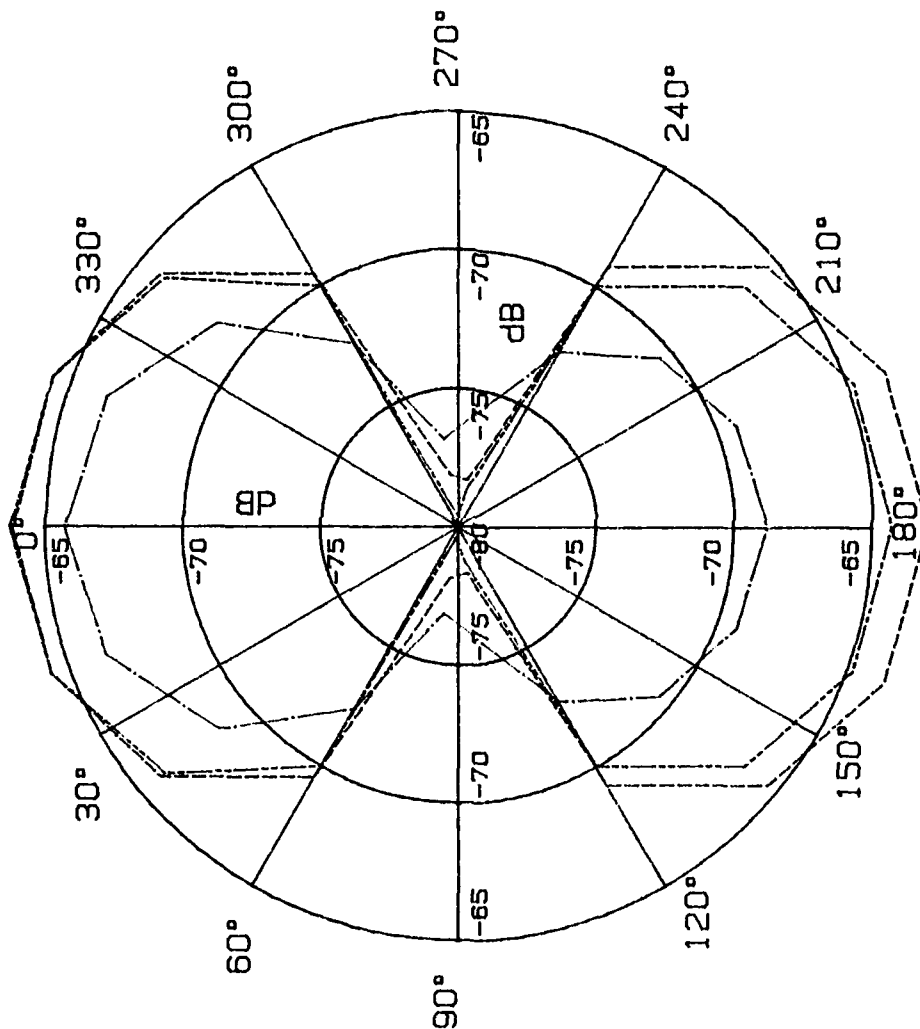
FAR-FIELD DIRECTIVITY ON
PLANE NORMAL TO SHELL AXIS
DRIVE ON FRAME, F=100 Hz



ELEV. ANG. = 40 DEG -----
ELEV. ANG. = 80 DEG -----
ELEV. ANG. = 140 DEG -.-.-.-

Figure IV. 10 Predicted Acoustic Directivity vs ϕ for 100 Hz with Point Drive on Near-middle Frame; $\psi=40^\circ, 80^\circ, 140^\circ$.

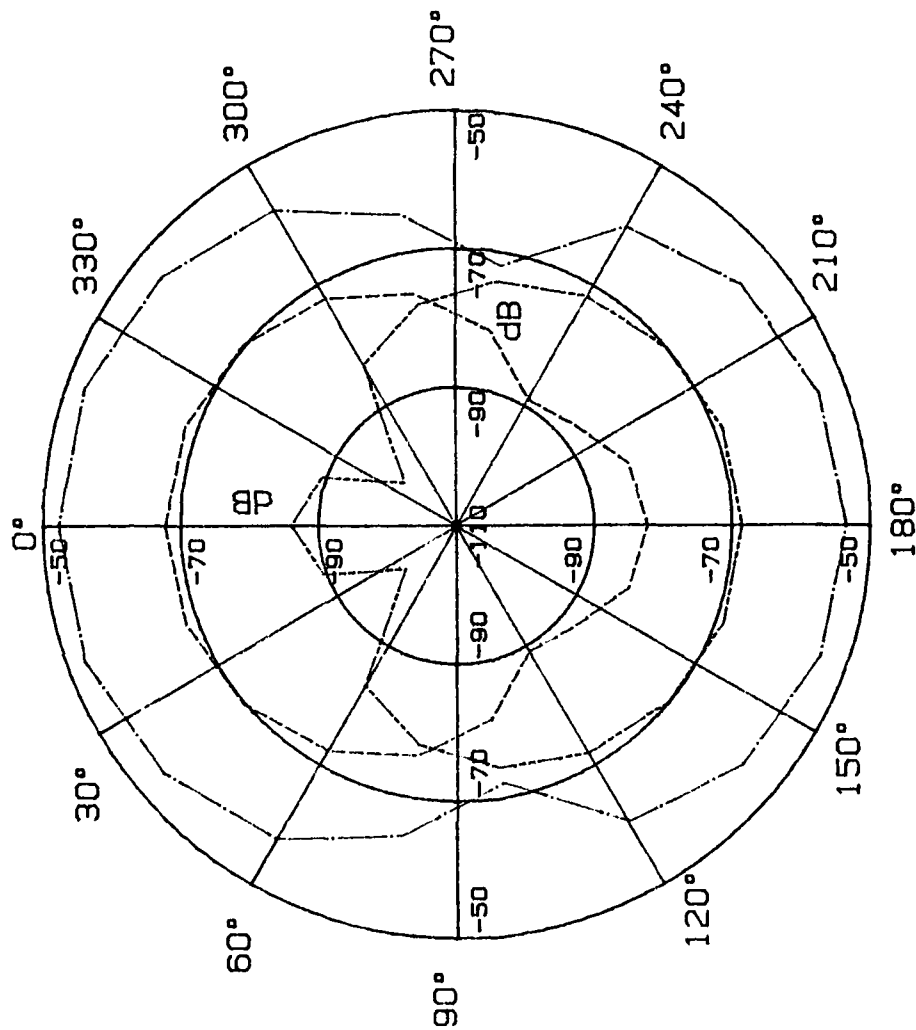
FAR-FIELD DIRECTIVITY ON PLANE NORMAL TO SHELL AXIS DRIVE ON FRAME, F=200 HZ



ELEV. ANG. = 40 DEG ———
 ELEV. ANG. = 80 DEG - - -
 ELEV. ANG. = 140 DEG - . -

Figure IV.11 Predicted Acoustic Directivity vs ϕ for 200 Hz with Point Drive on Near-middle Frame; $\psi=40^\circ, 80^\circ, 140^\circ$.

FAR-FIELD DIRECTIVITY ON PLANE NORMAL TO SHELL AXIS DRIVE ON FRAME, $F=350$ HZ



ELEV. ANG. = 40 DEG -----
 ELEV. ANG. = 80 DEG -----
 ELEV. ANG. = 140 DEG -----

Figure IV.12 Predicted Acoustic Directivity vs ϕ for 350 Hz with Point Drive on Near-middle Frame; $\psi=40^\circ, 80^\circ, 140^\circ$.

FAR-FIELD DIRECTIVITY ON PLANE NORMAL TO SHELL AXIS DRIVE ON FRAME, F=500 HZ

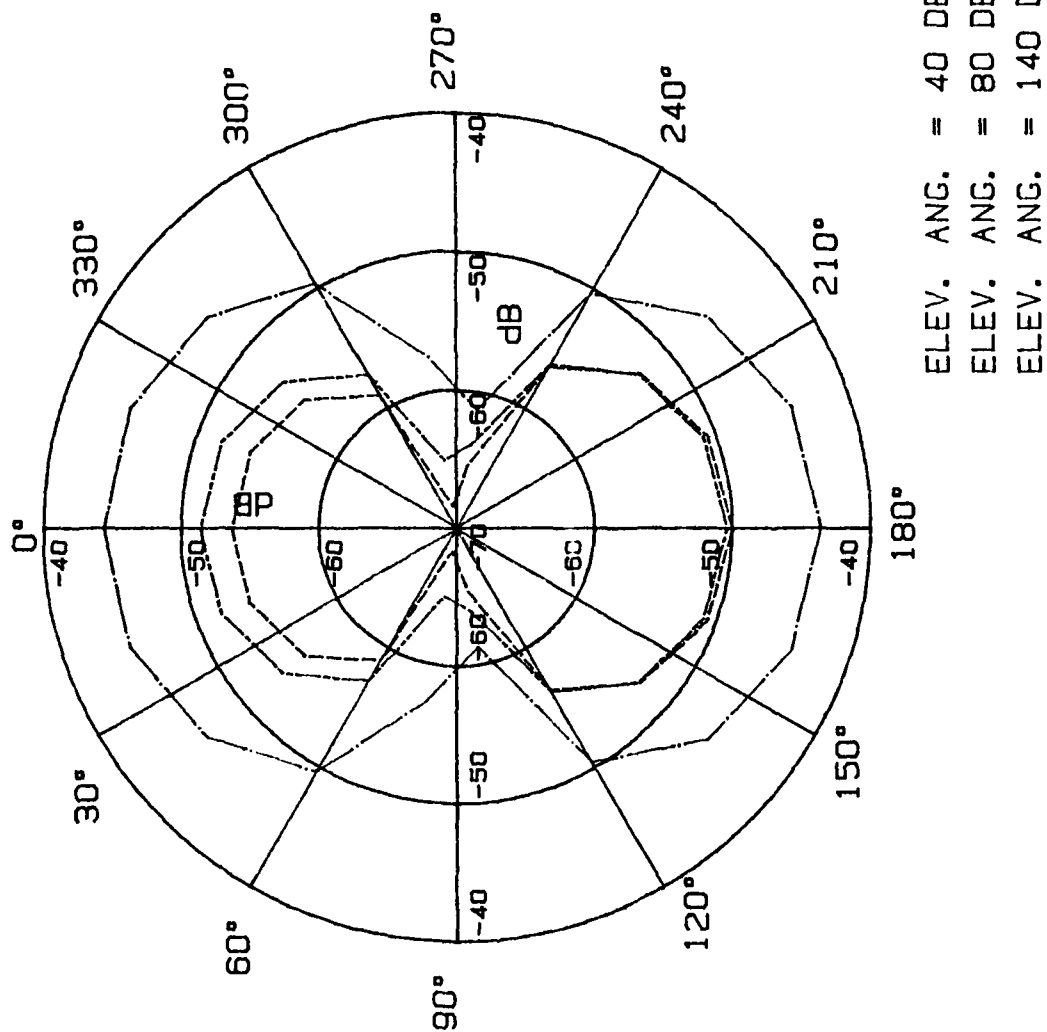


Figure IV.13 Predicted Acoustic Directivity vs ϕ for 500 Hz with Point Drive on Near-middle Frame; $\psi=40^\circ, 80^\circ, 140^\circ$.

FAR-FIELD DIRECTIVITY ON
 PLANE PASSING THRU SHELL AXIS
 DRIVE ON FRAME, CIRC. ANG.=0

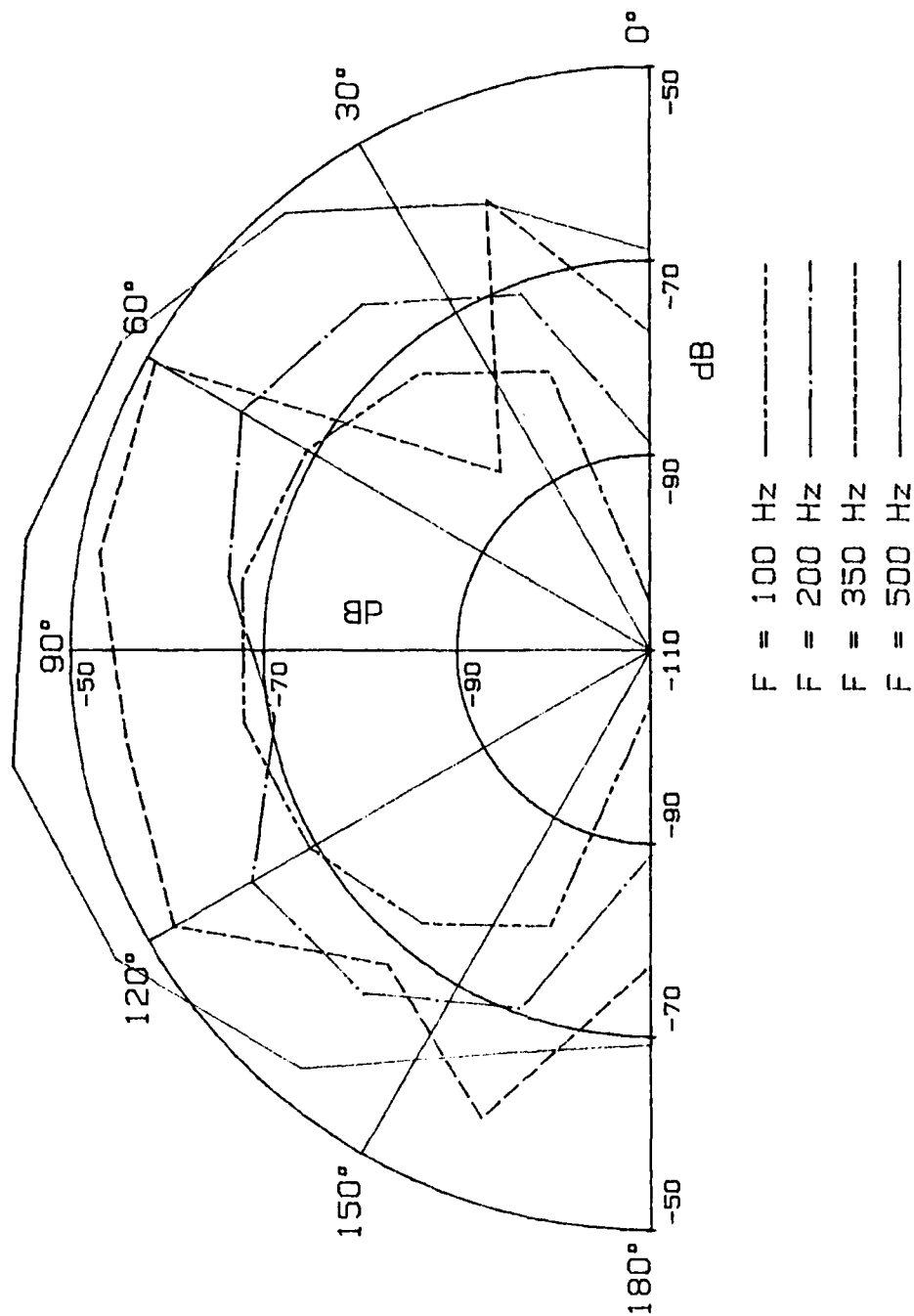


Figure IV. 14 Predicted Acoustic Directivity vs ψ for $\phi=0$; Point Drive on Near-middle Frame.

ITERATED F - SWEEPS FOR
EL. ANG. = 80 DEG, CIRC. ANG. = 0
DRIVE ON SHELL

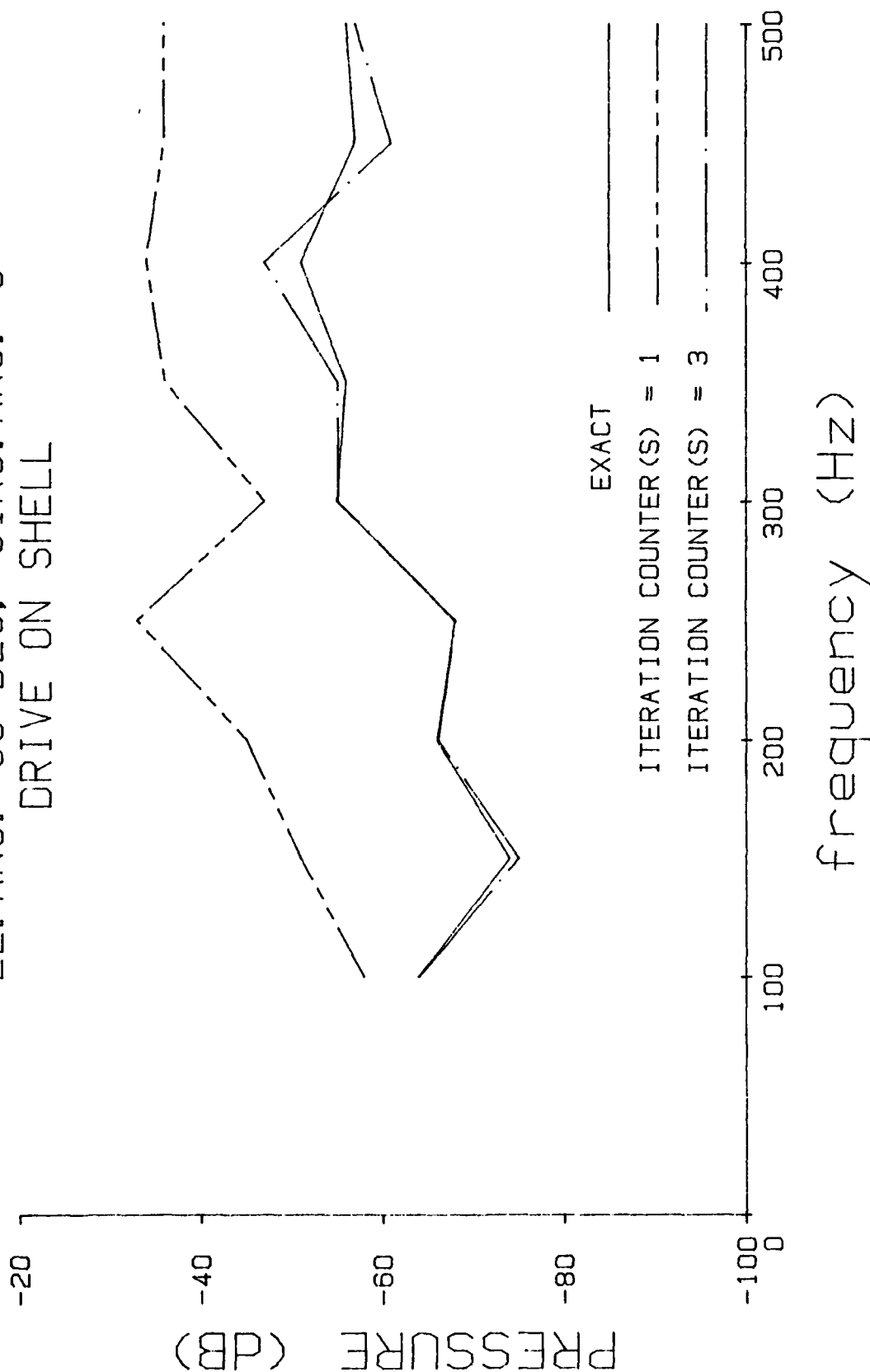


Figure IV. 15 Comparison of Exact and Approximate Spectra using Iteration; $\phi=0$, $\psi=80^\circ$; Drive on Shell.

ITERATED F - SWEEPS FOR
EL. ANG.=0, CIRC. ANG.=0
DRIVE ON SHELL

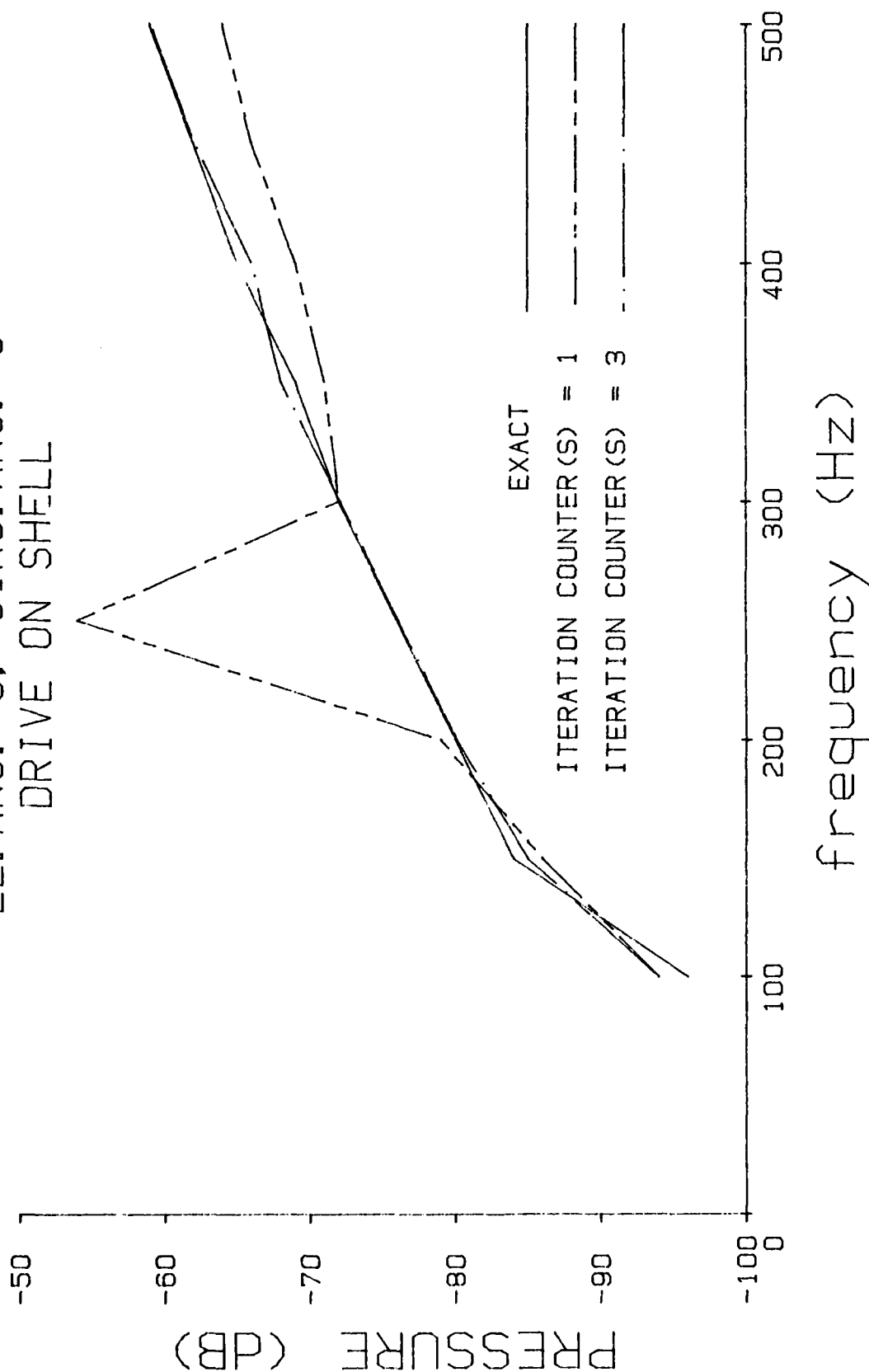


Figure IV. 16 Comparison of Exact and Approximate Spectra using Iteration; $\psi=0$ (or 180°); Drive on Shell.

ITERATED FAR FIELD FOR PLANE NORMAL TO SHELL AXIS, EL. ANG.=80 DEG DRIVE ON SHELL, F=100 Hz

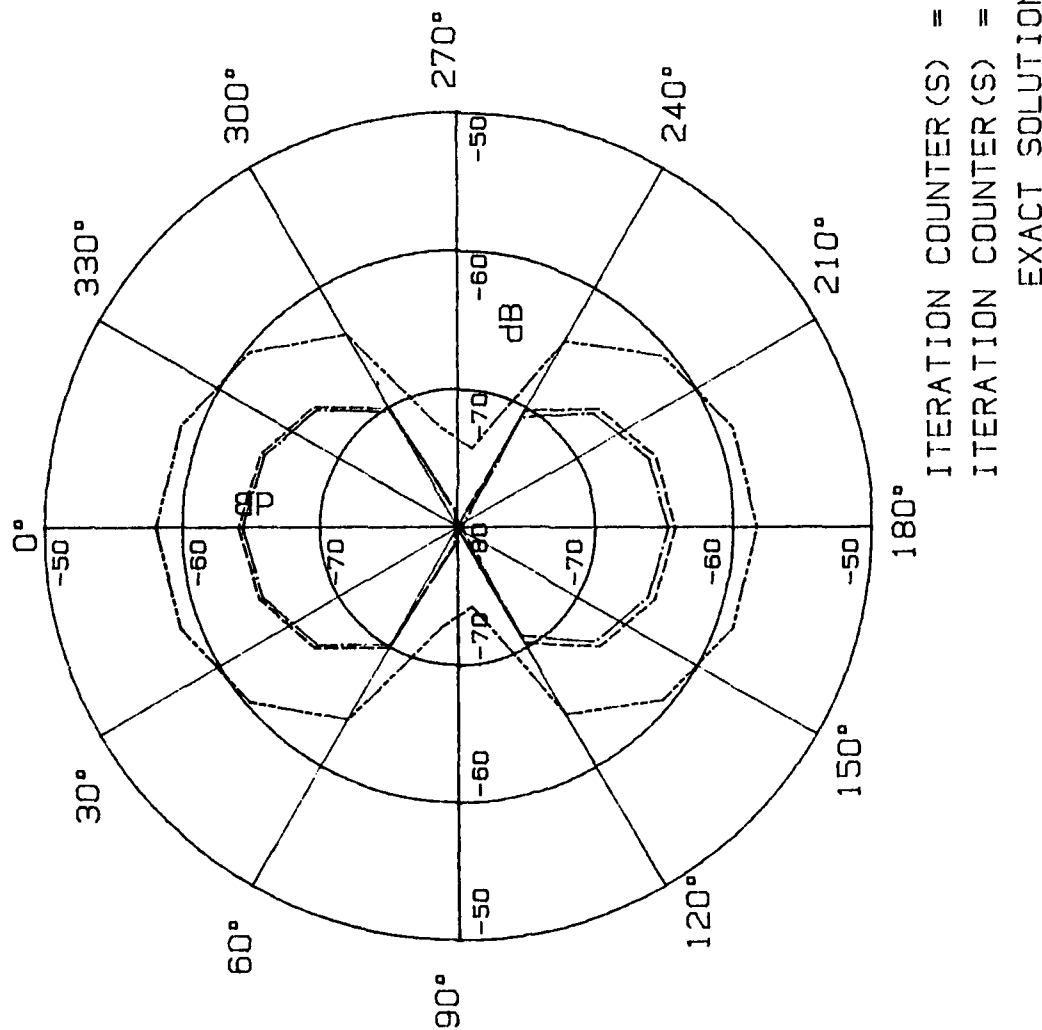


Figure IV.17 Comparison of Exact, and Approximate Directivity Patterns using Iteration; ϕ variable; $\psi=80^\circ$.

ITERATED FAR FIELD FOR PLANE
NORMAL TO SHELL AXIS, EL. ANG. = 80 DEG
DRIVE ON SHELL, F=300 Hz

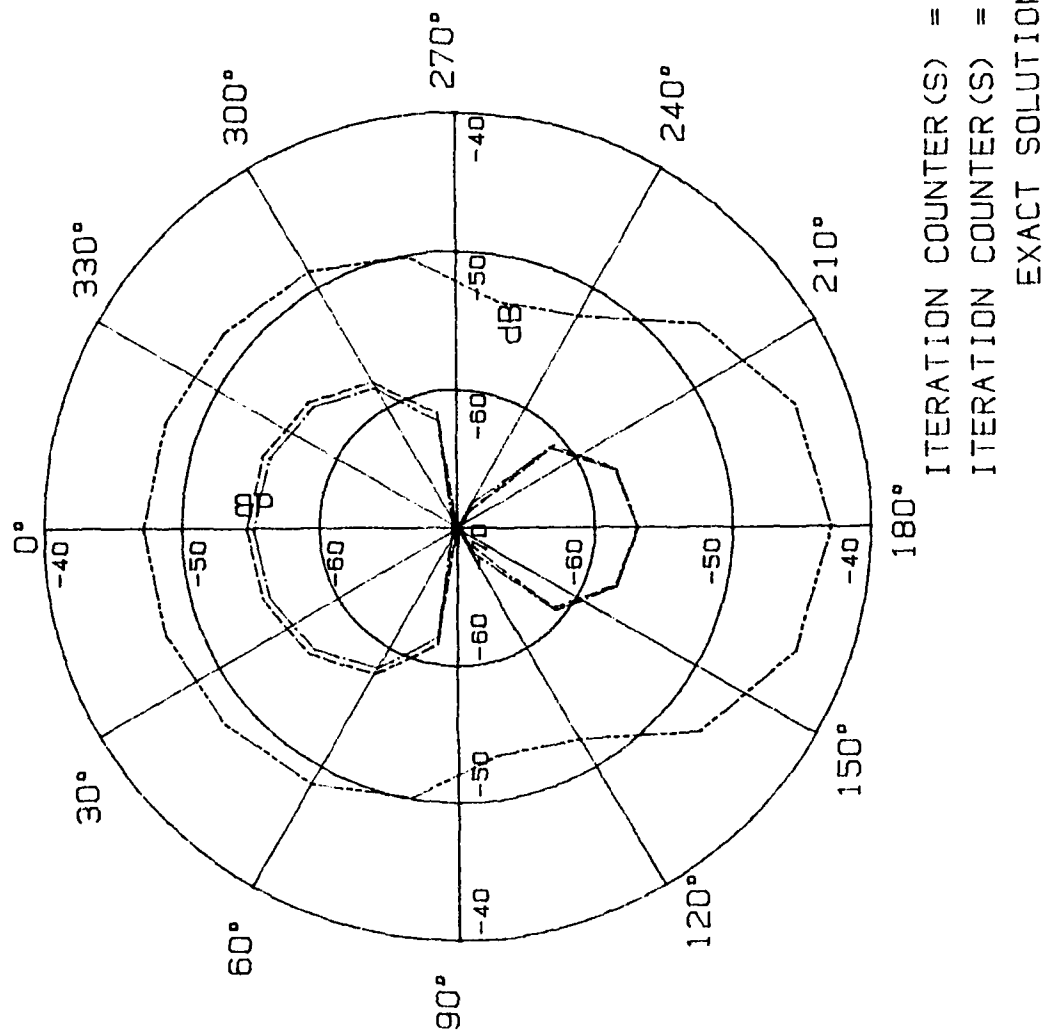


Figure IV. 18 Comparison of Exact, and Approximate Directivity Patterns using Iteration; ϕ variable; $\psi=80^\circ$;
 $f=300$ Hz; Drive on Shell.

NORMAL TO SHELL AXIS, EL. ANG. = 80 DEG
 DRIVE ON SHELL, F=400 Hz

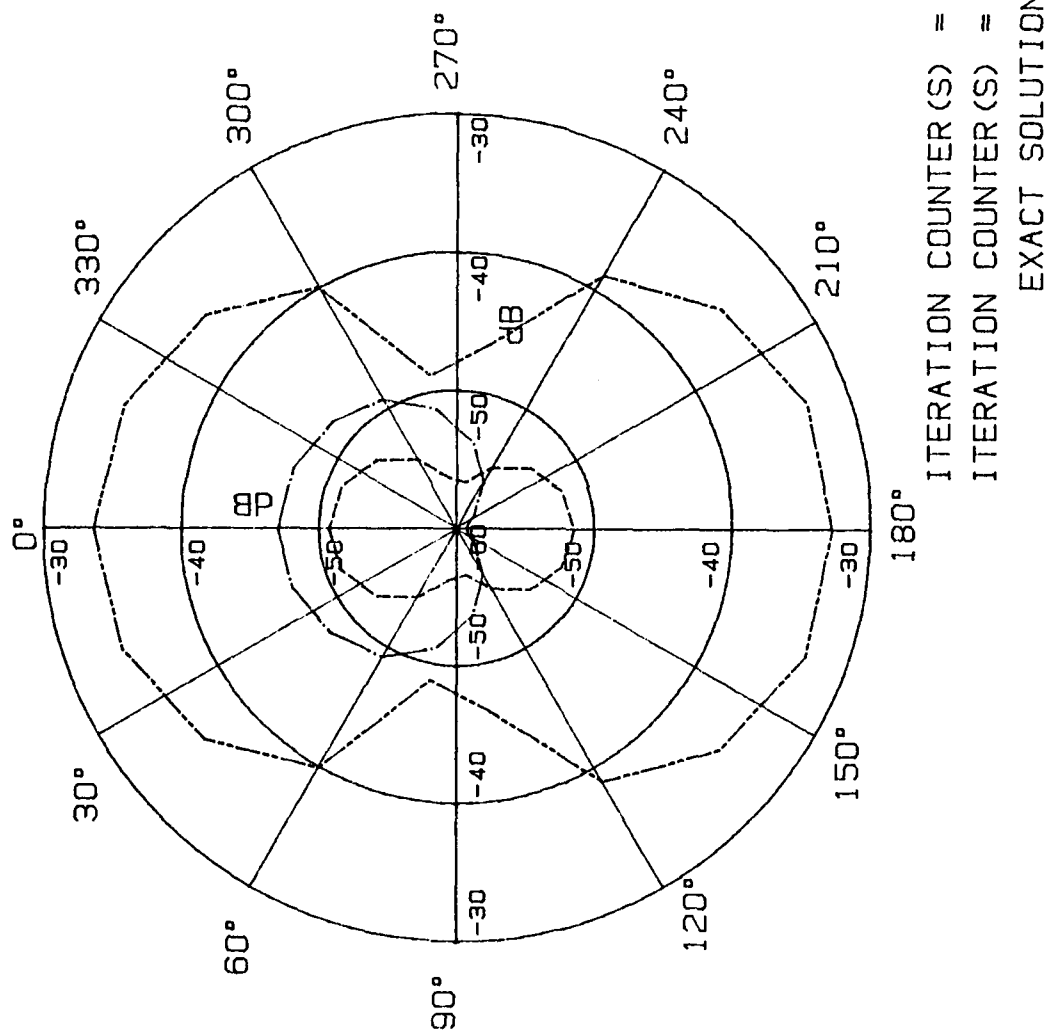


Figure IV. 19 Comparison of Exact, and Approximate Directivity Patterns using Iteration; ϕ variable, $\psi=80^\circ$; $f=400$ Hz; Drive on Shell.

NORMAL TO SHELL AXIS, EL. ANG. = 80 DEG
 DRIVE ON SHELL, F=500 Hz

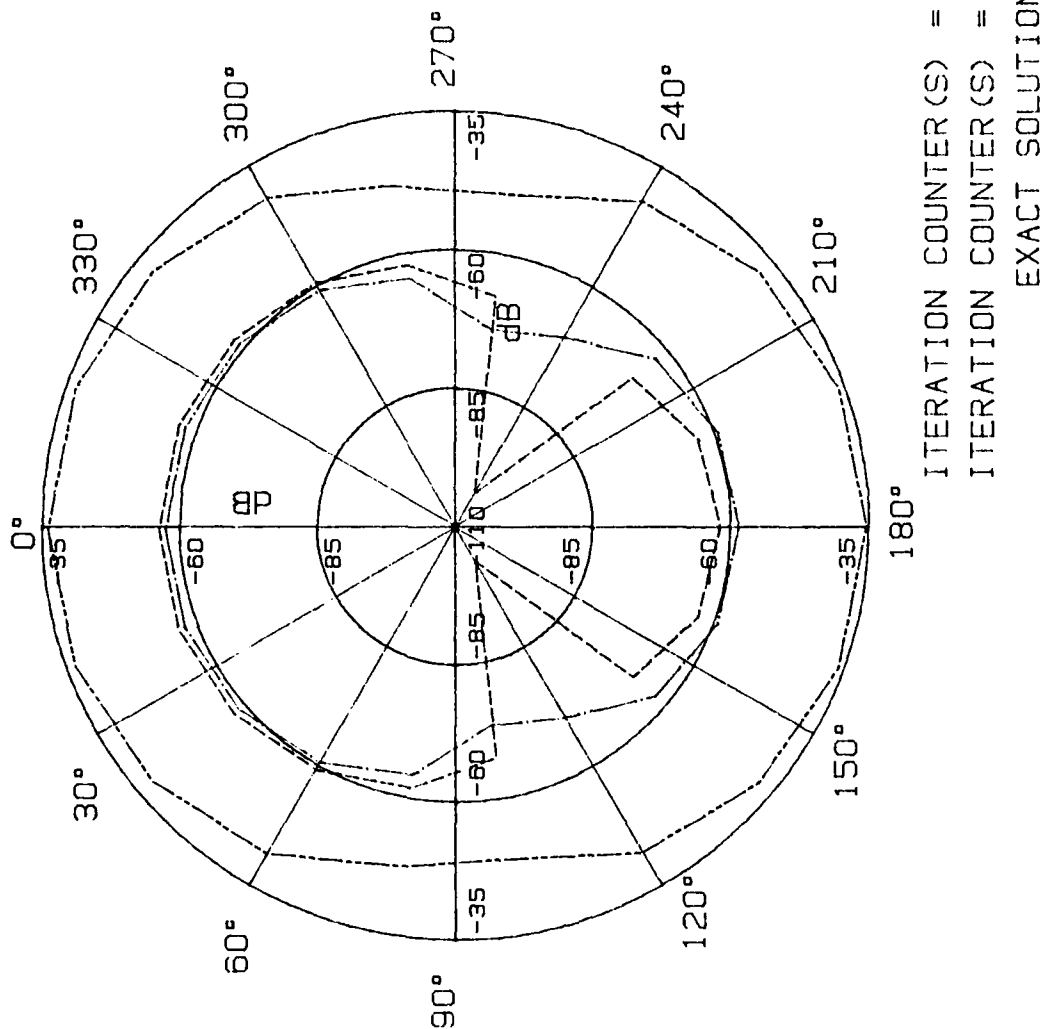


Figure IV. 20 Comparison of Exact, and Approximate Directivity Patterns using Iteration; ϕ variable, $\psi=80^\circ$; $f=500$ Hz; Drive on Shell.

DRIVE ON SHELL, $F=100$ Hz

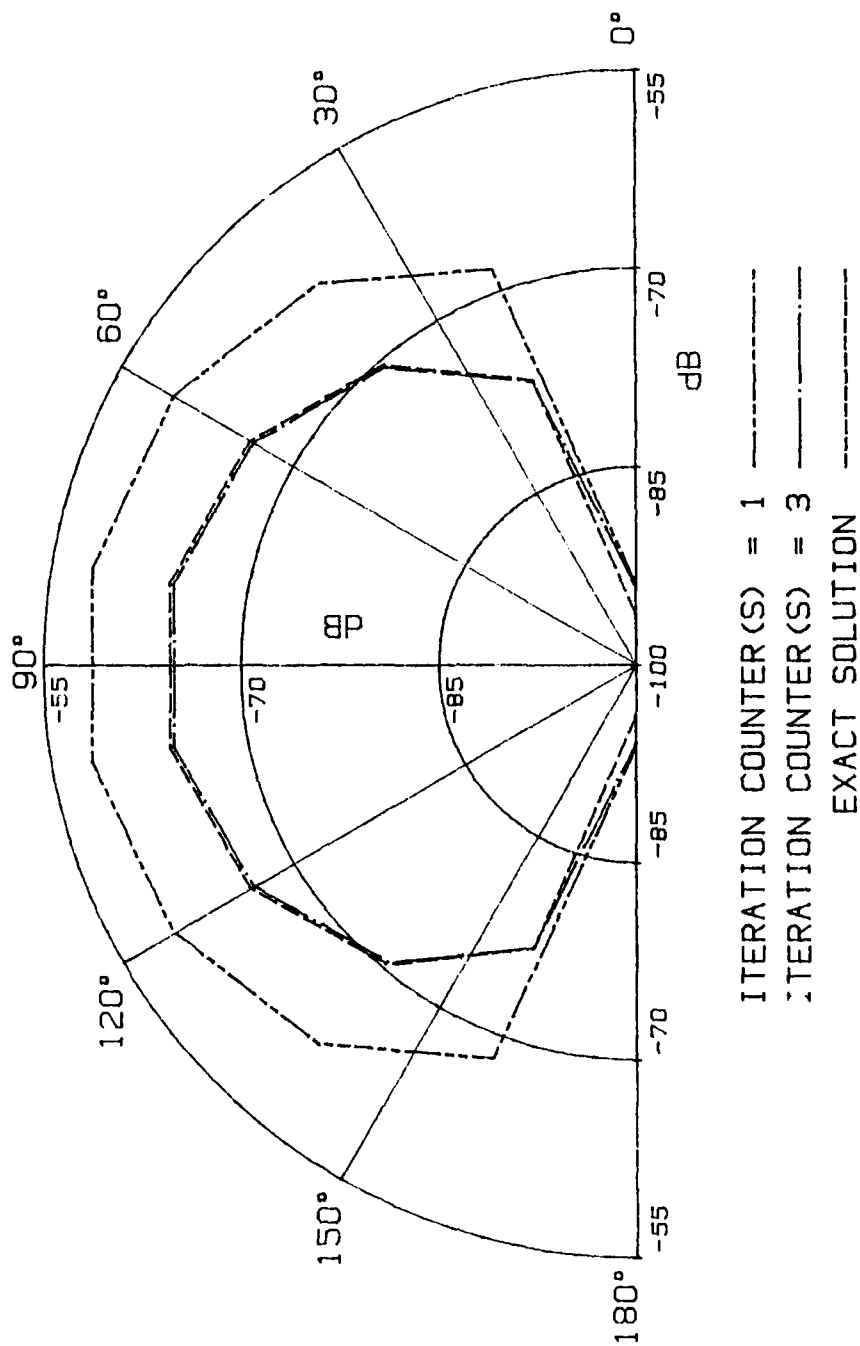


Figure IV. 21 Comparison of Exact, and Approximate Directivity Patterns using Iteration; $\phi=0$; ψ variable; $f=100$ Hz; Drive on Shell.

ITERATION SOLUTION FOR A SUBMERGED FORCE-DRIVEN FINITE
CYLINDER(U) CAMBRIDGE ACOUSTICAL ASSOCIATES INC MA
R MARTINEZ APR 85 U-1208-328 N00014-83-C-0194

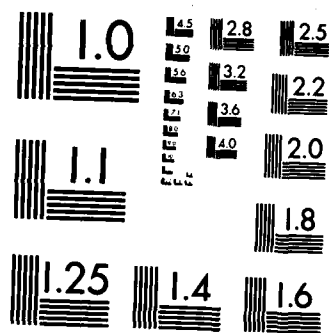
UNCLASSIFIED

F/G 20/1

NL

END

FILMED



MICROCOPY RESOLUTION TEST CHART
NATIONAL BUREAU OF STANDARDS-1963-A

ITERATED FAR FIELD FOR PLANE
PASSING THRU SHELL AXIS, CIRC. ANG. = 0
DRIVE ON SHELL, F=300 HZ

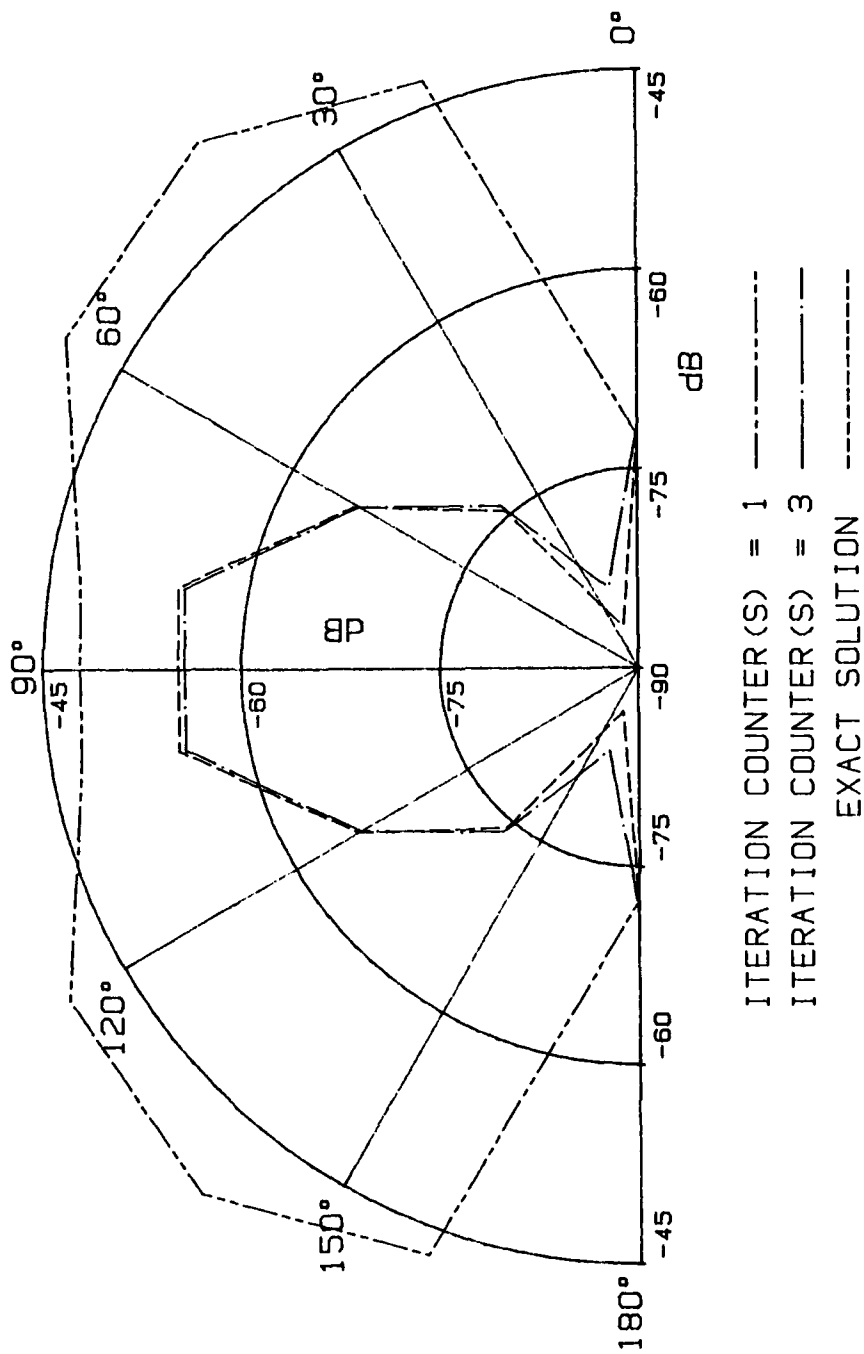


Figure IV. 22 Comparison of Exact, and Approximate Directivity Patterns using Iteration; $\phi=0$, ψ variable;
 $f=300$ Hz; Drive on Shell.

ITERATED FAR FIELD FOR PLANE
PASSING THRU SHELL AXIS, CIRC. ANG. = 0
DRIVE ON SHELL, $F=400$ Hz

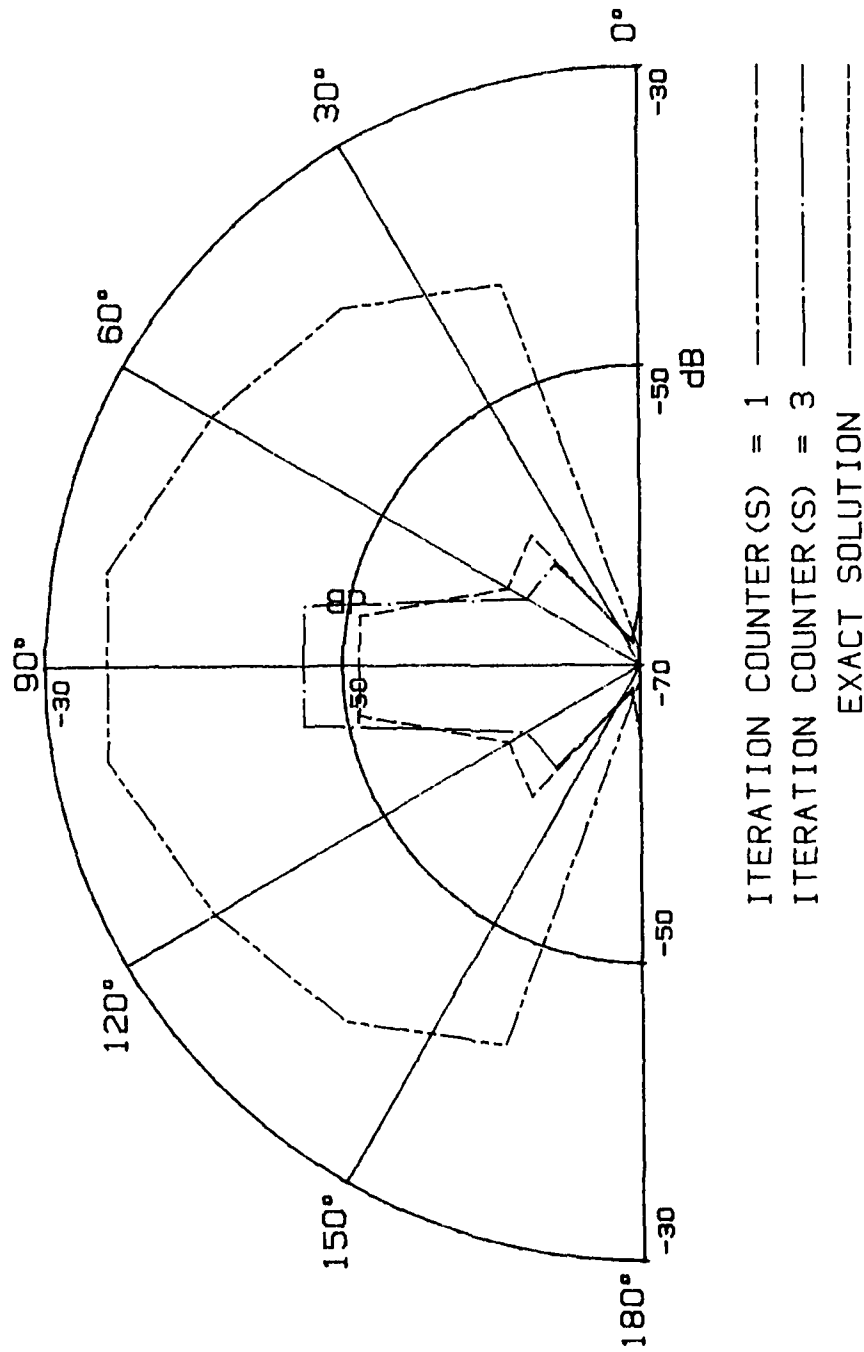


Figure IV. 23 Comparison of Exact, and Approximate Directivity Patterns using Iteration; $\phi=0$, ψ variable;
 $f=400$ Hz; Drive on Shell

ITERATED FAR FIELD FOR PLANE PASSING THRU SHELL AXIS, CIRC. ANG. = 0 DRIVE ON SHELL, F=500 HZ

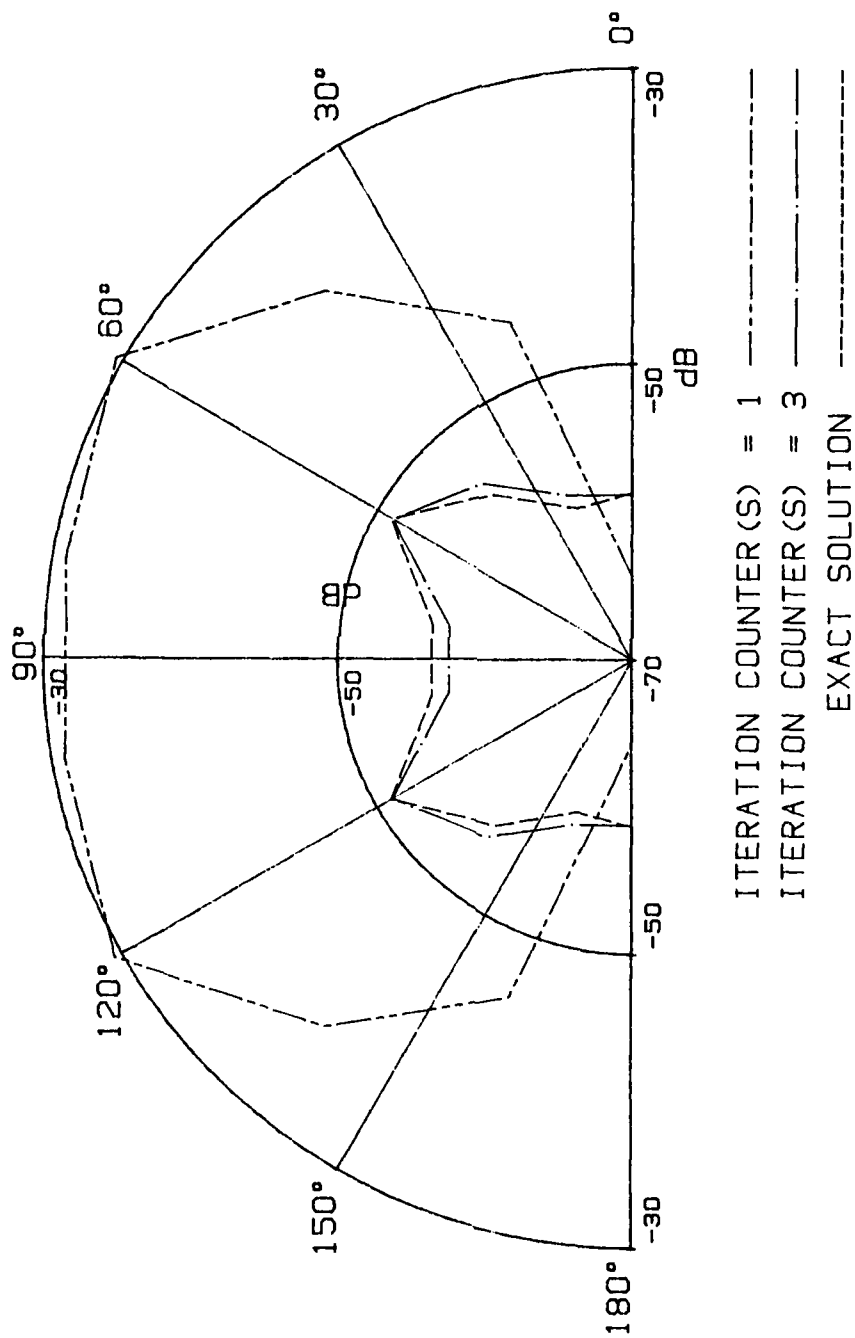


Figure IV. 24 Comparison of Exact, and Approximate Directivity Patterns using Iteration; $\phi=0, \psi$ variable;
f=500 Hz; Drive on Shell.

TABLE IV. 3
COMPUTATIONAL TIME COMPARISON BETWEEN EXACT AND ITERATED SOLUTIONS VS.
ITERATION COUNTERS K_1 , K_2

Solution #	K_1	K_2	Execution Time (secs)	% Time Savings Over Exact
1 (exact)	-	-	75.1	0
2	3	3	64.2	14.5
3	3	2	62.3	17.0
4	3	1	62.0	17.4
5	2	3	60.9	18.9
6	1	1	58.9	21.6

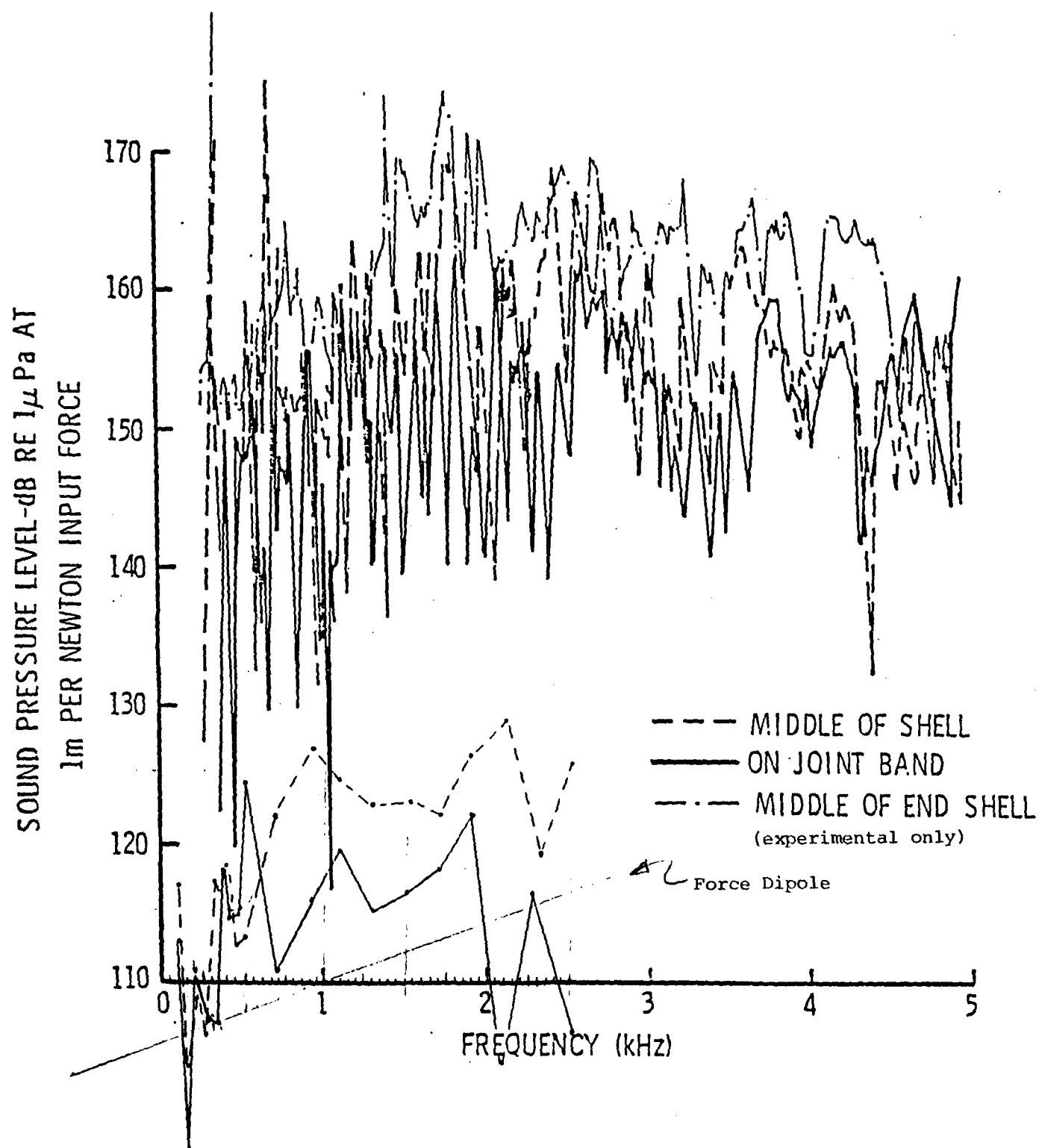


Figure IV. 25 Comparison of Predicted to Measured Spectrum (from Ref. 40) at $\phi=0$, $\psi=90^\circ$; Predictions for $f>500$ Hz use an Infinite Cylinder Model for the Fluid.

REFERENCES

- 1 R. Martinez and J. M. Garrelick, "An Exact Analysis of the Force-Excited Submerged Spherical Shell using Iterative Techniques," CAA Rept. C-911-288, Feb. 1983.
- 2 L.G. Copley, "Fundamental Results Concerning Integral Representations in Acoustic Radiation," JASA 44 (1), 1968, pp. 28-32.
- 3 H.A. Schenck, "Improved Integral Formulation for Acoustic Radiation Problems," JASA 44 (1), 1968, pp. 41-58.
- 4 K. Brod, "On the Uniqueness of Solution for all Wavenumbers in Acoustic Radiation," 76 (4), 1984, pp. 1238-1243.
- 5 I. Mathews and D. Hitchings, "Acoustic Radiation from Three-Dimensional Elastic Structures," Innovative Numerical Analysis for the Engineering Sciences, UVA Press, 1980, pp. 69-78.
- 6 G.T. Schuster and L.C. Smith, "A Comparison Among Four Direct Boundary Integral Methods," JASA, 77 (3), 1985, pp. 850-864.
- 7 H. Huang, "Helmholtz Integral Equations for Fluid-Structure Interaction," Advances in Fluid-Structure Interaction - 1984, presented at the 1984 Pressure Vessel and Piping Conference and Exhibition, San Antonio, Tx., June 17-21, 1984.
- 8 G. Chertock, "Sound Radiation from Vibrating Surfaces," JASA 36 (7), 1964, pp. 1305-1313.
- 9 R. Courant and D. Hilbert, Methods of Mathematical Physics, Vol. I, Interscience, 1966, p. 136.
- 10 B.E. Sandman, "Numerical Fluid Loading Coefficients for the Modal Velocities of a Cylindrical Shell," Comp. & Struc., 6, 1976, pp. 467-473.

- 11 B.E. Sandman, "Fluid-Loading Influence Coefficients for a Finite Cylindrical Shell," JASA 60 (6), 1976, pp. 1256-1264.
- 12 M.C. Junger and D. Feit, Sound, Structures, and Their Interaction, 1st, ed., MIT Press, 1972, p. 207.
- 13 V.A. Kozyrev and E.L. Shenderov, "Radiation Impedance of a Cylinder of Finite Height, "Sov. Phys. Acous., 26 (3), 1980, pp. 230-236.
- 14 V. A. Kozyrev and E.L. Shenderov, "Radiation Impedance of a Cylinder with Acoustically Compliant Ends," Sov. Phys. Acous., 27 (3), 1981, pp. 247-248.
- 15 J.S. Patel, "Radiation and Scattering from an Arbitrary Elastic Structure using Consistent Fluid Structure Formulation," Computers & Struct., 9, 1978, pp. 287-291.
- 16 T.L. Geers, "Transient Response Analysis of Submerged Structures," Finite-Element Analysis of Transient Nonlinear Structural Behavior, edited by T. Belytschko, et.al., ASME, N.Y., 1975, pp. 59-84.
- 17 T.L. Geers, "Doubly Asymptotic Approximations for Transient Motion of Submerged Structures," JASA, 64(5), 1978, pp. 1500-1508.
- 18 T.L. Geers and C.A. Felippa, "Doubly Asymptotic Approximations for Vibration Analysis of Submerged Structures," Lockheed Palo Alto Research Laboratory Rept. prepared for DTNSRDC/Annapolis, Sept. 1981.
- 19 H. Huang and Y.F. Wang, "Asymptotic Fluid-Structure Interaction Theories for Acoustic Radiation Prediction," Advances in Fluid-Structure Interactions - 1984, see. ref. 7 for details.
- 20 D. Ranlet, F.L. Dimmagio, H.H. Bleich and M.L. Baron, "Elastic Response of Submerged Shells with Internally Attached Structures to Shock Loading," Comp. & Struct., 7, 1977, pp. 355-364.

- 21 L.H. Chen and D. G. Schweikert, "Sound Radiation from an Arbitrary Body," JASA, 35 (1), 1963, pp. 1626-1632.
- 22 M.L. Baron, L.A. Matthews, and H. H. Bleich, "Forced Vibrations of an Elastic Circular Cylindrical Body of Finite Length Submerged in an Acoustic Medium," Weidlinger Tech. Rept. 1, prepared for ONR, June 1962.
- 23 J. M. McCormick and M.L. Baron, "Sound Radiation from Submerged Cylindrical Shells of Finite Length," Weidlinger Tech. Rept. 3, prepared for ONR, June 1964.
- 24 J. M. McCormick and M. L. Baron, "Sound Radiation from Submerged Stiffened Cylindrical Shells of Finite Length with Flexible End Caps," Weidlinger Tech. Rept. 9, prepared for ONR, Aug. 1970.
- 25 D. G. Crighton, "Resonant Oscillations of Fluid-Loaded Struts," J. of Sound & Vib., 87 (3), 1983, pp. 429-437.
- 26 C.B. Burroughs, "Acoustic Radiation from Fluid-Loaded Infinite Circular Cylinders with Periodic Ring Supports," JASA, 75, (3), 1984, pp. 715-722.
- 27 J.E. Cole, "Parametric Study and Design Implications of the Low Frequency Response and Radiated Noise of a Submarine Hull," CAA Rept. C-938-274.13E, prepared for Naval Sea Systems Command, Aug. 1983.
- 28 A. Harari, "Wave Propagation in Cylindrical Shells with Finite Regions of Structural Discontinuity," JASA, 62 (5), 1977, pp. 1196-1205.
- 29 D.M. Young, Iterative Solution of Large Linear Systems, Academic Press, N.Y., 1971.
- 30 M.K. Au-Yang, "Natural Frequencies of Cylindrical Shells and Panels in Vacuum and in a Fluid," JASA, 57 (3), 1978, pp. 341-355.

- 31 Y.W. Chang and C.Y. Wang, "An Eulerian Method for Large Displacement Fluid Structure Interaction in Reactor Containment," Computational Methods for Fluid-Structure Interaction Problems, AMD Vol. 26, Winter Annual Meeting of the ASME, Atlanta, Ga., Nov. 27-Dec. 2, 1977, pp. 1-14.
- 32 T. Belytschko, "Fluid-Structure Interaction," Comp. & Struc., 12, 1980, pp. 459-469.
- 33 W. Whitlow and W. L. Harris, "Lifting Airfoils in Transonic Flow in Parametric Differentiation," AIAA Paper 80-1394. Presented at the 13th AIAA Fluid and Plasma Conf., Snowmass Col., July 14-16, 1980.
- 34 O.D. Kellogg, Foundations of Potential Theory, Dover, N.Y., 1953, p. 299.
- 35 A. W. Leissa, Vibration of Shells, NASA SP-288, 1973; for Donnell-Mushtari theory see p. 32.
- 36 M.E. Goldstein, Aeroacoustics, McGraw-Hill, N.Y., 1976, p. 119.
- 37 A.A. Cannarozzi and E. D'Anna, "A Routine for Solving Sparse Linear Systems in Structural Analysis," Comp. & Struc., 6, 1976, pp. 99-105.
- 38 H. Peterson and E. P. Popov, "Substructuring and Equation System Solutions in Finite-Element Analysis," Comp. & Struc., 7, 1977, pp. 197-206.
- 39 A. Maher, P.G. Kessel, and R.D. Cook, "A Partitioned Finite-Element Method for Dynamical Systems," Comp. & Struc., 18, pp. 81-91.
- 40 C. B. Burroughs, S.I. Hayek, D.A. Bostain, and J.E. Hallander, "Acoustic Radiation from Single and Double Ribbed Circular Cylindrical Shells," Penn. State ARL TM 84-76, March 1984; also, "Resonant Frequencies and Mode Shapes for Single and Double Cylindrical Shells," Penn. State ARL TM 83-169, Sept. 1983.
- 41 H.B. Ali and D. Feit, "Acoustic Measurements and Prediction for a Submarine Model - A Heuristic Appraisal," DTNSRDC Rept. 78/042, May 1978.
- 42 M.C. Junger, "Force Dipole Noise Radiation by Submarine Hulls," CAA Rept. C-890-274, 13A prepared for Naval Sea Systems Command, July 1983.

END

FILMED

7-85

DTIC